Model-Based Optimization of Ultra High Performance Concrete Highway Bridge Girders

by

Hesson Park

B.S., Seoul National University (2001)

Submitted to the Department of Civil and Environmental Engineering
in partial fulfillment of the requirements for the degree of

Master of Science in Civil and Environmental Engineering

at the

MASSACHUSETTS INSTITUTE OF TECHNOLOGY

June 2003

© 2003 Massachusetts Institute of Technology. All rights reserved.

BARKER

MASSACHUSETTS INSTITUTE OF TECHNOLOGY
JUN 0 2 2003
LIBRARIES

Signature of Author .....
Department of Civil and Environmental Engineering
April 7, 2003

Certified by ....
Franz-Josef Ulm
Associate Professor of Civil and Environmental Engineering
Thesis Supervisor

Accepted by..... .....
Oral Buyukozturk
Chairman, Department Committee on Graduate Students

Model-Based Optimization of Ultra-High Performance Concrete Highway Bridge Girders

by

Hesson Park

Submitted to the Department of Civil and Environmental Engineering
on April 7, 2003, in partial fulfillment of the
requirements for the degree of
Master of Science in Civil and Environmental Engineering

Abstract

Ultra High Performance Concrete (UHPC) represents a breakthrough for civil engineering materials. Compared to conventional concrete solutions, UHPC possesses such dramatic mechanical improvements that new design philosophies, safe guidelines, and design tools for UHPC structures are required to gain true acceptance in the global civil engineering design and construction community. The research presented in this report aims at contributing to this goal through the development of a comprehensive model-based optimization methodology and its application toward the design of UHPC highway bridge girders.

At the core of the proposed model-based design strategy is a macroscopic two-phase UHPC material model, in which the brittle-plastic composite matrix and the elasto-plastic composite fiber reinforcement are modeled as two distinct and interacting phases, using a minimal number of model input parameters that are all accessible by a single notched tensile test.

The UHPC model is combined with maximum crack width criteria, which aptly define the Service Limit State (SLS) and the Ultimate Strength Limit State (ULS) of UHPC structures, to yield a three step design strategy for UHPC bridge girders: 1) 1-D section design models suffice for initial estimates of section dimensions and design parameters (prestressing level, etc.). 2) A refined 2-D finite element model is employed for assessment of the global flexural and shear resistance of UHPC girders that is quantified in terms of admissible matrix plastic strains (normalized crack widths) at SLS and ULS. Finally, complete 3-D finite element simulations allow the study of localized 3-D stress and cracking states, which occurs as a result of punching shear in unreinforced UHPC slab systems or transfer of prestressing.

Hence, a comprehensive method for the model-based design of UHPC structures is developed. Design solutions are proposed for prestressed double-tee sections for small and medium span highway bridge girders ($21.3 - 36.6\,\mathrm{m}$ ($70 - 120\,\mathrm{ft}$)), which possess many advantages over conventional precast concrete solutions (reduction in height and weight, elimination of shear reinforcement, etc.), and which will ultimately translate into easier and faster construction processes, longer life spans with higher durability and less maintenance.

Thesis Supervisor: Franz-Josef Ulm
Title: Associate Professor of Civil and Environmental Engineering

Contents

1 INTRODUCTION **13**

1.1 Industrial Context 13

1.2 Background and Research Significance 15

1.3 Research Objectives and Approach 16

1.4 Outline of the Report 18

I UHPC-MODEL AND MODEL VALIDATION **20**

2 UHPC MATERIAL MODEL **21**

2.1 1-D UHPC Model 22

2.1.1 1-D Think Model of UHPC Material Behavior 23

2.1.2 Constitutive Relations 24

2.1.3 1-D Thermodynamics 27

2.1.4 Energy Transformation during Brittle-Plastic Fracture 29

2.2 3-D UHPC Model 30

2.2.1 3-D Isotropic Elasticity Properties 31

2.2.2 3-D Strength Domain 33

2.3 Summary of the Input Parameters 38

3 UHPC MODEL VALIDATION **41**

3.1 The FHWA UHPC Girder Tests 42

3.1.1 Validation Criteria 42

3.1.2 Modeling of Prestressing: Upper and Lower Bound 43

3.1.3 Section Modeling and Load Application 47
3.2 Validation Set #1: FHWA Flexure Test 47
3.2.1 Global Results: Load-Deflections Curves 47
3.2.2 Local Results: Strain Gauge Measurements 48
3.2.3 Local Results: Cracking Patterns 50
3.3 Validation Set #2: FHWA Shear Test 53
3.3.1 Global Results: Load-Deflections Curves 53
3.3.2 Local Results: Strain Gauge Measurements 55
3.3.3 Local Results: Cracking Patterns 57
3.3.4 Discussion of UHPC Model Validation 57
3.4 Design Load Prediction 59
3.5 Summary of Model and Model Validation 62

II MODEL-BASED OPTIMIZATION 64

4 UHPC SECTION DESIGN FORMULA, DESIGN CRITERIA AND DESIGN STRATEGY 65

4.1 1-D Section Design Formula 65
4.2 Model-Based Design Strategy 69
4.2.1 LRFD Design versus UHPC Design Criteria 70
4.2.2 Optimization Procedure 72
4.3 1-D Optimization: Primary Section Parameters 74
4.3.1 Section Parameters 75
4.3.2 Prestressing Parameters 75
4.3.3 UHPC Composite Material Parameters 76
4.3.4 Design Moment 76
4.3.5 Minimum Height Prediction 81
4.4 Summary of UHPC Design Strategy 82

5 MODEL-BASED DESIGN 84

5.1 Design Parameters 84

5.1.1 Common Section Types 85
5.1.2 Choice of Section Profile and Section Parameters 86
5.1.3 Load and Modeling of Loading 88
5.2 2-D Optimization: Validation of Design Formula 89
5.2.1 2-D Section Modeling 89
5.2.2 Global Optimization Results: ULS Flexural Resistance 91
5.2.3 Design Control #1: Service Limit State 97
5.2.4 Design Control #2: Shear Resistance 98
5.2.5 Design Remark 98
5.3 3-D Optimization: Minimum UHPC Slab Thickness 99
5.3.1 3-D Section Modeling 102
5.3.2 3-D ULS Design 103
5.3.3 3-D SLS Design and Appraisal of the 'No Cracking' Criterion 105
5.3.4 Design Control #1: Slab Joint Position 108
5.3.5 Design Control #2: Transfer of Prestressing 116
5.4 Case Study of Two-Span Continuous UHPC Girders 117
5.4.1 2-D Finite Element Model: Achieving Continuity After Prestressing . . . 118
5.4.2 Model-Based ULS Analysis 119
5.4.3 Comment on UHPC Continuous Beams 122
5.5 Summary of Optimized Design Solutions for UHPC Double-Tee Girder Sections . 126

6 CONCLUSIONS AND OUTLOOK 129
6.1 Summary of Scientific Findings 129
6.1.1 Model-Based Optimization Framework: UHPC Model and Crack Opening Criteria 130
6.1.2 A Comprehensive Model-Based Design Strategy: From 1-D Design Formulas to 3-D Finite Element Simulations 131
6.2 Industrial Benefits 132
6.3 Current Limitations and Suggestions for Future Research 133

A Conversion Factors 139

List of Tables

2.1 Input parameters of the 3-D UHPC model and typical values for DUCTAL^{TM}, derived from a notched tensile plate test. 39

3.1 Values of UHPC model parameters used in the FHWA flexure and shear finite element simulations. Bold characters denote change in material parameters. . . . 46

4.1 Values of 'effective' UHPC model parameters. Bold characters denote changes made in material parameters. 77

4.2 Summary of loads: nominal loads, partial load factors, and design loads. (*) For 2-D simulations, the wheel load p_2 is smeared out over the traffic lane of width $B = 3.6576$ m (12 ft), i.e. $p_2(2\text{D}) = p_2(3\text{D})b_w/B$, where $b_w = 0.51$ m (20 in) is the transversal tire width. 80

4.3 Summary of maximum moment for various spans. (*) The self-weight is calculated assuming cross sectional area of $A = 0.645\text{m}^2$ (1000in^2). 81

4.4 Input - output parameters of the optimization process. 83

5.1 Minimum web heights for single span UHPC girders. 96

5.2 List of meshes for 3D analysis of the slabs. The "L" and "H" in the mesh name stand for the low (4.45 MN (1,000 kips)) and the high level (6.68 MN (1,500 kips)) of prestressing. 103

5.3 Design parameters employed in the study of applicability of double-tee girders for coninuous beams. 118

5.4 Choice of section for double-tee girders prestressed with 4.45 MN (1,000 kips) per lane. (*)The total prestress force, cross-sectional area and estimated weight/lane are calculated for a single traffic lane composed of 1.5 double-tee girder sections. 127

5.5 Choice of section for double-tee girders prestressed with 6.68 MN (1,500 kips) per lane. (*)The total prestress force, cross-sectional area and estimated weight/lane are calculated for a single traffic lane composed of 1.5 double-tee girder sections. 128

A.1 Conversion factors between SI and IU units. 139

List of Figures

1-1 Annual vehicle miles of highway travel (years 1992 - 2000) [17]. 14

1-2 Comparison of the flexural strengths of UHPC (DUCTAL^{TM}) and conventional concrete (HPC) [4]. 15

1-3 Economic benefits from using UHPC (DUCTAL^{TM}); Case study of a 19m wide, 2 km long four-lane bridge design for automobile travel [29]. 16

2-1 Typical stress-crack opening response of a UHPC material; results from notched tensile test [7]. 23

2-2 1D Think Model of a two-phase matrix-fiber composite material [14]. 24

2-3 Stress-strain response of the two-phase composite model [14]. 25

2-4 Two sources of energy dissipation upon cracking of brittle-plastic composite material [14]: (a) brittle fracture, (b) frictional dissipation, (c) total dissipation. . . 29

2-5 Biaxial composite matrix strength domain [12]. 36

2-6 Composite matrix strength domain in the $I_1 - |\underline{\underline{s}}|$ the halfplane (left), and stress-strain response (right) [12]. 37

2-7 (a) Experimental notched tensile test data of DUCTAL^{TM} by Lafarge; (b) Stress-strain response of the 3-D UHPC model using input data of Table 2.1. 40

3-1 Cross section of the AASHTO Type II girder: (a) Actual beam; (b) Idealized 2-D model in finite element simulation. 43

3-2 Loading configuration and strain gauge locations for the FHWA flexure test. . . . 48

3-3 Model-based simulation results of FHWA flexure test: (a) Fine mesh with boundary conditions; (b) Deformed shape; (c) Composite matrix plastic strains. 49

3-4 FHWA flexure test: Global force-midspan deflection curve. 50
3-5 FHWA flexure test: Local strain gauge measurements. 51
3-6 Evolution of longitudinal composite matrix plastic strains $\varepsilon^{p}_{M,xx}$ along the height of the FHWA flexure girder at the midpoint as predicted by the upper bound fine mesh simulation. 52
3-7 Evolution of longitudinal stresses $\Sigma_{xx} = \sigma_{M,xx} + \sigma_{F,xx}$ along the height of the FHWA flexure girder at the midpoint as predicted by the upper bound fine mesh simulation. 52
3-8 Loading configuration and strain gauge locations for the FHWA shear test. . . . 53
3-9 Model-based simulation results of FHWA shear test: (a) Fine mesh with boundary conditions; (b) Deformed shape; (c) Composite matrix plastic strains. 54
3-10 FHWA shear test: Global force-midspan deflection curve. 56
3-11 FHWA shear test: Local strain gauge measurements. 56
3-12 Model-based simulation results of composite matrix cracking: (a) Crack initiation at the flange-web interface; (b) Fully developed shear cracks in the web; (c) Experimental crack patterns at failure of the shear beam. 58
3-13 Normalized load F/F_u versus normalized plastic strain for: (a) FHWA flexure test ($F_u = 800\,\text{kN}$ (180 kips)); (b) FHWA shear test ($F_u = 3,400\,\text{kN}$ (765 kips)). 61

4-1 The two-point engineering section design model: (a) Realistic stress Distribution of a UHPC Section in bending; (b) Simplified design model. 66
4-2 The stress-strain relation and the limiting strains of French UHPC guidelines [38]. $\varepsilon_{u,0.3}$ is the strain corresponding to the crack opening of $[[w]]^{un}_{\text{lim}} = 0.3\,\text{mm}$, i.e. $\varepsilon^{p,un}_{\text{lim}}$ in our report, and ε_{lim} is the same parameter as $\varepsilon^{p,re}_{\text{lim}}$ in our report. 73
4-3 Design truck load from AASHTO Standard Specifications [5]. 78
4-4 Load configuration for maximum moment. 80
4-5 H' versus span L using the design formula, for two prestressing forces. 82

5-1 AASHTO standard girder types. [3] 85

5-2 Examples of UHPC girder design for (a) Short spans ($L < 21\,\mathrm{m}$ (70 ft)); (b) Medium spans ($21 - 36\,\mathrm{m}$ ($70 - 120\,\mathrm{ft}$)); and (c) long spans ($L > 36\,\mathrm{m}$ (120 ft)); from [35]. 86
5-3 Double-tee or π-section girder: (a) Section; (b) 3-D view of a traffic lane, where $B_g = 2B/3$. 87
5-4 Load chronology scheme applied in model-based simulations for (a) Service limit state analysis; (b) Ultimate strength limit state analysis. 90
5-5 Cross section of double-tee girder: (a) Actual beam; (b) Idealized 2-D modeling in finite element simulation. 91
5-6 Loading scheme for (a) flexure and (b) shear. 92
5-7 Model-based simulation of flexural loading of the girder with $L = 21.3\,\mathrm{m}$ (70 ft): (a) Mesh with boundary conditions and loads; (b) Deformed shape; (c) Composite matrix plastic strains. 93
5-8 Model-based simulation results: Normalized ULS live load versus normalized plastic strain for: (a) Web height H_w from design formula (starting point of model-based optimization); (b) Optimized web height. 95
5-9 Results of 2-D optimization procedure: Minimum girder height $H = H_w + T_s + T_f$ versus span L. ($T_s = 0.10\,\mathrm{m}\,(4\,\mathrm{in})$, $T_f = 0.15\,\mathrm{m}\,(6\,\mathrm{in})$ were fixed values in the optimization procedure). For purpose of comparison, the figure also displays the results of the 1-D optimization procedure for two prestress force levels of $P_{1,000} = 4.45\,\mathrm{MN}$ ($1,000\,\mathrm{kips}$) and $P_{1,500} = 6.68\,\mathrm{MN}$ ($1,500\,\mathrm{kips}$) per traffic lane. . 96
5-10 Model-based simulation results for optimized section heights: normalized SLS live load versus normalized plastic strain. 97
5-11 Design parameters for slab thickness optimization: (a-b) Design truck location; (c-d) Slab joint location. 100
5-12 Employed mesh for the the slab thickness optimization: Section and 3-D view of 3D-30H-5S girder (in Table 5.2) mesh, with the location of HS-20 truck load and the boundary conditions. 102

5-13 Model-based simulation results for 3D-30L girders: Normalized ULS live load versus normalized plastic strain for three slab thicknesses $T_s = 0.05\,\mathrm{m}$ (2 in), 0.075 m (3 in), 0.10 m (4 in). The admissible ULS plastic strains according to (5.8) decrease with increasing T_s: $D_{\mathrm{lim}} = 1/110...1/170...1/220$. 104
5-14 Model-based simulation results for 3D-30L girders: Normalized SLS live load versus cumulative crack opening for three slab thickness $T_s = 0.05\,\mathrm{m}$ (2 in), 0.075 m (3 in), 0.10 m (4 in). 105
5-15 Slab thickness versus normalized SLS live load at which the first cracking occurs in the simulations. 106
5-16 Normalized crack width at the SLS design load (normalized by the ULS limit crack opening of $[[w]]^{un}_{\mathrm{lim}} = 0.3\,\mathrm{mm}\left(\frac{1}{85}\,\mathrm{in}\right)$) versus slab thickness. 107
5-17 Plastic strains of 3D-30L-5S girder slab at SLS. Top: the plastic strain distribution. Bottom: the direction of principal plastic strains. The mesh is tilted to show the cracking at the bottom of the slab. A dashed and a solid arrow is given as references for the longitudinal and transversal direction of the girder, respectively. 109
5-18 Plastic strains of 3D-30L-5S girder slab at ULS. Top: the plastic strain distribution. Bottom: the direction of principal plastic strains. The mesh is tilted to show the cracking at the bottom of the slab. A dashed and a solid arrow is given as references for the longitudinal and transversal direction of the girder, respectively. 110
5-19 2-D Model-based simulation results for girders of span $L = 30.5\,\mathrm{m}$ (100 ft): Normalized ULS live load versus normalized plastic strain for two slab thickness $T_s = 0.10\,\mathrm{m}$ (4 in) and 0.15 m (6 in). Effect of the increase in slab thickness on the overall structural performance. 111
5-20 3-D Model-based investigation of the effect of the slab joint position: (a-b) Section models with load and boundary conditions; (c) 3D–view of mesh with joint in slab mid span, showing the location of HS-20 truck loads; (d-e) Plastic strain distribution under the truck wheel load. 112

5-21 Normalized service live load versus normalized crack opening for: (a) $T_s = 0.05\,\mathrm{m}$ (2 in) and (b) $T_s = 0.075\,\mathrm{m}$ (3 in). 114
5-22 Normalized ultimate live load versus normalized crack opening, for $T_s = 0.10\,\mathrm{m}$ (4 in). 115
5-23 3-D model-based investigation of transfer of prestressing: employed mesh with boundary conditions. 116
5-24 Plastic strain distribution in critical region after prestress application. 117
5-25 (a) Mesh of girder with rounded corner, (b) Plastic strain distribution after prestress application. 118
5-26 Location of design truck load HS-20 for maximum negative moment: P_{w1} and P_{w2} correspond to the front and back wheel load. The (non-load bearing) wearing surface load g_2 and the uniform lane load p_2 are not shown in the figure. 120
5-27 2-D finite element simulation of the prestressing phase (prior to establishment of continuity at support). Top: Deformed Shape with rotational discontinuity over support. Bottom: Longitudinal stress distribution around mid-support, showing that there is no stress transfer between the two girders during prestress application. 120
5-28 2-D Model-based results of continuous UHPC beam: (a-b) Deformed shape and plastic strain distribution over support at 15% ULS live load level; (c-d) Same for the 100% ULS live load level. 121
5-29 2-D Model-based results of continuous UHPC beam over mid support (negative moment) for 15% and 100% ULS live load level: (a) Longitudinal composite matrix plastic strains $\varepsilon^p_{M,xx}$ along the height of the girder, (b) Longitudinal stresses Σ_{xx} along the height of the girder. 123
5-30 2-D Model-based results of continuous UHPC beam in field (positive moment) for 15% and 100% ULS live load level: (a) Longitudinal composite matrix plastic strains $\varepsilon^p_{M,xx}$ along the height of the girder, (b) Longitudinal stresses Σ_{xx} along the height of the girder. 124

Chapter 1

INTRODUCTION

1.1 Industrial Context

Highways are a key element of our infrastructure, and the demand for highway capacity increases annually with economic growth and increase in population. Vehicle miles of travel on US highways increases by more than two percent each year (Fig. 1-1) [17]. However, for both economic and ecological reasons, the construction of new highways does not keep up with the demand, resulting in a gradual saturation of the existing highway system. In addition, the existing highways and highway bridges are facing severe deterioration problems. Data from the National Bridge Inventory indicate that about 30% of the highway bridges are either structurally deficient or functionally obsolete [34]. This structural deficiency compromises the overall cost effectiveness of our transportation system as it affects the wear-and-tear of vehicles, fuel consumption, transportation related emissions, congestion from expanded work zones for maintenance, travel time, public safety, etc. The next generation of highway bridges must address these issues in the following ways [2]:

- Longer life spans with higher durability and less maintenance;
- Adaptability to new traffic;
- Improved reliability and safety, as well as immunity to extreme events;
- Environmental friendliness;

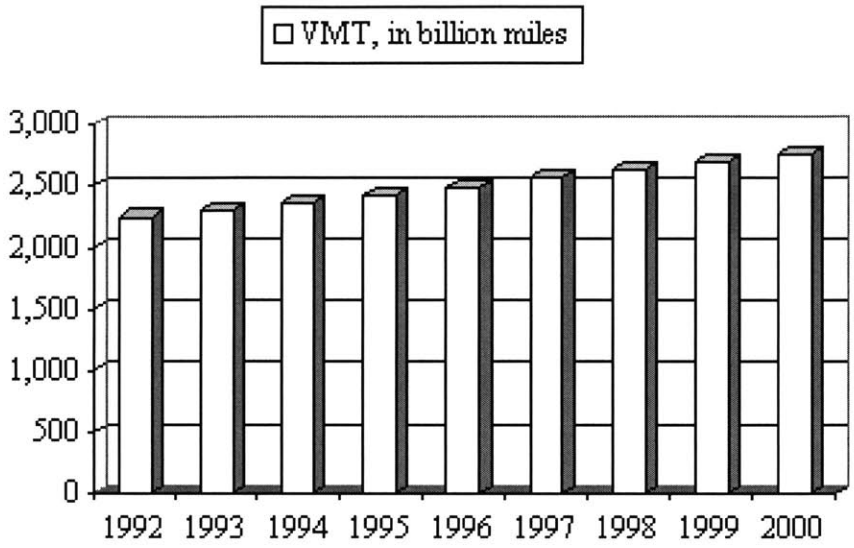

Figure 1-1: Annual vehicle miles of highway travel (years 1992 - 2000) [17].

- Easier and faster construction.

One way of achieving these goals is through the introduction of new improved construction materials. Since concrete is by far the most commonly used material for highway bridges – 60% of all US highway bridges and 40% of deteriorated bridges are made of concrete [34] – improved concrete solutions are critical to the aforementioned improvements.

One new concrete solution currently emerging on the market is Ultra High Performance Concrete (UHPC). UHPC is a new generation of fiber reinforced cementitious material composed of Portland cement, silica fume, mineral fillers, fine silica sand, superplasticizer, water, and steel fibers. A typical UHPC material has a design compressive strength of $f'_c = 200\,\text{MPa}$ (29ksi) and a ductile tensile strength of $f'_t = 10 - 15\,\text{MPa}$ (1.5 ksi – 2.2 ksi), which are achieved by optimizing both the packing density of the matrix and the length-diameter spectrum of the steel fiber reinforcement [4,16,36]. Because of the material's ability to dissipate energy through superior bonding between the matrix and the fiber, UHPC structures are capable of deforming and supporting flexural and tensile loads even after initial cracking. Figure 1-2 displays the exceptional flexural strength of UHPC in comparison to that of normal concrete. This capacity allows the use of UHPC in bridge girders without passive reinforcement or shear stirrups, saving labor and cost (see Fig. 1-3). The high strength of UHPC can also allow smaller sec-

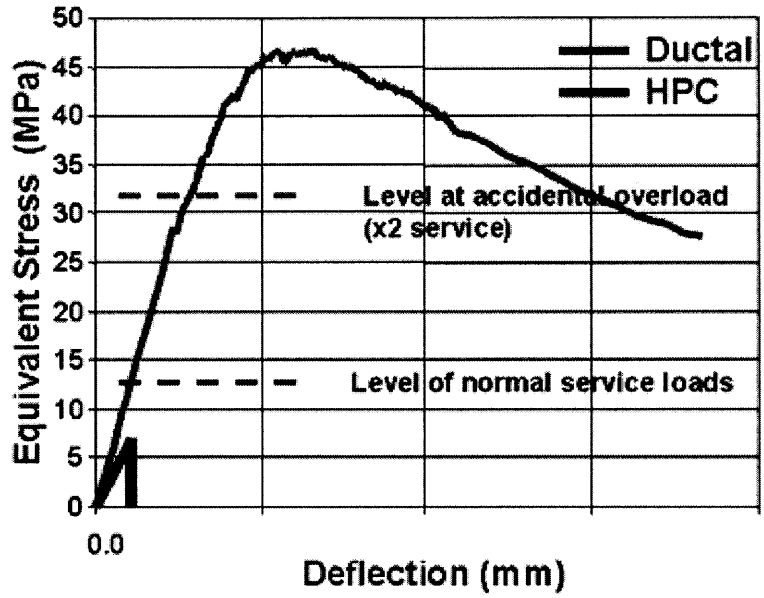

Figure 1-2: Comparison of the flexural strengths of UHPC (DUCTAL^{TM}) and conventional concrete (HPC) [4].

tion sizes, reducing construction time and work crews. UHPC girders are capable of spanning longer distances and mitigating disturbance to ecosystems and natural habitats. Finally, the low permeability and porosity of UHPC leads to high durability and a superior resistance to corrosive attack. Therefore, UHPC material may be a solution to current problems in highway systems.

1.2 Background and Research Significance

Since UHPC has entered the market, several applications of UHPC have been realized. These include the world's first UHPC bridge on the Bourg lès Valence bypass in Drôme, France (2002) [39], a pedestrian bridge in Seoul, Korea that spans 120 m (394 ft) with a deck only 3 cm (1.2 in) thick (2002) [8], a pedestrian/bike bridge in Sherbrooke, Canada (1997) [1], as well as some non-structural applications such as wall panels and safety vaults [35].

In the United States, the Federal Highway Administration (FHWA) has initiated research into innovative bridge systems in which UHPC plays a prominent role. For example, two

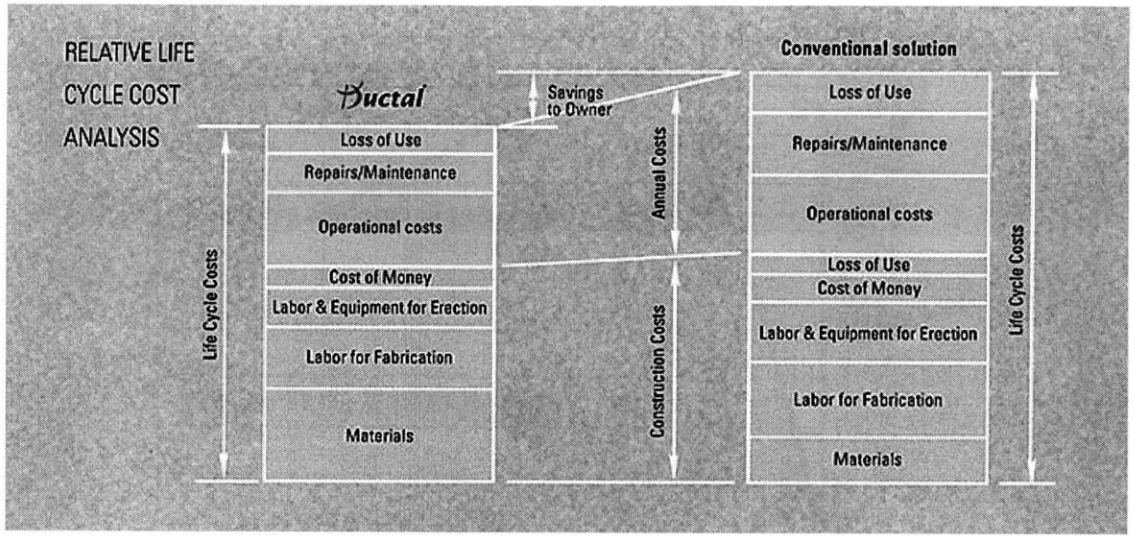

Figure 1-3: Economic benefits from using UHPC (DUCTAL^{TM}); Case study of a 19m wide, 2 km long four-lane bridge design for automobile travel [29].

large-scale structural UHPC beam girder tests were performed at the FHWA Turner-Fairbank Highway Research Center in McLean, Virginia (2001-2002). Without passive reinforcement or shear stirrups, the prestressed beams displayed superior flexural and shear resistance over normal strength prestressed concrete, which underscored the great potential of this new material for large-scale structural applications [18, 19, 30].

The sections employed were derived from standard AASHTO Type II girder sections in which reinforced concrete was replaced by unreinforced UHPC. That is, neither the superior compressive strength of UHPC nor the ductile tensile strength of UHPC were considered in the section design. Ideally, UHPC girders would exploit the material's superior mechanical behavior with economic section design, e.g. minimizing cross-sectional area while maximizing structural performance.

1.3 Research Objectives and Approach

The recent development of UHPC is based on advances in the materials science of cementitious materials, producing materials with improved mechanical and durability properties. Given the progress and potential of these materials, it is unfortunate that the application of UHPC in

the building and construction industry has lagged behind. Considerable effort is required to translate and implement the knowledge gained on the material level into structural engineering and design. Reaching this goal requires research into the link between the *in situ* behavior of the materials and the resulting structural performance. Aside from empirical approaches, based on large-scale testing of structures, recent progress in constitutive modeling of materials and model-based simulation can considerably contribute to attaining this goal. In fact, an appropriate material model for UHPC allows simulation of the behavior of the material. Furthermore, the implementation of this model in an advanced computational mechanics environment (such as the one offered by the finite element method) provides the assessment of the *in situ* behavior of the material by means of model-based structural simulations [12]. With these developments, it is possible to either optimize a material for a given structure [33], or *vice versa*, optimize a structure or structural element for a given material. The research results reported here contribute to the second objective and, more generally, demonstrate the beneficial use of model-based simulation for facilitating implementation of material innovation in structural engineering.

To address this objective, we develop a rational methodology for model-based optimization of structures made of UHPC and implement this methodology for the design of optimized UHPC bridge girder sections. Our approach follows a natural progression from a simple 1-D section design formula to sophisticated 2-D and 3-D computational modeling of UHPC structures.

At the core of our approach is a two-phase constitutive model for UHPC, developed in recent years at M.I.T. [14], which allows the model-based simulation of UHPC structures in two and three dimensions and which can complement or replace expensive structural tests in many ways. The model has been validated for different UHPC structural applications, namely the FHWA flexural and shear tests [13]. The key finding of the model validation is that it is possible to capture, with one model parameter set, both the structural behavior (force-displacement relation) and local *in situ* material behavior (strain gage measurements and cracking behavior) of differently sized UHPC structural members for both service conditions and the ultimate limit state. The validation of the model, therefore, allows us to use the model as a reliable engineering tool for model-based optimization of UHPC structures.

The optimization of a design solution first requires the adoption of appropriate design criteria for UHPC structures subjected to a specific loading. In contrast to standard reinforced concrete

design criteria, based primarily on maximum material strength criteria, UHPC design criteria should be based on a critical crack opening below which the material achieves its tensile strength capacity with high confidence. In this research, we adapt the maximum crack opening criterion issued by the French Association of Civil Engineering (AFGC[1]) [38], and show its employment for model-based simulations.

By way of application, we systematically explore in a quantitative and analytical fashion the best combination of the superior mechanical performance of UHPC materials and efficient structural shapes for highway bridge girders by considering both the service state and the ultimate limit state. In particular, we examine the efficiency of precast double-tee girders for single span and two span bridges in the $21-36\,\mathrm{m}$ ($70-120\,\mathrm{ft}$) span range. For this application, we define the design space, design criteria, and design parameters and illustrate in a quantitative fashion the model-based optimization procedure.

1.4 Outline of the Report

This work is divided into six chapters, starting with the UHPC material model and model validation, moving on to the model-based optimization, and finishing with the choice of optimized sections for UHPC bridge girder sections. Chapter 2 begins with a brief review of the two-phase constitutive model for UHPC material and the model input parameters. The two-phase model structure is based on the material composition with one phase representing the matrix, the other the reinforcing fibers. This separation of the overall composite behavior into individual composite matrix and composite fiber behaviors will be particularly important with regard to the aforementioned crack opening design criterion, because the crack opening is only associated with the matrix phase. In Chapter 3, the effectiveness of the model and its implementation in a commercial finite element program is validated with experimental data as given by the FHWA flexure test and the FHWA shear test. In the same chapter, we illustrate the applicability of the maximum crack opening criterion issued by the French Association of Civil Engineering with model-based simulation results of the FHWA structural tests.

Chapter 4 is devoted to the development of the model-based optimization methodology

[1] Association Française de Génie Civil

for UHPC sections. Inspired by standard prestressed concrete design, we adopt a zero crack opening criterion for the service state and a maximum crack opening criterion for unreinforced and reinforced UHPC members for the ultimate limit state. The design procedure is illustrated with the development of a simple 1-D engineering formula (based on section equilibrium) for UHPC section design. The load cases for bridge girders, including partial security factors, are presented and primary design parameters for bridge girder sections are determined.

Chapter 5 shows the detailed application of the optimization methodology for UHPC bridge girders in the $21 - 36\,\mathrm{m}$ ($70 - 120\,\mathrm{ft}$) span range. The chapter begins with a review of section profiles suitable for the span range. Choosing double-tee girders, we validate the 1-D design formula with detailed two-dimensional and three-dimensional finite element simulations. For two levels of prestressing, $4.45\,\mathrm{MN}$ ($1,000$ kips) and $6.68\,\mathrm{MN}$ ($1,500$ kips), we determine minimum section dimensions for the slab, flange, and web that satisfy the crack-opening design criteria of the service and ultimate limit states. The suitability of the sections for two-span continuous beams is also discussed, as well as the feasibility of the sections with regard to the prestressing level. The results of the optimization procedure are then summarized in the form of optimized girder sections for the considered span range. Finally, the sections are compared with conventional concrete solutions, highlighting the advantages offered by UHPC girder sections.

In this way, a critical review of the proposed design methodology for UHPC bridge girders is presented and future research and engineering challenges for the implementation of UHPC in bridge engineering design practice are addressed.

Part I

UHPC-MODEL AND MODEL VALIDATION

Chapter 2

UHPC MATERIAL MODEL

The main challenge in modeling the behavior of fiber reinforced cementitious composites is to distinguish, in the overall composite response, the brittle behavior of the cementitious matrix from the ductile contribution of the reinforcing fibers and their shared interface. This is even more important for ultra-high performance cementitious composites (UHPC) which achieve a high ductile tensile strength as a result of an optimized match of high strength cementitious matrix and high strength fibers, and the possibility of continuous stress transfer from matrix to fiber over the common interface after initial matrix cracking [11]. Hence, a material model which separates, at the macroscopic level, the matrix phase from the fiber phase is critical for a realistic description of the *in situ* behavior of UHPC. This chapter reviews such a model, recently developed at M.I.T. The model is a two-phase model based on the material composition with one-phase representing the matrix, the other the reinforcing fibers. In addition, the matrix-fiber interaction is taken into account as internal cross-effects between the irreversible deformations of the composite constituents. This model, which will be validated in the Chapter 3, is at the core of the model-based optimization procedure for UHPC structures developed in this research. In particular, the model's separation of the overall composite behavior into a composite matrix and a composite fiber will turn out to be particularly important for the assessment of the crack opening in the matrix, which will be employed in the latter chapters as a design criterion. This chapter is structured as follows: the 1-D and 3-D versions of the model are presented first, along with a brief review of the ductile versus brittle energy transformations of UHPC captured by the model. The model input parameters are derived from a notched tensile plate test for a

particular UHPC material, DUCTAL^{TM}, which will be considered throughout this study.

2.1 1-D UHPC Model

Composite mechanics provides a suitable means of studying the material behavior of the composite material, particularly the capacity of the material to transfer stresses after cracking from the matrix to the fibers over their common interface. We can distinguish three composite mechanics approaches aimed at modeling the complex mechanisms acting in composite materials when subjected to mechanical loading:

- Micromechanics of stress transfer, yield, and fracture including interface shear, debonding, friction, and sliding (see, among many others, [9, 23, 27]), which has also been applied to cementitious composites (e.g. [26, 31, 32, 37, 40]; for a comprehensive review see [13]). These micromechanical models allow one to show that UHPC materials, in contrast to standard FRCC materials, are an optimized mechanical match of two materials and their interactions [11].

- Phenomenological continuum mechanics formulations in which the irreversible deformation of the matrix, fiber, and interface are taken into account by means of some macroscopic damage variables (e.g., [10, 21, 28]).

- Multiphase models for composite materials, in which matrix and fiber are considered as two distinct phases with distinct kinematics and a possible mechanical interaction (e.g., [15, 24]).

The model we consider here is part of the class of multiphase models which distinguish different phases and their interface in the overall composite response; i.e. the brittle behavior of the cementitious matrix and the ductile contribution of the reinforcing fibers. The micromechanical models based on fracture and/or yield approaches form the backbone of the UHPC model considered here, which is macroscopic in nature. In this way, UHPC is modeled in a continuous fashion, i.e. through the various stages of damage evolution.

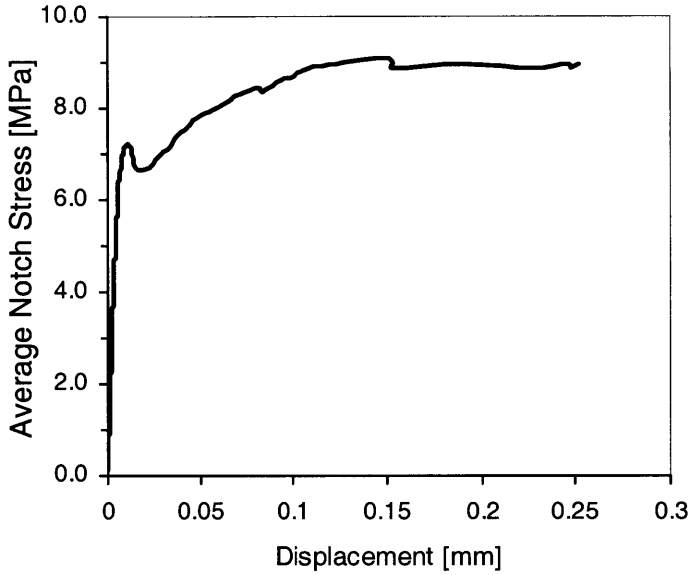

Figure 2-1: Typical stress-crack opening response of a UHPC material; results from notched tensile test [7].

2.1.1 1-D Think Model of UHPC Material Behavior

A typical tensile response of a UHPC material composed of a brittle matrix reinforced by a ductile fiber material is sketched in Figure 2-1: following an initial elastic response, the matrix cracks first, characterized by a macroscopic stress drop in a strain driven experiment. Following this stress drop, a pseudo-strain hardening stage is exhibited, until the composite material yields and eventually fails. The 1-D Think Model displayed in Figure 2-2 was proposed by Chuang and Ulm [14] to capture the characteristic features of such a composite behavior. The device is composed of two parallel subdevices, which represent the macroscopic behaviors of the composite constituents, that is the matrix and fibers. An elastic spring (stiffness C_M) and a brittle-plastic crack device (crack strength f_t, frictional strength k_M) model the elastic brittle-plastic behavior of the composite matrix. The composite fiber behavior is governed by an elasto-plastic material law, described by an elastic spring (stiffness C_F) in series with a friction element (strength f_y). Additionally, the two parallel elements are coupled by an elastic spring of stiffness M, which links the irreversible matrix behavior (strain ε_M^p) with the irreversible fiber reinforcement behavior (strain ε_F^p). These 6 model parameters $(C_M, C_F, M, f_t, k_M, f_y)$

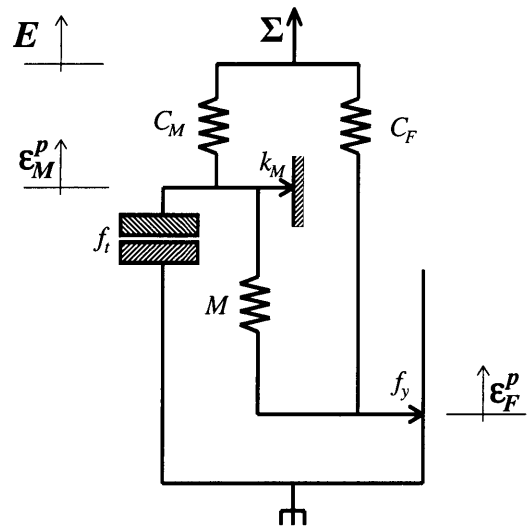

Figure 2-2: 1D Think Model of a two-phase matrix-fiber composite material [14].

govern the composite material behavior.

2.1.2 Constitutive Relations

The macroscopic stress Σ is composed of composite stresses σ_M and σ_F, representing the stresses acting on the matrix crack element and the fiber frictional device, respectively:

$$\Sigma = \sigma_M + \sigma_F \tag{2.1}$$

where

$$\begin{pmatrix} \Sigma \\ \sigma_M \\ \sigma_F \end{pmatrix} = \begin{bmatrix} C_M + C_F & -C_M & -C_F \\ C_M & -(C_M + M) & M \\ C_F & M & -(C_F + M) \end{bmatrix} \begin{pmatrix} E \\ \varepsilon_M^p \\ \varepsilon_F^p \end{pmatrix} \tag{2.2}$$

E is the total strain, ε_M^p is the permanent strain associated with composite matrix cracking (opening of the crack element in Fig. 2-2), and ε_F^p the permanent strain associated with permanent composite fiber deformation. From elementary equilibrium considerations, the composite

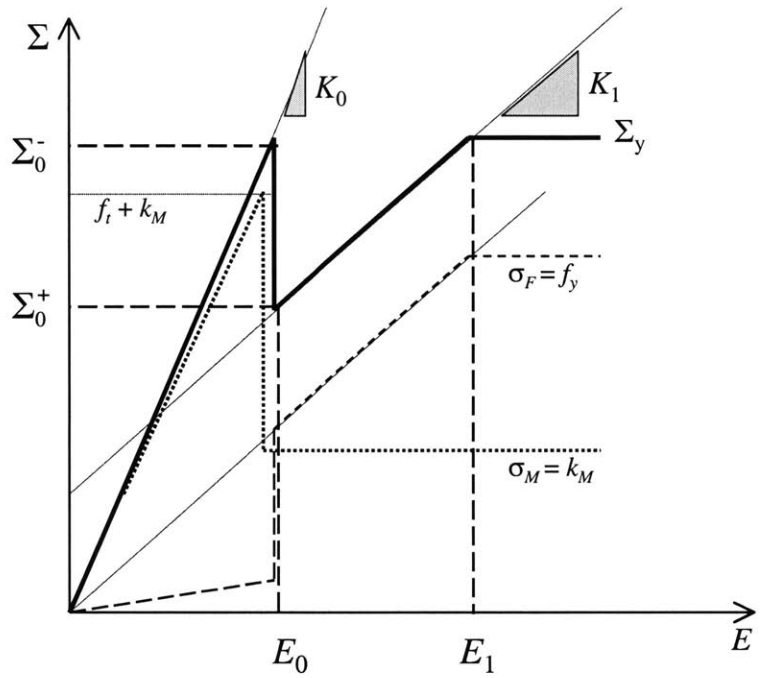

Figure 2-3: Stress-strain response of the two-phase composite model [14].

stresses, σ_M and σ_F, are constrained by the following loading functions:

$$F(\sigma_M, \sigma_F) = \max(f_M(\sigma_M), f_F(\sigma_F)) \leq 0 \tag{2.3}$$

The initial elasticity is defined by:

$$\begin{aligned} f_M(\sigma_M) &= \sigma_M - (f_t + k_M) \\ f_F(\sigma_F) &= |\sigma_F| - f_y \end{aligned} \tag{2.4}$$

while the following Kuhn-Tucker conditions describe the loading-unloading conditions after crack opening:

$$\sigma_M - k_M \leq 0; \;\; \varepsilon_M^p \geq 0; \;\; (\sigma_M - k_M)\,\varepsilon_M^p = 0 \tag{2.5}$$

The stress-strain response of the model is displayed in Figure 2-3:

1. In the initial elastic range $\left(\varepsilon_M^p = \varepsilon_F^p = 0\right)$, the overall elasticity is governed by the initial

composite stiffness $K_0 = C_M + C_F$ for

$$F(\sigma_M, \sigma_F) < 0 \Rightarrow \Sigma = (C_M + C_F) E \tag{2.6}$$

The matrix cracks first provided that:

$$\kappa = \frac{C_F}{C_M} < \frac{f_y}{f_t + k_M} \tag{2.7}$$

In this case, the onset of cracking occurs for $E_0 = (f_t + k_M)/C_M$, which corresponds to the following composite stress state:

$$\varepsilon_M^p (E_0)^- = 0; \left\{ \begin{array}{c} \Sigma_0^- = (1+\kappa)(f_t + k_M) \\ \sigma_M^- = f_t + k_M \\ \sigma_F^- = \kappa (f_t + k_M) \end{array} \right\} \tag{2.8}$$

2. Immediately after cracking, in a strain driven experiment, the crack opening strain and the composite stress state read:

$$\varepsilon_M^p (E_0)^+ = \frac{f_t}{C_M + M}; \left\{ \begin{array}{c} \Sigma_0^+ = \Sigma_0^- - \frac{C_M}{C_M+M} f_t \\ \sigma_M^+ = \sigma_M^- - f_t = k_M \\ \sigma_F^+ = \sigma_F^- + \frac{M}{C_M+M} f_t \end{array} \right\} \tag{2.9}$$

After cracking, the permanent matrix strain is governed by:

$$d\varepsilon_M^p = \frac{C_M}{C_M + M} dE \tag{2.10}$$

and the composite stresses by:

$$d\Sigma = d\sigma_F = K_1 dE; \; d\sigma_M = 0$$

where K_1 is the tangential stiffness:

$$K_1 = C_M + C_F - \frac{C_M^2}{C_M + M} \tag{2.11}$$

3. The maximum stress the composite can sustain in tension is:

$$\Sigma_y = k_M + f_y \tag{2.12}$$

which is reached, in the strain driven experiment, when:

$$E_1 = \frac{k_M M + f_y (C_M + M)}{C_M M + C_F (C_M + M)} \tag{2.13}$$

Beyond this strain, the composite response is ideal plastic, that is:

$$d\varepsilon_M^p = d\varepsilon_F^p = dE;\ d\Sigma = d\sigma_F = d\sigma_M = 0 \tag{2.14}$$

The 6 model parameters $(C_M, C_F, M, f_t, k_M, f_y)$ can be assessed from the pure macroscopic stress-strain response of the composite material, that is from the macroscopic stiffnesses K_0 and K_1, the stresses Σ_0^-, Σ_0^+ and Σ_y, and one asymptotic assumption [14].

2.1.3 1-D Thermodynamics

Prior to the 3-D extension, it is instructive to examine the model within the framework of thermodynamics of irreversible processes (see e.g. [42]). The starting point for this investigation is the Clausius-Duhem inequality:

$$\varphi dt = \Sigma dE - d\psi \geq 0 \tag{2.15}$$

which states that the part of the external (i.e. controllable) work supply, ΣdE, which is not stored as free energy ψ in the system is dissipated into heat form. The free energy ψ is a function of the state variables, the total strain E, and the permanent composite strains ε_M^p and ε_F^p. The free energy is the elastic energy stored in the springs of the model in Figure 2-2, that is:

$$2\psi\left(\varepsilon, \varepsilon_M^p, \varepsilon_F^p\right) = C_M\left(E - \varepsilon_M^p\right)^2 + C_F\left(E - \varepsilon_F^p\right)^2 + M\left(\varepsilon_M^p - \varepsilon_F^p\right)^2 \tag{2.16}$$

Use of the free energy expression in the Clausius-Duhem inequality delivers:

$$\varphi dt = \sigma_M d\varepsilon_M^p + \sigma_F d\varepsilon_F^p \geq 0 \tag{2.17}$$

along with the state equations:

$$\Sigma = \frac{\partial \psi}{\partial \varepsilon} = (C_M + C_F)\, E - C_M \varepsilon_M^p - C_F \varepsilon_F^p \tag{2.18}$$

$$\sigma_M = -\frac{\partial \psi}{\partial \varepsilon_M^p} = C_M E - (C_M + M)\, \varepsilon_M^p + M \varepsilon_F^p \tag{2.19}$$

$$\sigma_F = -\frac{\partial \psi}{\partial \varepsilon_F^p} = C_F E + M \varepsilon_M^p - (C_F + M)\, \varepsilon_F^p \tag{2.20}$$

We note:

1. The overall elastic composite stiffness $K_0 = C_M + C_F$ is derived from:

$$K_0 = \frac{\partial \Sigma}{\partial E} = \frac{\partial^2 \psi}{\partial E^2} \tag{2.21}$$

and the composite stiffnesses are defined by the Maxwell symmetry relations:

$$C_M = -\frac{\partial \Sigma}{\partial \varepsilon_M^p} = \frac{\partial \sigma_M}{\partial E} = -\frac{\partial^2 \psi}{\partial E \partial \varepsilon_M^p} \tag{2.22}$$

$$C_F = -\frac{\partial \Sigma}{\partial \varepsilon_F^p} = \frac{\partial \sigma_F}{\partial E} = -\frac{\partial^2 \psi}{\partial E \partial \varepsilon_F^p} \tag{2.23}$$

Analogously, the coupling modulus is derived from:

$$M = \frac{\partial \sigma_M}{\partial \varepsilon_F^p} = \frac{\partial \sigma_F}{\partial \varepsilon_M^p} = -\frac{\partial^2 \psi}{\partial \varepsilon_M^p \partial \varepsilon_F^p} \tag{2.24}$$

The matrix-fiber coupling modulus represents the change in composite matrix stress induced by unit of irreversible composite fiber deformation, and vice versa. These matrix-fiber cross-effects (or thermodynamic couplings) maintain the stress additivity of the macroscopic stress, $\Sigma = \sigma_M + \sigma_F$.

2. The energy approach allows us to formally identify the composite stresses σ_M and σ_F as the thermodynamic forces of the irreversible composite matrix and fiber deformation.

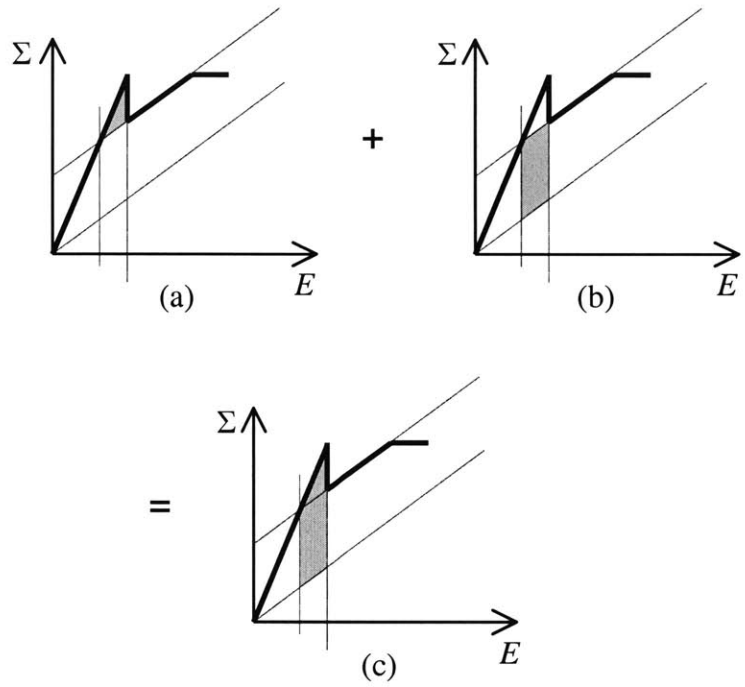

Figure 2-4: Two sources of energy dissipation upon cracking of brittle-plastic composite material [14]: (a) brittle fracture, (b) frictional dissipation, (c) total dissipation.

Unlike the total stress Σ, these composite stresses are not related by equilibrium to external forces, but represent driving forces of the dissipation, i.e. the transformation of externally supplied energy (ΣdE) into heat form.

2.1.4 Energy Transformation during Brittle-Plastic Fracture

In a strain driven experiment, in which the macroscopic strain is frozen during the brittle fracture (i.e. $dE = 0$), the part of the energy which is dissipated $\mathcal{D}$ equals the jump in free energy. Thus, from (2.15):

$$\mathcal{D} = \int_{s=t_o^-}^{s=t_0^+} \varphi ds = -[[\psi]] = \frac{1}{2}\frac{f_t^2}{C_M + M}\left(1 + 2\frac{k_M}{f_t}\right) \geq 0 \tag{2.25}$$

The total dissipation upon matrix cracking is comprised of two terms: one associated with pure matrix cracking (dissipation of f_t upon crack element opening),

$$-[[\psi]]_c = \frac{1}{2}\frac{f_t^2}{C_M + M} \geq 0 \tag{2.26}$$

and one associated with friction mechanism activated upon cracking (dissipation upon crack element opening of friction strength k_M along $0 \rightarrow \varepsilon_M^p\,(E_0)^+$):

$$-[[\psi]]_M = k_M \varepsilon_M^p\,(\varepsilon_0)^+ = k_M \frac{f_t}{C_M + M} = -2[[\psi]]_c \frac{k_M}{f_t} \geq 0 \tag{2.27}$$

These two sources of dissipation in brittle-plastic composites are displayed in Figure 2-4. In addition to the dissipation of energy by creation of fracture surface, an additional residual matrix strength is activated during matrix cracking, which dissipates energy in subsequent loading. The ratio of these two sources of dissipation can be used to quantify the ductility of UHPC material solutions upon first cracking:

$$\mathcal{R}_D = \frac{-[[\psi]]_M}{-2[[\psi]]_c} = \frac{k_M}{f_t} \tag{2.28}$$

We note that $R_D = 0$ for a pure elastic brittle matrix reinforced by fibers (e.g. poor FRCC materials), while $R_D \sim 10$ for typical UHPC materials. This highlights, at the macroscopic scale, that UHPC upon first cracking primarily dissipates the released energy by frictional mechanisms which ultimately lead to the apparent strain hardening and highly ductile behavior of these materials.

2.2 3-D UHPC Model

The 1-D UHPC model of Section 2.1 extends to three-dimensions by replacing the 1-D scalar quantities by their tensorial 3-D counterparts and the 1-D loading functions by appropriate 3-D strength criteria for the composite matrix and fiber. The starting point of this extension is the 3-D expression of the Clausius-Duhem inequality:

$$\varphi dt = \underline{\underline{\Sigma}} : d\underline{\underline{E}} - d\psi \geq 0 \tag{2.29}$$

where $\underline{\underline{\Sigma}} : d\underline{\underline{E}}$ represents the external work supply in 3-D, while the free energy ψ reads now as a function of the strain tensor $\underline{\underline{E}}$, the composite matrix plastic strain $\underline{\underline{\varepsilon}}_M^p$ representing cracking, and the composite fiber plastic strain $\underline{\underline{\varepsilon}}_F^p$. With similar reasoning as employed in the 1-D case, we arrive at:

$$\varphi dt = \underline{\underline{\sigma}}_M : \underline{\underline{\varepsilon}}_M^p + \underline{\underline{\sigma}}_F : \underline{\underline{\varepsilon}}_F^p \geq 0 \tag{2.30}$$

along with the 3-D counterparts of the 1-D state equations (2.18) to (2.20):

$$\begin{pmatrix} \underline{\underline{\Sigma}} \\ \underline{\underline{\sigma}}_M \\ \underline{\underline{\sigma}}_F \end{pmatrix} = \begin{bmatrix} \mathbb{C}_M + \mathbb{C}_F & -\mathbb{C}_M & -\mathbb{C}_F \\ \mathbb{C}_M & -(\mathbb{C}_M + \mathbb{M}) & \mathbb{M} \\ \mathbb{C}_F & \mathbb{M} & -(\mathbb{C}_F + \mathbb{M}) \end{bmatrix} : \begin{pmatrix} \underline{\underline{E}} \\ \underline{\underline{\varepsilon}}_M^p \\ \underline{\underline{\varepsilon}}_F^p \end{pmatrix} \tag{2.31}$$

Here, $\underline{\underline{\sigma}}_M$ and $\underline{\underline{\sigma}}_F$ still represent the driving forces of matrix cracking and fiber yielding, respectively; which satisfy the stress additivity relation:

$$\underline{\underline{\Sigma}} = \underline{\underline{\sigma}}_M + \underline{\underline{\sigma}}_F \tag{2.32}$$

In turn, the general 3-D constitutive relations involve 3×21 stiffness parameters associated with the forth order stiffness tensors $\mathbb{C}_M$, $\mathbb{C}_F$ and $\mathbb{M}$:

$$\mathbb{C}_M = -\frac{\partial^2 \psi}{\partial \underline{\underline{E}} \partial \underline{\underline{\varepsilon}}_M^p}; \; \mathbb{C}_M = -\frac{\partial^2 \psi}{\partial \underline{\underline{E}} \partial \underline{\underline{\varepsilon}}_F^p}; \; \mathbb{M} = -\frac{\partial^2 \psi}{\partial \underline{\underline{\varepsilon}}_M^p \partial \underline{\underline{\varepsilon}}_F^p} \tag{2.33}$$

2.2.1 3-D Isotropic Elasticity Properties

The number of elasticity constants decreases significantly when considering specific matrix behavior and specific fiber orientations. For example, fiber reinforced materials with random fiber orientation can be estimated to act isotropically. Accordingly, the separate behaviors of the cementitious matrix and the randomly oriented reinforcing fibers can be approximated to be isotropic. In this case, $\mathbb{C}_M$ and $\mathbb{C}_F$ can each be described with two unique scalar values:

$$\mathbb{C}_i = 3K_i\mathbb{K} + 2G_i\mathbb{J}; \; \left\{ \begin{array}{c} K_i = \frac{C_i}{3(1-2\nu_i)} \\ G_i = \frac{C_i}{2(1+\nu_i)} \end{array} \right\} i = M, F \tag{2.34}$$

where $K_{ijkl} = \frac{1}{3}\delta_{ij}\delta_{kl}$ is the volumetric part of the 4th order unit tensor $\mathbb{I}$, and $\mathbb{J} = \mathbb{I} - \mathbb{K}$ is the deviatoric part; G_F and G_M are the shear moduli of the composite fiber and matrix; K_F and K_M are the bulk moduli of the composite fiber and matrix; ν_F and ν_M are the Poisson's ratio of the composite fiber and matrix, but for the sake of simplicity, it will be assumed from this point $\nu_F = \nu_M \equiv \nu$, where ν is the overall composite Poisson's ratio.

Analogously, the assumption of randomly oriented cracks after matrix cracking suggests the following isotropic form of the matrix-fiber coupling tensor $\mathbb{M}$:

$$\mathbb{M} = \frac{M^{3D}}{1-2\nu}\mathbb{K} + \frac{M^{3D}}{1+\nu}\mathbb{J} \tag{2.35}$$

where M^{3D} is the 3-D counterpart of the 1-D coupling modulus M. Unlike the composite fiber and composite matrix stiffnesses, the 3-D coupling stiffness tensor $\mathbb{M}$ is not directly related to its 1-D counterpart M. Instead, the 3-D coupling behavior (stiffness tensor) must be formulated in such a way that the 3-D model would give the same macroscopic uniaxial response (and thermodynamic response) as the 1-D model, a 1-D consistency condition. While relation (2.34), by definition, requires $\mathbb{C}_M$ and $\mathbb{C}_F$ to adhere to this 1-D consistency condition, the model parameter M^{3D} must also be solved from this 1-D consistency condition as well. Chuang and Ulm [13] derived the following expression:

$$M^{3D} = \beta M + (\beta - 1)\frac{C_M C_F}{(C_M + C_F)} \tag{2.36}$$

For $\beta = 1$, $M^{3D} = M$, while a refined analysis yields:

$$\beta_I = \frac{\left(\alpha_M^{UN} + \sqrt{\frac{2}{3}}\right)^2 (1-2\nu)(1+\nu)}{3\left(\alpha_M^{UN}\right)^2 (1+\nu) + (1-2\nu)} \tag{2.37}$$

where α_M^{UN} is the friction coefficient of the matrix, which is a function of the matrix compressive and tensile strength, σ_{Mc} and $\sigma_{Mt} = f_t + k_M$, as detailed in the following section:

$$\alpha_M^{UN} = \sqrt{\frac{2}{3}}\frac{\sigma_{Mc} - \sigma_{Mt}}{\sigma_{Mc} + \sigma_{Mt}} \tag{2.38}$$

2.2.2 3-D Strength Domain

The overall 3-D strength domain $\mathcal{D}_E$ of the composite material is defined for the composite stresses $\underline{\underline{\sigma}}_M$ and $\underline{\underline{\sigma}}_F$, that is:

$$\begin{gathered} \underline{\underline{\Sigma}} \in \mathcal{D}_E \\ \Updownarrow \\ \left(\begin{array}{c} \underline{\underline{\sigma}}_M \in \mathcal{D}_M \Leftrightarrow F_M = \max f_M \left(\underline{\underline{\sigma}}_M \right) \leq 0 \\ \underline{\underline{\sigma}}_F \in \mathcal{D}_F \Leftrightarrow F_F = \max f_F \left(\underline{\underline{\sigma}}_F \right) \leq 0 \end{array} \right) \end{gathered} \tag{2.39}$$

where $\mathcal{D}_M$ and $\mathcal{D}_F$ denote the strength domains of the composite matrix and the composite fiber, respectively. These strength domains are expressed in 3-D by a set of loading functions, F_M and F_F, that are the analogous to the 1-D loading functions, f_M and f_F, defined by (2.4).

The composite strength domains $\mathcal{D}_M$ and $\mathcal{D}_F$, are represented with combinations of two types of loading functions: the tension cut-off criterion (TC) and the Drucker-Prager criterion (DP). These loading functions represent isotropic strength domains. The TC loading surface is defined by:

$$f^{TC} = I_1 - \sigma^{TC} \tag{2.40}$$

and the DP reads:

$$f^{DP} = \alpha I_1 + \left| \underline{\underline{s}} \right| - c^{DP} \tag{2.41}$$

where $\left| \underline{\underline{s}} \right| = \sqrt{s_{ij} s_{ij}}$ refers to the magnitude of the stress deviator; α, σ^{TC}, and c^{DP} are material parameters.

Composite Matrix Strength Domain

Following the form of the 1-D UHPC model, the composite matrix is assigned a brittle-plastic 3-D strength domain, the composite fiber an elasto-plastic strength domain. The composite matrix captures an elastic-brittle behavior with a higher initial (uncracked) limit, and a lower yield limit after cracking. This strength domain is described by 6 characteristic values, listed as absolute values:

1. The initial tensile strength, σ_{Mt}. By definition, this must be the same as the matrix

cracking strength of the 1-D UHPC model:

$$\sigma_{Mt} = f_t + k_M \tag{2.42}$$

2. The initial compressive strength, σ_{Mc}.

3. The initial biaxial compressive strength, σ_{Mb}.

4. The post-cracking tensile yield strength, σ_{Mt}^{cr}. This is equivalent to the 1-D composite matrix post-cracking strength k_M:

$$\sigma_{Mt}^{cr} = k_M \tag{2.43}$$

5. The post-cracking compressive yield strength, σ_{Mc}^{cr}.

6. The post-cracking biaxial compressive yield strength, σ_{Mb}^{cr}.

Before matrix cracking, the initial strength limits (σ_{Mt}, σ_{Mc}, and σ_{Mb}) govern the composite matrix loading functions. To enforce these initial strength limits, a tension cut-off criterion governs the tension-tension stress states f_M^{TC}, one Drucker-Prager criterion governs the compression-tension stress states f_M^{UN}, and another DP governs the compression-compression stress states f_M^{BI}. These criteria are expressed by:

$$f_M^{TC} = I_{1,M} - \sigma_{Mt} \leq 0 \tag{2.44}$$

$$f_M^{UN} = \alpha_M^{UN} I_{1,M} + \left|\underline{\underline{s}}_M\right| - c_M^{UN} \leq 0 \tag{2.45}$$

$$f_M^{BI} = \alpha_M^{BI} I_{1,M} + \left|\underline{\underline{s}}_M\right| - c_M^{BI} \leq 0 \tag{2.46}$$

where

$$\begin{aligned} \alpha_M^{UN} &= \frac{\sqrt{2/3}(\sigma_{Mc}-\sigma_{Mt})}{\sigma_{Mc}+\sigma_{Mt}};\ c_M^{UN} = \left(\sqrt{2/3} - \alpha_M^{UN}\right)\sigma_{Mc} \\ \alpha_M^{BI} &= \frac{\sqrt{2/3}(\sigma_{Mb}-\sigma_{Mc})}{2\sigma_{Mb}-\sigma_{Mc}};\ c_M^{BI} = \left(\sqrt{2/3} - \alpha_M^{BI}\right)\sigma_{Mc} \end{aligned} \tag{2.47}$$

After cracking, the post-cracking strength parameters (σ_{Mt}^{cr}, σ_{Mc}^{cr}, and σ_{Mb}^{cr}) govern the strength domain. As a simplification, it is assumed that the post-cracking composite strengths

are reduced by the same factor, $\rho_D^{cr} = \sigma_{Mt}^{cr}/\sigma_{Mt}$:

$$\sigma_{Mc}^{cr} = \rho_D^{cr}\sigma_{Mc}; \qquad \sigma_{Mb}^{cr} = \rho_D^{cr}\sigma_{Mb} \tag{2.48}$$

With this simplification, the six composite matrix strength parameters (σ_{Mt}, σ_{Mc}, σ_{Mb}, σ_{Mt}^{cr}, σ_{Mc}^{cr}, and σ_{Mb}^{cr}) are effectively reduced to four (σ_{Mt}, σ_{Mc}, σ_{Mb}, and σ_{Mt}^{cr}) while the friction coefficient in the uncracked and cracked states remains the same. The post-cracking loading functions read:

$$f_M^{TC,cr} = I_{1,M} - \sigma_{Mt}^{cr} \leq 0 \tag{2.49}$$

$$f_M^{UN,cr} = \alpha_M^{UN} I_{1,m} + \left|\underline{\underline{s}}_M\right| - c_M^{UN,cr} \leq 0 \tag{2.50}$$

$$f_M^{BI,cr} = \alpha_M^{BI} I_{1,M} + \left|\underline{\underline{s}}_M\right| - c_M^{BI,cr} \leq 0 \tag{2.51}$$

where $c_M^{UN,cr} = \rho_D^{cr} c_M^{UN}$ and $c_M^{BI,cr} = \rho_D^{cr} c_M^{BI}$.

The composite matrix loading functions provided in Eqs. (2.44) to (2.51) are illustrated in the biaxial stress plane in Figure 2-5 and in the $I_1 - \left|\underline{\underline{s}}\right|$ plane in Figure 2-6, respectively. In the uncracked state, Eqs. (2.44) to (2.47) dictate the composite matrix strength domain, as depicted by the dashed lines in Figure 2-6 in the $I_1 - \left|\underline{\underline{s}}\right|$ plane. After cracking, Eqs. (2.49) to (2.51) represent the post-cracking plastic limit, illustrated with the dotted lines in Figure 2-6. In this figure, the composite matrix is loaded in uniaxial tension, uniaxial compression, and biaxial (equibiaxial) compression. Upon achieving its initial strength limit, the composite matrix exhibits a brittle stress drop to its corresponding post-cracking strength. It is this stress drop in the composite matrix which enforces a macroscopic stress drop at first cracking, and which is critical to the assessment of the matrix cracking expressed in terms of the plastic matrix strain $\underline{\underline{\varepsilon}}_M^p$.

Composite Fiber Strength Domain

The elasto-plastic composite fiber is characterized by two strength values in the 3-D space:

1. The tensile strength, σ_{Ft}. This, by definition, is the same as the 1-D fiber strength f_y:

$$\sigma_{Ft} = f_y \tag{2.52}$$

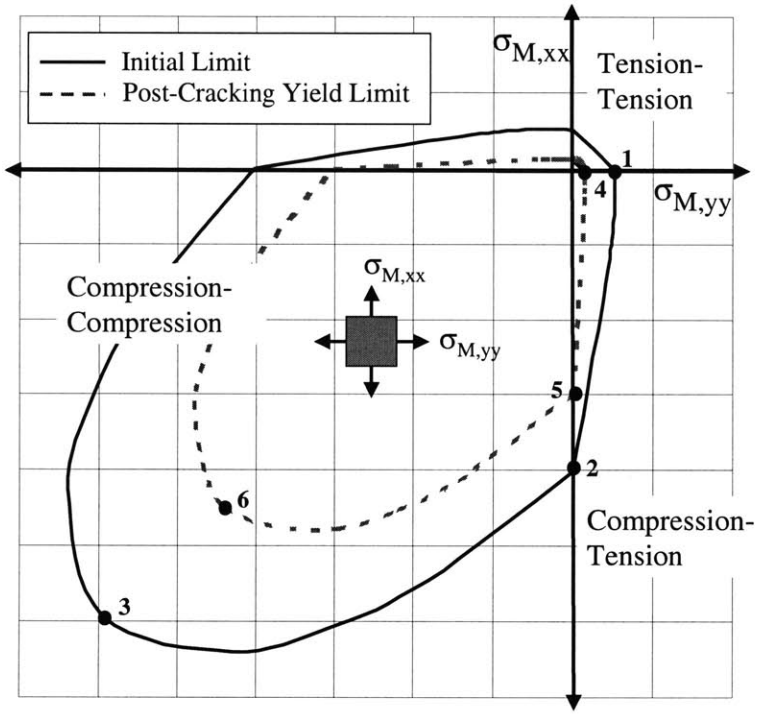

Figure 2-5: Biaxial composite matrix strength domain [12].

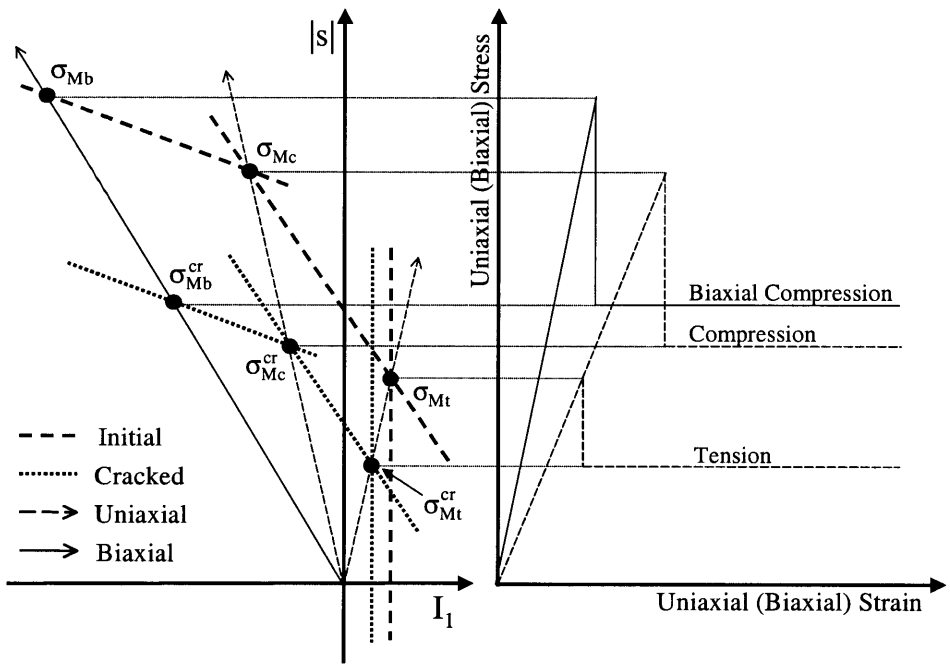

Figure 2-6: Composite matrix strength domain in the $I_1 - |\underline{\underline{s}}|$ the halfplane (left), and stress-strain response (right) [12].

2. The compressive strength, σ_{Fc}.

As a simplifying assumption, a criterion is not specifically designated to limit the composite fiber's biaxial compressive strength σ_{Fb}. Furthermore, unlike the composite matrix, the strength domain of the composite fiber is constant, regardless of the cracking state in the composite matrix. Thus, to enforce the elasto-plastic limits in the tensile-compressive domain, before and after cracking, a TC is employed to limit the tension-tension stress states f_F^{TC}; and a DP is utilized to limit the compression-tension stress states f_F^{DP}:

$$f_F^{TC} = I_{1,F} - \sigma_{Ft} \leq 0 \tag{2.53}$$

$$f_F^{DP} = \alpha_F^{DP} I_{1,F} + \left| \underline{\underline{s}}_F \right| - c_F^{DP} \leq 0 \tag{2.54}$$

where $\alpha_F^{DP} = \sqrt{2/3}\,(\sigma_{Fc} - \sigma_{Ft}) \,/\, (\sigma_{Fc} + \sigma_{Ft})$ and $c_F^{DP} = \left(\sqrt{2/3} - \alpha_F^{DP}\right) \sigma_{Fc}$.

2.3 Summary of the Input Parameters

In this chapter, we reviewed the two-phase UHPC model which will be employed in subsequent chapters for model-based simulations of UHPC structures. The main strength of this model is that it attributes the overall composite behavior, at the macroscopic scale, to a brittle plastic matrix phase and an elasto-plastic fiber phase. It is useful to note that the term 'phase' employed here does not necessarily refer to micromechanical phases in the material at smaller scales. Rather, one may consider the fiber phase as a macroscopic representation of the stiffness (stiffness C_F) and yield capacity (yield strength f_y) that are added to the overall UHPC composite stiffness and strength as a result of reinforcing fibers[1], which is activated (via the coupling spring M) upon matrix cracking.

The virtue of the macroscopic nature of the material model is that all model parameters can be determined from the macroscopic response of UHPC materials. The 3-D composite strength domain $\mathcal{D}_E$ described in Section 2.2.2 can be characterized by six model strength parameters –four composite matrix parameters (σ_{Mt}, σ_{Mt}^{cr}, σ_{Mc}, and σ_{Mb}) and two composite

[1]For instance, the characteristic compressive strength of the composite fiber σ_{Fc} is not the compressive strength of the reinforcing fiber, but represents the compressive capacity added to the UHPC compressive strength by the presence of fibers (see, for example, [25]).

	Description	for UHPC	
		SI	IU
C_M	Composite Matrix Stiffness	53.9 GPa	(7820 ksi)
C_F	Composite Fiber Stiffness	0 GPa	(0 ksi)
M	Composite Interface Stiffness	1.65 GPa	(240 ksi)
ν	Poisson's ratio	0.17	
f_t	Brittle tensile strength of composite matrix	0.7 MPa	(0.1 ksi)
k_M	Post-cracking tensile strength of composite matrix	6.9 MPa	(1 ksi)
σ_{Mc}	Initial compressive strength of composite matrix	190 MPa	(28 ksi)
σ_{Mb}	Initial biaxial compressive strength of composite matrix	220 MPa	(32 ksi)
f_y	Tensile strength of composite fiber	4.6 MPa	(0.67 ksi)
σ_{Fc}	Compressive strength of composite fiber	10 MPa	(1.5 ksi)

Table 2.1: Input parameters of the 3-D UHPC model and typical values for DUCTAL^{TM}, derived from a notched tensile plate test.

fiber parameters (σ_{Ft} and σ_{Fc})– in order to capture six physically observed strength values (Σ_t, Σ_t^{cr}, Σ_c, Σ_c^{cr}, Σ_b and Σ_b^{cr}). In addition, assuming an isotropic elastic behavior of both composite matrix and composite fiber, four additional stiffness parameters (C_M, C_F, M, ν) are required by the state equations. This leads to a total of $4+6=10$ unique model parameters summarized in Table 2.1. The compressive strength values are readily available from the UHPC manufacturer or can be estimated from well accepted data for cementitious materials[2]. Furthermore, the six model parameters that characterize the tensile behavior of UHPC ($C_M, C_F, M, \sigma_{Mt} = f_t + k_M$, $\sigma_{Mt}^{cr} = k_M$, $\sigma_{Ft} = f_y$), should be derived from a tensile notched plate test, which is generally provided by the UHPC manufacturer with high accuracy (and small standard deviation). The rationale behind using notched tensile data is that the notched configuration best reflects – in an average sense – UHPC structural behavior, particularly after cracking. Figure 2-7 displays the results of a notched plate test for DUCTAL^{TM} provided by Lafarge, from which we extract the values of the model parameters in Table 2.1. We will employ these model parameters exclusively in the model-based simulations of this work.

[2]For instance, the biaxial strength of a cementitious matrix σ_{Mb} is well known to be $1.15-1.20$ times higher than the uniaxial strength σ_{Mc}.

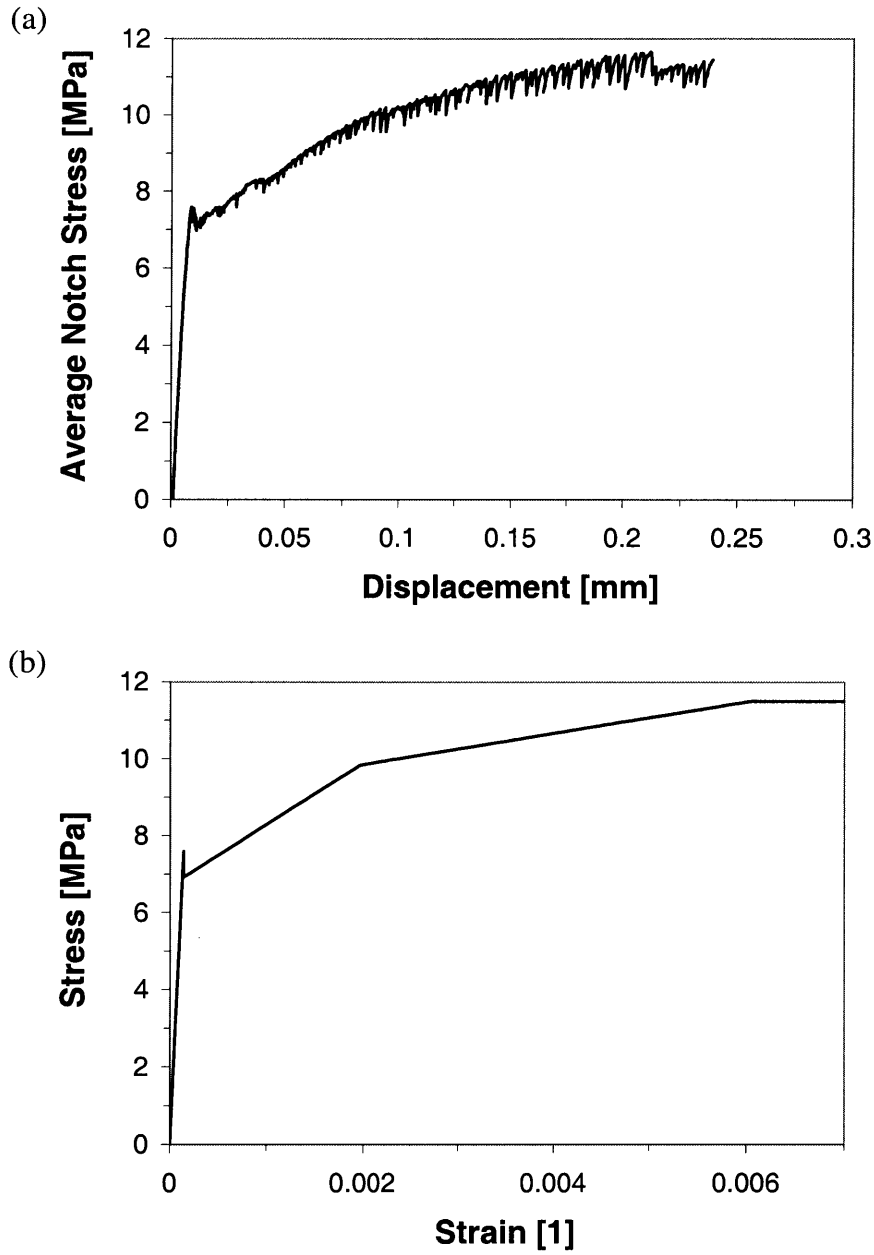

Figure 2-7: (a) Experimental notched tensile test data of DUCTAL^{TM} by Lafarge; (b) Stress-strain response of the 3-D UHPC model using input data of Table 2.1.

Chapter 3

UHPC MODEL VALIDATION

This second chapter on UHPC material modeling deals with model validation. The UHPC model of Chapter 2 was implemented in a commercial finite element program, CESAR-LCPC, which makes it possible to simulate the nonlinear response of UHPC structures [13]. To validate the UHPC model and its finite element implementation, two large-scale case studies are presented: a flexure test and a shear test of prestressed AASHTO Type II beam girders, which were recently carried out by the Federal Highway Administration (FHWA) at the Turner-Fairbank Highway Research Center Structures Laboratory in McLean, Virginia. The input parameters of the model-based simulations are the model parameters derived from a notched plate test of DUCTAL^{TM} (see Section 2.3), the UHPC material under investigation in this study provided by the UHPC manufacturer, Lafarge. The output of the simulations are global force-displacement and local strain predictions, which are compared with the experimental results obtained by FHWA. The objective of this chapter, therefore, is to validate on the basis of two independent data sets (input – output), the predictive capabilities of the model, model input parameters, and model implementation. Furthermore, for the two large-scale tests, we investigate the suitability of a crack opening design criterion recently issued by the French Association of Civil Engineering (AFGC) [38] to define the ultimate limit state of UHPC structures. Both model validation and crack opening design criterion are key elements of the model-based optimization methodology for UHPC structures developed in this work.

3.1 The FHWA UHPC Girder Tests

The validation data set considered here is derived from the flexure and the shear tests carried out by the Federal Highway Administration (FHWA) at the Turner-Fairbank Highway Research Center Structures Laboratory in McLean, Virginia under the direction of Joey Hartmann and Benjamin Graybeal [18,19]. Both of these tests were numerically simulated to gauge the accuracy and reliability of the UHPC model and its finite element implementation.

Both tests involved AASHTO Type II girders, depicted in Figure 3-1(a), comprised of the DUCTAL^{TM}, the UHPC material considered in this study. The AASHTO Type II prestressed concrete girder is a 91 cm (3 ft) high beam with a 30 cm (1 ft) wide top flange, 15 cm (6 in) wide web, and a 46 cm (1 ft 6 in) wide bottom flange. The AASHTO Type II girder is prestressed with 26 steel tendons, each 12.7 mm (0.5 in) in diameter, composed of low relaxation steel of strength $f_y^T = 1,860\,\text{MPa}$ (270 ksi) and stiffness $E_T = 200\,\text{GPa}$ (29,000 ksi) [18]. Each prestressing tendon was initially loaded to $\gamma = 55\%$ of its ultimate strength. Half of the tendons in the bottom flange were debonded for 91 cm (3 ft) from each end [18]. No shear reinforcement was used in either girder.

3.1.1 Validation Criteria

The finite element simulations validated the UHPC model with respect to three different criteria [13]:

- Load-deflection curves: The load-deflection curves of the FHWA specimen and the FE simulation demonstrate very good correlation and also prove the stability of the FE implementation with regard to the mesh density.

- Strain gauge measurements: The FE simulations provide results for the deflection of the nodes in a given mesh during loading. Strain results are calculated as the change in distance between two nodes divided by the original distance between the nodes. Strain predictions obtained from the FE simulation exhibit excellent agreement with strain measurements from strain gauges placed at various locations on the FHWA specimens.

- Cracking patterns: Plastic strains in the composite matrix can be related to cracking,

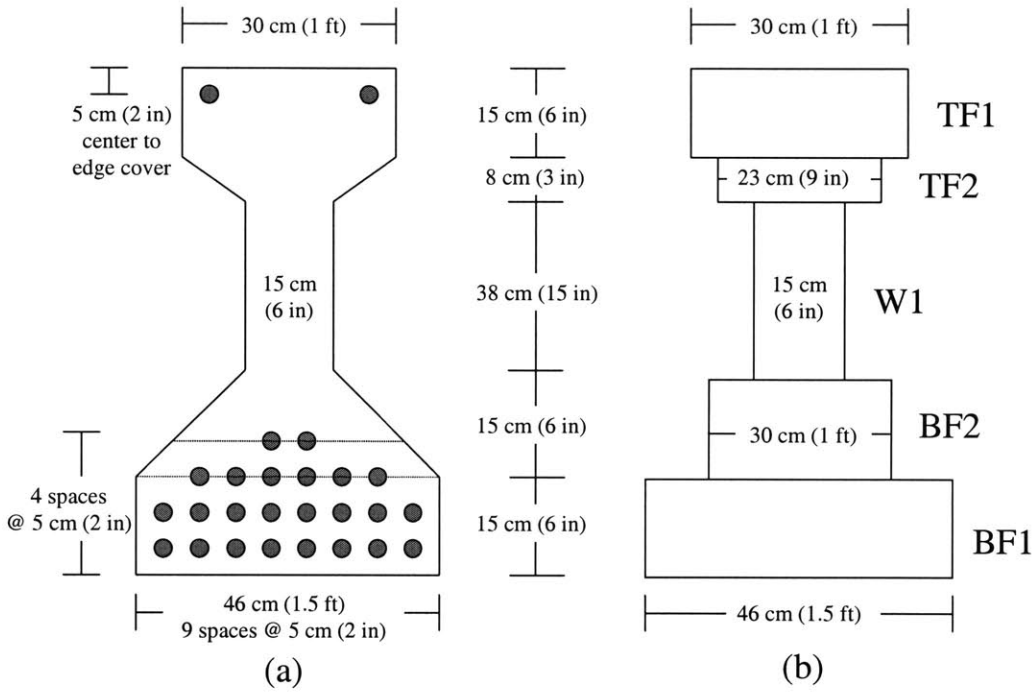

Figure 3-1: Cross section of the AASHTO Type II girder: (a) Actual beam; (b) Idealized 2-D model in finite element simulation.

which occurs in the cementitious matrix of UHPC. The composite matrix plastic strains as given by the FE simulation accurately model cracking observed in the FHWA specimens.

3.1.2 Modeling of Prestressing: Upper and Lower Bound

The prestressing tendons in the pre-tensioned beams are not explicitly simulated in the finite element model. Instead, the equivalent effect of the tendons is modeled, that is (1) the prestressing forces and (2) the contribution of the tendons to the stiffness and strength. This simplified modeling of prestressing will also be employed in the model-based optimization in subsequent chapters.

Equivalent Prestress Pressure

To capture the effect of prestressing forces, an equivalent external pressure is applied at the ends of the girder, representing the forces on the concrete element exerted after pre-tensioned prestress application. This pressure is expressed by:

$$p = \gamma f_y^T c_T \tag{3.1}$$

where γ is the prestress level, which in the case of the FHWA beams amounts to $\gamma = 0.55$; f_y^T is the strength of the prestressing tendons (here $f_y^T = 1,860\,\text{MPa}$ (270 ksi)). c_T is the (geometrical) reinforcement ratio of the prestressed concrete element:

$$c_T = \frac{A_{s,total}}{A_{c,element}} \tag{3.2}$$

where $A_{s,total} = \sum_{i=1}^{N} A_{s,i}$ the total cross sectional area of the N prestressing tendons, in the structural element of cross sectional area $A_{c,element}$. For the FHWA beam sections, we subdivide the bottom flange into two subregions (see Fig. 3-1(b)), denoted by BF1 and BF2, respectively. In BF1, $c_T = 3.0\%$, in BF2, $c_T = 2.2\%$. Analogously, in the top flange TF1, $c_T = 0.6\%$; $c_T = 0\%$ in the other cross sectional areas. Thus, the magnitude of p varies along the height of the girder according to the tendon reinforcement ratio c_T.

Effect of Prestressing Tendons on Composite Stiffness

A second effect of prestressing tendons on the structural behavior relates to the deformation of tendons in the section. In the case of a perfect adhesion of tendons and surrounding UHPC, the stiffness of the tendons contributes to the overall stiffness of the composite structural element, i.e. UHPC plus tendons. This is suitably captured by a mixture rule:

$$K^B \leq K_0 + c_T\,(E_T - K_0) \tag{3.3}$$

where $K_0 = C_M + C_F$ is the stiffness of the UHPC material (Section 2.1.1) and $E_T = 200\,\text{GPa}$ (29,000 ksi) is the Young's modulus of the tendons. The mixture rule (3.3), which is also known as the isostrain Voigt bound, represents an upper bound of the effective stiffness of the

overall composite, as it assumes the same strain field in the tendon-UHPC composite. In the simulations, this stiffness increase due to the tendons is enforced through the stiffness of the composite fiber phase in the structural element, i.e. the bottom flange, C_F^B, while the composite matrix stiffness is kept constant:

$$C_F^B = C_F + c_T\left(E_T - C_F\right) \tag{3.4}$$

where C_F is the composite fiber stiffness.

Effect of Prestressing Tendons on Composite Strength

Similarly, the presence of prestressing tendons has the potential to enhance the effective strength that the structural composite, UHPC plus tendons, realizes at failure. Indeed, from yield design theory [42], it can be shown that an upper strength bound Σ_y^B, based on the assumption of an identical strain rate field in tendons and UHPC at plastic failure, reads:

$$\Sigma_y^B \leq \Sigma_y + c_T[(1-\gamma)f_y^T - \Sigma_y] \tag{3.5}$$

where $\Sigma_y = k_M + f_y$ is the overall composite yield strength of the UHPC material (see Section 2.1.1), which is enhanced by the strength reserve of the tendons, $(1-\gamma)f_y^T$, available after prestressing to the prestress level γ. In the simulations, the upper strength bound (3.5) is applied to the yield strength of the composite fiber phase in the structural element, i.e. the bottom flange, f_y^B, while the composite matrix strength k_M is unchanged:

$$f_y^B = f_y + c_T[(1-\gamma)\sigma_T^u - f_y] \tag{3.6}$$

where f_y is the composite fiber yield strength of UHPC.

Upper and Lower Bound Input Model Parameters

The parameter values for the UHPC with a tendon effect ((3.4) and (3.6)) are provided in Table 3.1 ("UHPC with Tendons, BF1" and "UHPC with Tendons, BF2"). As shown in Table 3.1, the values for σ_{Fc} are also increased to ensure $\sigma_{Fc} > f_y$ and, as a consequence, $\alpha_F^{DP} \geq 0$, which

Model Parameter	UHPC Only		UHPC with Tendons, BF1		UHPC with Tendons, BF2	
	SI	IU	SI	IU	SI	IU
C_M [GPa /ksi]	53.9	7820	53.9	7820	53.9	7820
$C_F^{(B)}$ [GPa/ksi]	**0**	**0**	**6.0**	**870**	**4.4**	**640**
M [GPa/ksi]	1.65	240	1.65	240	1.65	240
ν [1]	0.17					
f_t [MPa/ksi]	0.7	0.1	0.7	0.1	0.7	0.1
k_M [MPa/ksi]	6.9	1	6.9	1	6.9	1
σ_{Mc} [MPa/ksi]	190	28	190	28	190	28
σ_{Mb} [MPa/ksi]	220	32	220	32	220	32
$f_y^{(B)}$ [MPa/ksi]	**4.6**	**0.67**	**29.6**	**4.29**	**22.9**	**3.32**
σ_{Fc} [MPa/ksi]	**10**	**1.5**	**30**	**4.4**	**30**	**4.4**

Table 3.1: Values of UHPC model parameters used in the FHWA flexure and shear finite element simulations. Bold characters denote change in material parameters.

is a requirement of the Drucker-Prager criterion (2.54) employed for the composite fiber phase. The new values of σ_{Fc} were chosen to be arbitrarily larger than f_y, but since no compressive yielding occurred in the bottom flange of the FHWA tests, the exact value of this parameter is irrelevant.

Finally, we should keep in mind that the mixture rules (3.4) and (3.6) are upper bounds of the effective stiffness and the effective strength of the UHPC-tendon composite, which overestimate stiffness and strength during loading and at failure. For this reason, we employ in the simulations two different sets of material parameters, a lower bound set and an upper bound set:

- The lower bound represents a "UHPC Only" structure. That is, the structural effect of the prestressing tendons was neglected except for the prestressing load p. This lower bound neglects any additional dissipative mechanisms related to tendon yielding, friction at the tendon-UHPC interface, etc.

- The upper bound represents the maximum possible effect of the prestressing tendons on the stiffness and strength of the bottom flange (Eqs. (3.4) and (3.6)). This upper bound overestimates the yielding capacity at failure as it neglects the possibility of bond failure as a kinematic failure mechanism.

3.1.3 Section Modeling and Load Application

In the finite element simulations, the AASHTO Type II girders are modeled in 2-D with solid plane stress finite elements. The FE meshes are comprised primarily of four-noded quadrilateral elements with some three-noded triangular elements. For each simulation, two types of meshes are examined, a coarse mesh and a fine mesh. To model the irregular girder cross section, the girder is partitioned along its height into five subdivisions of varying width as illustrated in Figure 3-1(b): the lower part of the bottom flange (BF1), the upper part of the bottom flange (BF2), the web (W1), the upper part of the top flange (TF1), and the lower part of the top flange (TF2). Each 2-D solid finite element was assigned a thickness according to its subdivision.

For both case studies, the prestressing pressures and gravity loads are simultaneously applied first. Then external loads are applied in 20 to 25 load steps, graduated such that smaller load steps are applied after the onset of plasticity (cracking). For this nonlinear material model, iterations are required at each load step to ensure convergence of the magnitude of the vector of residual forces to a tolerance of 0.01. For some load steps, convergence could not be achieved (e.g. load application greater than the capacity of the structure). Thus, the simulation was stopped when a given load step required more than 2000 iterations to converge.

3.2 Validation Set #1: FHWA Flexure Test

The FHWA flexure test is a four point bending test on an AASHTO Type II girder of 23.9 m (78.5 ft) loaded with two equal load points (total load F) located 0.9 m (3 ft) from the midspan. The loading configuration, beam geometry, and strain gauge location are illustrated in Figure 3-2. Figure 3-3 (a) displays the boundary conditions and load application locations; Figure 3-3 (b) shows the deformed shapes obtained by finite element simulation, and Figure 3-3 (c) the principal plastic strain in the composite matrix.

3.2.1 Global Results: Load-Deflections Curves

The load-deflection results from the FHWA experiment and the finite element simulation are graphed in Figure 3-4. Four different FE results are plotted in the figure: the upper bound

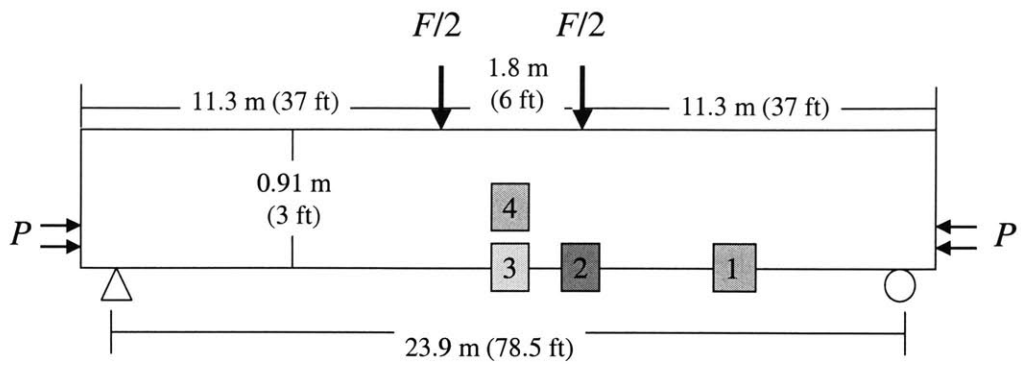

Figure 3-2: Loading configuration and strain gauge locations for the FHWA flexure test.

with a coarse and fine mesh (composed of 1005 and 2391 elements, respectively) and the lower bound with a coarse and fine mesh. The mesh stability of the FE simulations is verified as the coarse and fine mesh for each bound converge upon the same solution. As demonstrated, the simulated upper bound correlates very closely with the actual beam behavior. This is to be expected as the loading configuration induces high tensile stresses and flexure cracks in the bottom flange which activate significant stresses in the tendons.

The upper bound solution and the experimental result diverge at a load of $F = 800\,\text{kN}$ (180 kips), when the girder showed an abrupt load loss associated with the rupture of the tendons. This confirms the assumption of a tendon stiffness and strength effect as the stresses in the tendons are high enough to induce rupture. Since the FE model does not account for brittle rupture of the prestressing tendons, this abrupt load loss does not appear in the FE simulation, which achieves a much higher ultimate strength. However, despite its inability to directly predict the ultimate strength and subsequent collapse, the upper bound provides a very good load-deflection prediction before structural failure.

3.2.2 Local Results: Strain Gauge Measurements

Figure 3-5 compares the strain measurements given by strain gauges placed on the actual beam (oriented longitudinally, see Fig. 3-2) and strain measurements given by the upper bound finite element result (which was shown to give a very good load-deflection prediction in Figure 3-

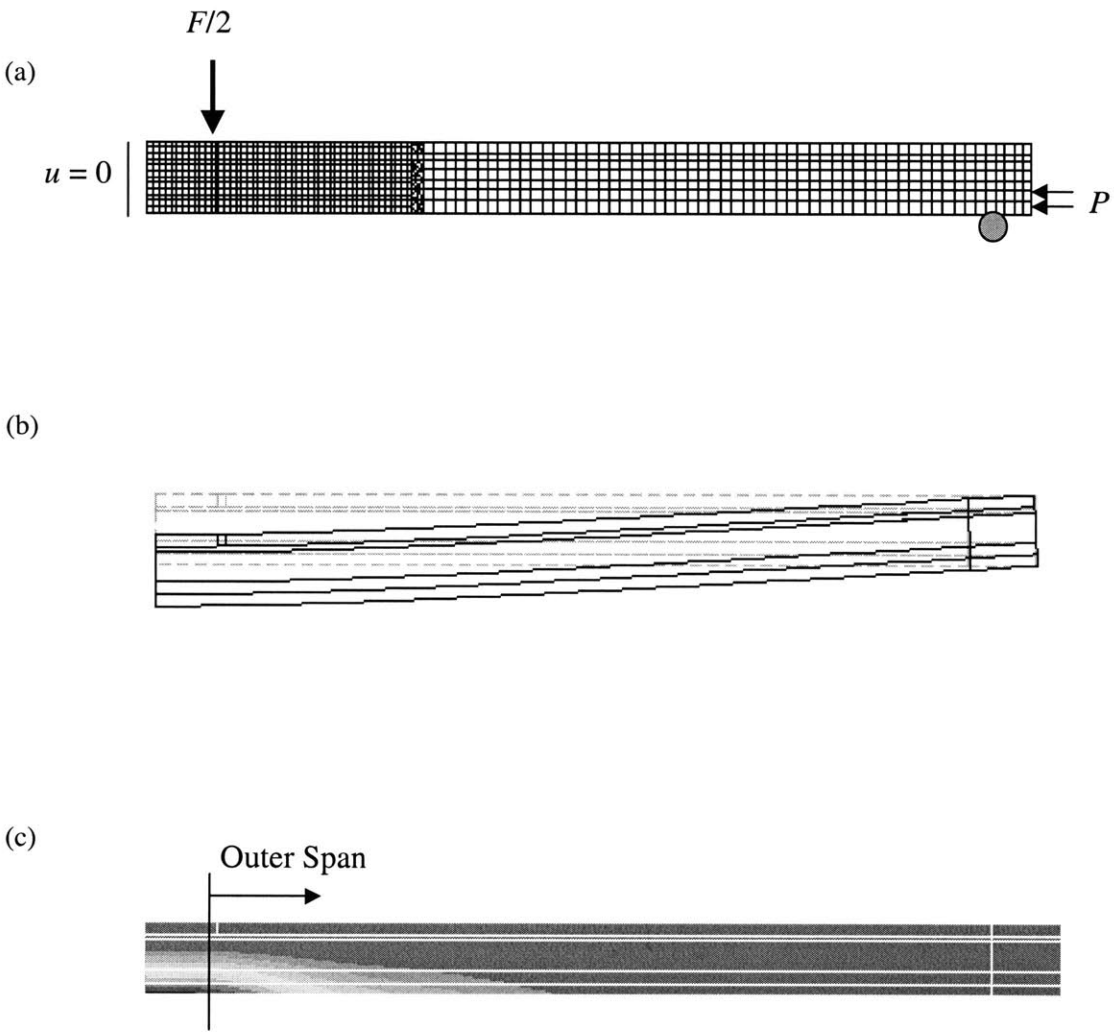

Figure 3-3: Model-based simulation results of FHWA flexure test: (a) Fine mesh with boundary conditions; (b) Deformed shape; (c) Composite matrix plastic strains.

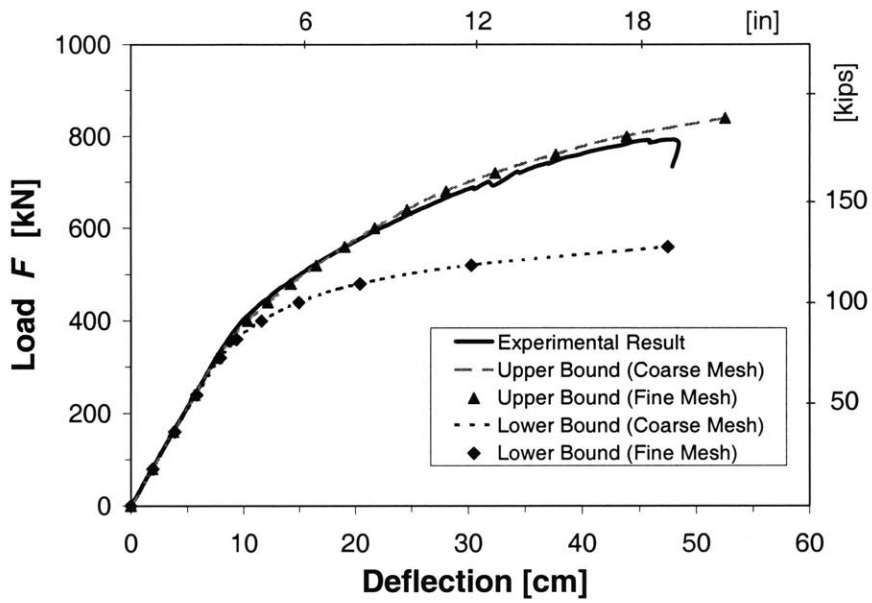

Figure 3-4: FHWA flexure test: Global force-midspan deflection curve.

4). Both the FE and actual strain measurements are plotted to the load at which the actual strain measurements exhibit discontinuity due to local cracking. As shown, the finite element simulation is also able to reproduce local strain results thus confirming the relevance of the upper bound data set (see Table 3.1) for predicting the structural behavior both locally and globally.

3.2.3 Local Results: Cracking Patterns

The composite matrix plastic strain results, $\varepsilon^p_{M,I}$, displayed in Figure 3-3 (c) for a very high load, can be translated into cracking data. Figure 3-6 displays the cracking evolution (as longitudinal composite matrix plastic strains $\varepsilon^p_{M,xx}$) along the girder height at the midpoint of the center span as predicted by the upper bound fine mesh simulation. Figure 3-7 displays the corresponding longitudinal stress profiles in the section. At the onset of noticeable nonlinear behavior $F = 400\,\text{kN}$ (90 kips) (see Fig. 3-3), the composite matrix plastic strains already extend up to a height of 27 cm (11 in), almost completely through the bottom flange. At a load

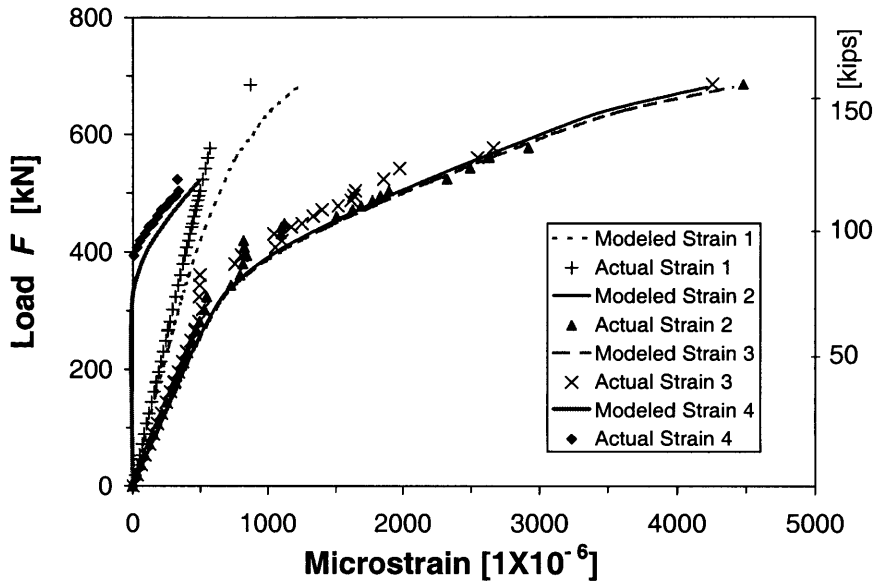

Figure 3-5: FHWA flexure test: Local strain gauge measurements.

$F = 600\,\text{kN}$ (135 kips), the height of the crack is $h_{cr} = 47\,\text{cm}$ (19 in) (roughly halfway up the web). At a load $F = 800\,\text{kN}$ (180 kips), the height of the crack is $h_{cr} = 62\,\text{cm}$ (24 in) (almost to the top of the web); and some plasticity has occurred in the top flange which can be associated with compressive crushing.

The stress profiles displayed in Figure 3-7 complement these results as the curves exhibit inflections at the crack heights (i.e. $h_{cr} = 27$, 47, 62 cm (11, 19, 24 in) for $F = 400$, 600, 800 kN (90, 135, 180 kips), respectively). These inflections represent the initiation points of the post-cracking stress-strain behavior. The curves in Figure 3-7 also delineate some UHPC stress limits, as numbered on the $F = 800\,\text{kN}$ (180 kips) result. Point 1 correlates with the first cracking strength of the UHPC in the web, $\Sigma_0^- = f_t + k_M = 7.6$ MPa (1.1 ksi). The stresses between point 2 and point 3 are associated with the stresses in BF2 which approach, but do not reach, their composite yield strength $\Sigma_y^{BF2} = f_y^{BF2} + k_M = 29.8\,\text{MPa}$ (4.3 ksi). The stresses in BF1 are delimited by points 3 and 4. At the bottom of the girder, point 4, the longitudinal stress is equivalent to the BF2 composite yield strength $\Sigma_y^{BF1} = f_y^{BF1} + k_M = 36.5\,\text{MPa}$ (5.3 ksi) (see Table 3.1). It appears that attainment of the composite yield strength in BF2 coincides

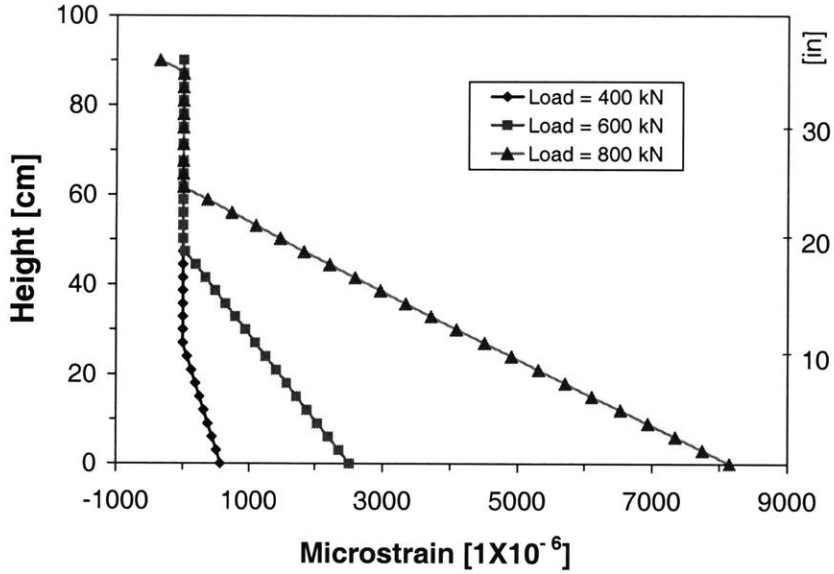

Figure 3-6: Evolution of longitudinal composite matrix plastic strains $\varepsilon^{p}_{M,xx}$ along the height of the FHWA flexure girder at the midpoint as predicted by the upper bound fine mesh simulation.

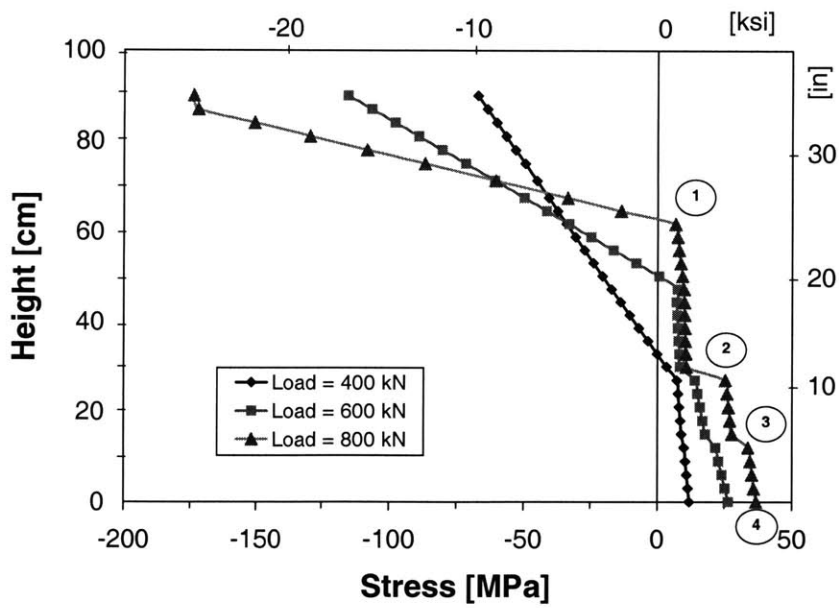

Figure 3-7: Evolution of longitudinal stresses $\Sigma_{xx} = \sigma_{M,xx} + \sigma_{F,xx}$ along the height of the FHWA flexure girder at the midpoint as predicted by the upper bound fine mesh simulation.

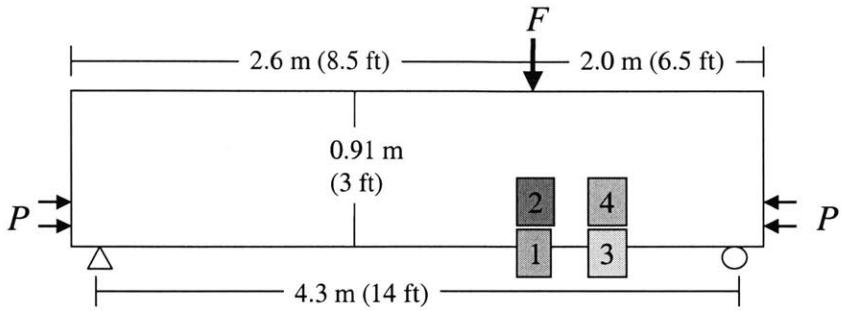

Figure 3-8: Loading configuration and strain gauge locations for the FHWA shear test.

with tendon failure in the flexure girder at a load $F_u = 800\,\text{kN}$ (180 kips) (see Fig. 3-3). In other words, evidently, one may be able to directly associate the ultimate state of this structure to ultimate strength of the bottom flange Σ_y^B and, by association, the tendon stresses $\sigma_T = f_y^T$. This is only possible, however, if the tendons do not exhibit significant plastic yielding before rupture in tension.

3.3 Validation Set #2: FHWA Shear Test

The FHWA shear test is a three point bending test on a 4.3 m (14 ft) long AASHTO Type II girder. The load F is applied off-center, 1.8 m (6 ft) from one of the supports, which induces high shear stresses in the short load span. Figure 3-8 displays the loading configuration and strain gauge locations. The model-based simulations were carried out with a coarse mesh (720 elements) and a fine mesh (2878 elements); the latter is displayed in Figure 3-9 (a) along with the applied boundary conditions and loads. The deformed shape for the fine mesh is drawn in Figure 3-9 (b), and Figure 3-9 (c) displays the composite matrix plastic strains.

3.3.1 Global Results: Load-Deflections Curves

The load-deflection results from the shear experiment and the FE results are plotted in Figure 3-10. The experimental curve was adjusted to account for the experimental compliance in the supports determined by Benjamin Graybeal [20]. Four different FE results are presented in

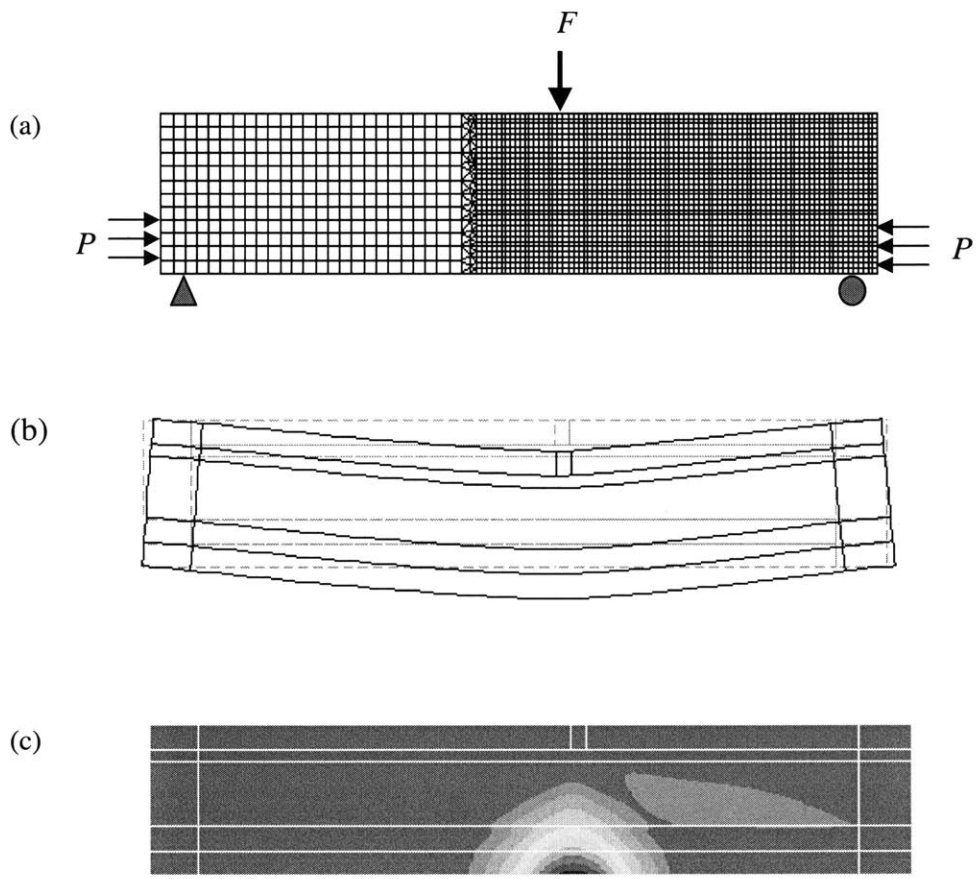

Figure 3-9: Model-based simulation results of FHWA shear test: (a) Fine mesh with boundary conditions; (b) Deformed shape; (c) Composite matrix plastic strains.

Figure 3-10 which verify the FE mesh stability: a coarse and fine mesh for the lower bound ("UHPC Only") and a coarse and a fine mesh for the upper bound (tendon strength and stiffness added to the bottom flange, according to relations (3.4) and (3.6)). In contrast to the flexural test, the lower bound here closely matches with the actual load-deflection behavior. This suggests an insignificant activation of stresses in the prestressing tendons. This supposition was substantiated by the large shear cracks which appeared in the web during pre-peak loading. Thus, it can be interpreted that the nonlinear structural behavior is mainly governed by shear cracking in the (unreinforced) web.

The FE upper bound prediction and the experimental result diverge at a load $F = 3,400\,\text{kN}$ (765 kips) when the FHWA shear beam exhibited structural failure. Nonetheless, the FE lower bound solution appears to approach this same maximum load. It is suggested that this structural failure was a result of bond failure between the tendons and the UHPC in the bottom flange. In support of this bond failure premise is the severe tendon slip that was recorded during the test just prior to a deflection of 15 mm (0.6 in), when the girder manifests an abrupt drop in load capacity. Accordingly, the lower bound result manages to predict the shear behavior accurately since a tendon effect never fully develops due to tendon slip. Furthermore, since the beam acted as a "UHPC Only" structure, the lower bound also seems to ably predict the ultimate load capacity of the beam. The bond failure is most likely a consequence of short anchorage lengths (only 2 m (6.5 ft) on the short load span side) which do not permit proper tendon-UHPC bonding.

3.3.2 Local Results: Strain Gauge Measurements

Strain measurements given by strain gauges on the FHWA beam and the lower bound FE simulations are plotted in Figure 3-11 for the strain gauges depicted in Figure 3-8. The predicted local strain measurements exhibit very good correlation with the actual local strain readings, thus confirming the relevance of the lower bound solution for simulation of both the local and global response of the FHWA shear girder.

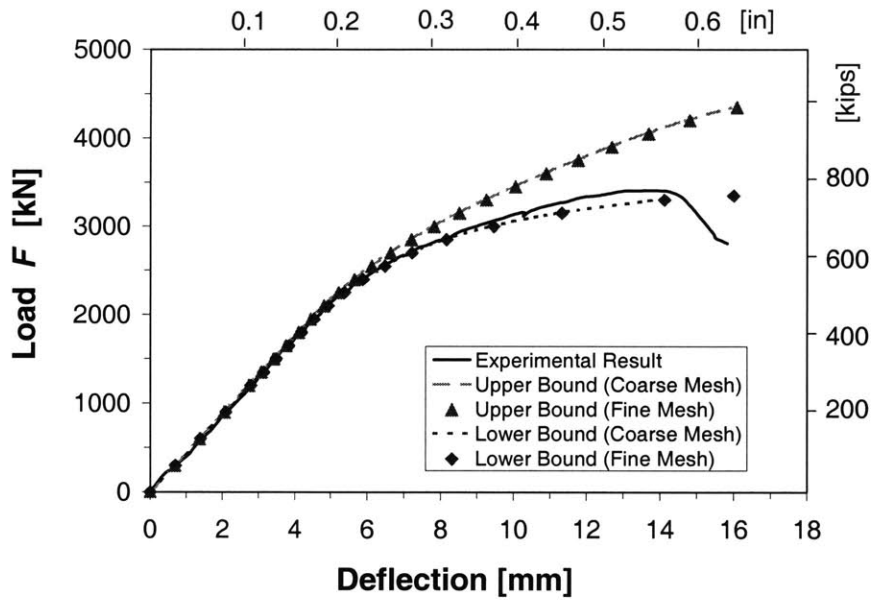

Figure 3-10: FHWA shear test: Global force-midspan deflection curve.

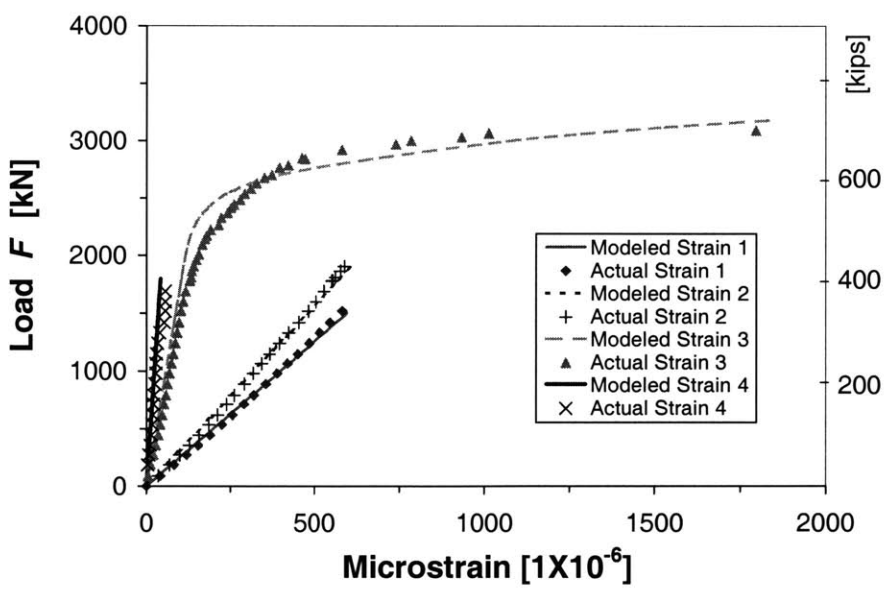

Figure 3-11: FHWA shear test: Local strain gauge measurements.

3.3.3 Local Results: Cracking Patterns

The principal composite matrix plastic strains $\varepsilon^{p}_{M,I}$ for the FHWA shear beam as predicted by the lower bound FE simulations are illustrated in Figure 3-9 (c). As shown in the figure, there is substantial flexural cracking in the bottom flange under the load point, which was detected in the FHWA shear beam. However, focusing on the short load span, significant shear cracking is also evident. Figure 3-12 (a) and (b) represent magnitude and orientation of the composite matrix plastic strains (or shear crack opening displacement) in the web. As physically observed, first shear cracking is predicted at the web-flange interface. Furthermore, the fully developed plastic strain vectors suggest the orientation of crack propagation, which is perpendicular to the orientation of the crack openings (crack propagation denoted in Fig. 3-12 (b) with dashed line). The shear cracking angle $\alpha_{cr} \approx 35°$ predicted by the FE simulation also corresponds well to that of the large shear crack pictured in Figure 3-12 (c).

3.3.4 Discussion of UHPC Model Validation

The FE simulation results for both the flexural and the shear test show the remarkable capacity of the model (and its model implementation) to accurately predict the *in situ* behavior of the UHPC material, which translates into an accurate prediction of the structural behavior of UHPC elements. The validation of the UHPC model is based on two independent data sets, one employed for the determination of the input parameters (calibration) and the second for testing of the model at a structural scale in bending and shear. In this sense, the case studies presented here validate not only the model and the model implementation, but also the large-scale relevance of the model input parameter values, which were determined from the UHPC notched plate test. That is, the harsh loading conditions imposed by the notched tension testing configuration appear to effectively capture the material performance of UHPC in large scale applications. This was validated with respect to three different aspects: load-deflection behavior, local strain measurements, and cracking patterns. In particular, the FE implementation is able to predict the strain behavior and cracking patterns quite adeptly. This is possible due to the continuous post-cracking behavior of UHPC at the material level (i.e. small, evenly spaced, highly distributed cracks). The FE local strain predictions would not be as successful for a material which exhibits softening behavior or local failure (i.e. localized

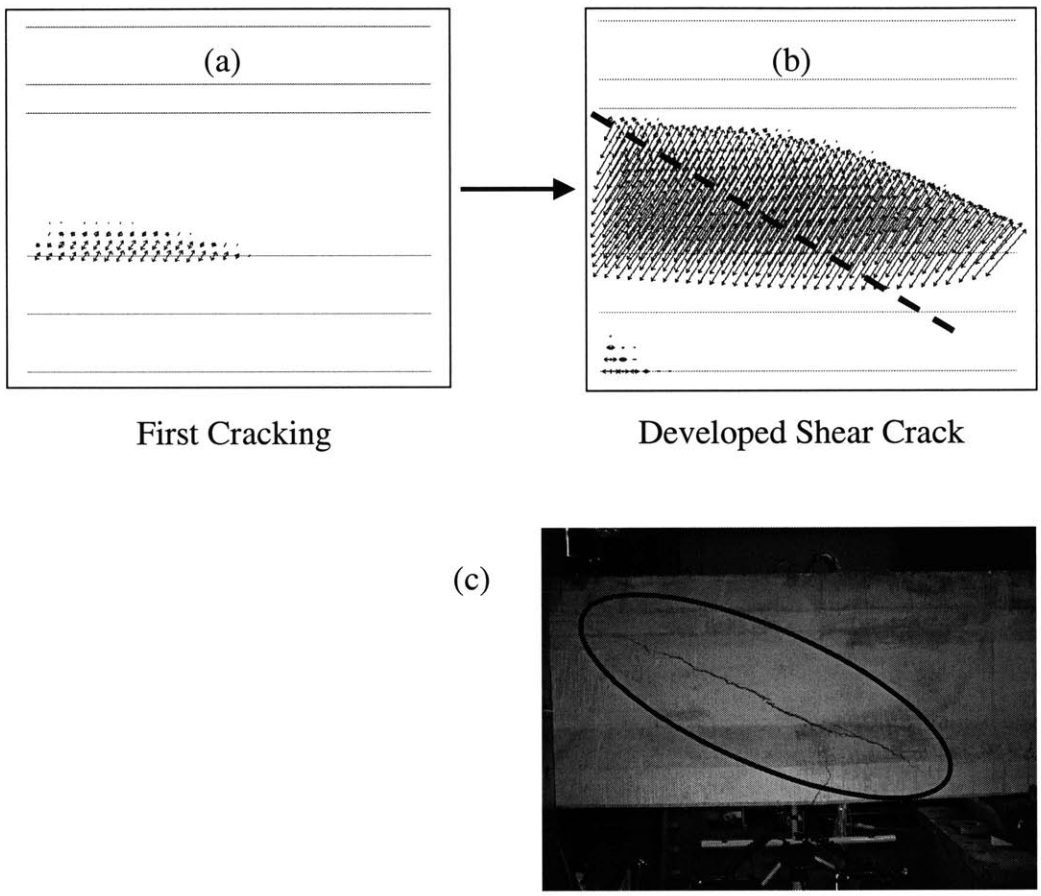

Figure 3-12: Model-based simulation results of composite matrix cracking: (a) Crack initiation at the flange-web interface; (b) Fully developed shear cracks in the web; (c) Experimental crack patterns at failure of the shear beam.

cracks), such as a less ductile FRCC. As a result, the simulation results underscore the high *in situ* ductility of the UHPC material which is captured by the UHPC model.

For the flexure test, the overall response in bending is governed by the flange response of UHPC reinforced by prestressing tendons, which deform together as a composite until tendon failure at very large deflections of the beam ($\delta/L \approx 1/50$). While the upper bound parameter set offers a simple, yet effective way to model the tendon effect in the FHWA flexure test, the load bearing capacity of the structure in bending is ultimately governed by the tendon strength. Similarly, utilizing a lower bound material set to simulate the FHWA shear test proves to be appropriate as tendon slip in the girder compromises the tendon effect. For both FHWA specimens, structural failure was tendon-related: tendon rupture in the flexure test and tendon-bond failure in the shear test, which is beyond the scope of the model and its current predictive capabilities.

3.4 Design Load Prediction

One advantage of the two-phase structure of the UHPC model is its ability to assess the matrix plastic strains which represent crack opening at a macroscopic scale. Since the model does not account for a softening behavior, which goes beyond the safe design considerations, it is sensible to introduce a maximum crack opening criterion for the proper functioning of the UHPC material. Such a criterion has been recently proposed in the UHPC design guidelines issued by the French Association of Civil Engineering (AFGC) [38][1]:

$$\max\left[[w]\right] \ll \left\{ \begin{array}{l} [[w]]^{un}_{\text{lim}} = 0.3\,\text{mm}\left(= \dfrac{1}{85}\,\text{in}\right) \text{ for unreinforced sections} \\ [[w]]^{re}_{\text{lim}} = \min\left(\dfrac{L_f}{4}; \dfrac{h}{100}\right) \text{ for reinforced sections} \end{array} \right\} \tag{3.7}$$

where $[[w]]_{\text{lim}}$ is a maximum admissible crack opening which differs for unreinforced and reinforced UHPC sections, which depends on the fiber length L_f of the UHPC and the height h of the structure. For UHPC, the values for $[[w]]_{\text{lim}}$ do not represent the crack opening of an individual crack, but rather the total cumulative crack opening measured over a characteris-

[1]This design crietrion will be discussed in greater detail in Chapter 4.

tic length $l_c = \frac{2}{3}h$. This consideration allows us to translate the dimensional crack opening criterion into a dimensionless maximum matrix plastic strain criterion:

$$\max_{\underline{x}} \left(\varepsilon^p_{M,I}(\underline{x})\right) \leq \frac{[[w]]_{\text{lim}}}{l_c} = \left\{ \begin{array}{l} \varepsilon^{p,un}_{\text{lim}} = 1.5\frac{[[w]]^{un}_{\text{lim}}}{h} \text{ for unreinforced sections} \\ \varepsilon^{p,re}_{\text{lim}} = \min\left(\frac{3L_f}{8h}; \frac{3}{200}\right) \text{ for reinforced sections} \end{array} \right\} \tag{3.8}$$

where $\max_{\underline{x}} \left(\varepsilon^p_{M,I}(\underline{x})\right)$ represents the maximum value of the plastic strain in the composite matrix.

It is instructive to employ the dimensionless crack opening criterion for the FHWA flexure and shear test, for which (3.8) reads ($L_f = 13\,\text{mm}\,(= \frac{1}{2}\,\text{in})$, $h = 0.91\,\text{m}\,(= 3\,\text{ft})$):

$$\max_{\underline{x}} \left(\varepsilon^p_{M,I}(\underline{x})\right) \leq \left\{ \begin{array}{l} \varepsilon^{p,un}_{\text{lim}} = 4.9 \times 10^{-4} \text{ for unreinforced sections} \\ \varepsilon^{p,re}_{\text{lim}} = 5.4 \times 10^{-3} \text{ for reinforced sections} \end{array} \right\} \tag{3.9}$$

Figure 3-13 (a) displays the normalized load versus the normalized plastic strain for the upper bound of the FHWA flexural beam. The load F is normalized by the experimental failure load, $F_u = 800\,\text{kN}$ (180 kips). The maximum plastic strain, which occurs in the reinforced flange (see Fig. 3-6), is normalized by $\varepsilon^{p,re}_{\text{lim}}$ given in (3.9). From this figure, we determine the flexural load bearing capacity allowed by the UHPC design criterion:

$$\frac{\max_{\underline{x}} \left(\varepsilon^p_{M,I}(\underline{x})\right)}{\varepsilon^{p,re}_{\text{lim}}} = 1 \Rightarrow \frac{F_{\text{lim}}}{F_u} = 0.90 \tag{3.10}$$

The normalized load-plastic strain curve for the FHWA shear beam is given in Figure 3-13 (b), in which the load is normalized by the experimental failure load $F_u = 3,400\,\text{kN}$ (765 kips), while the maximum plastic strain in the unreinforced web, which governs the overall shear behavior, is normalized by the limit value $\varepsilon^{p,un}_{\text{lim}}$ given in (3.9). The shear load bearing capacity allowed by the UHPC design criterion is:

$$\frac{\max_{\underline{x}} \left(\varepsilon^p_{M,I}(\underline{x})\right)}{\varepsilon^{p,un}_{\text{lim}}} = 1 \Rightarrow \frac{F_{\text{lim}}}{F_u} = 0.86 \tag{3.11}$$

We note that the crack opening design criterion provides for both cases, flexure and shear,

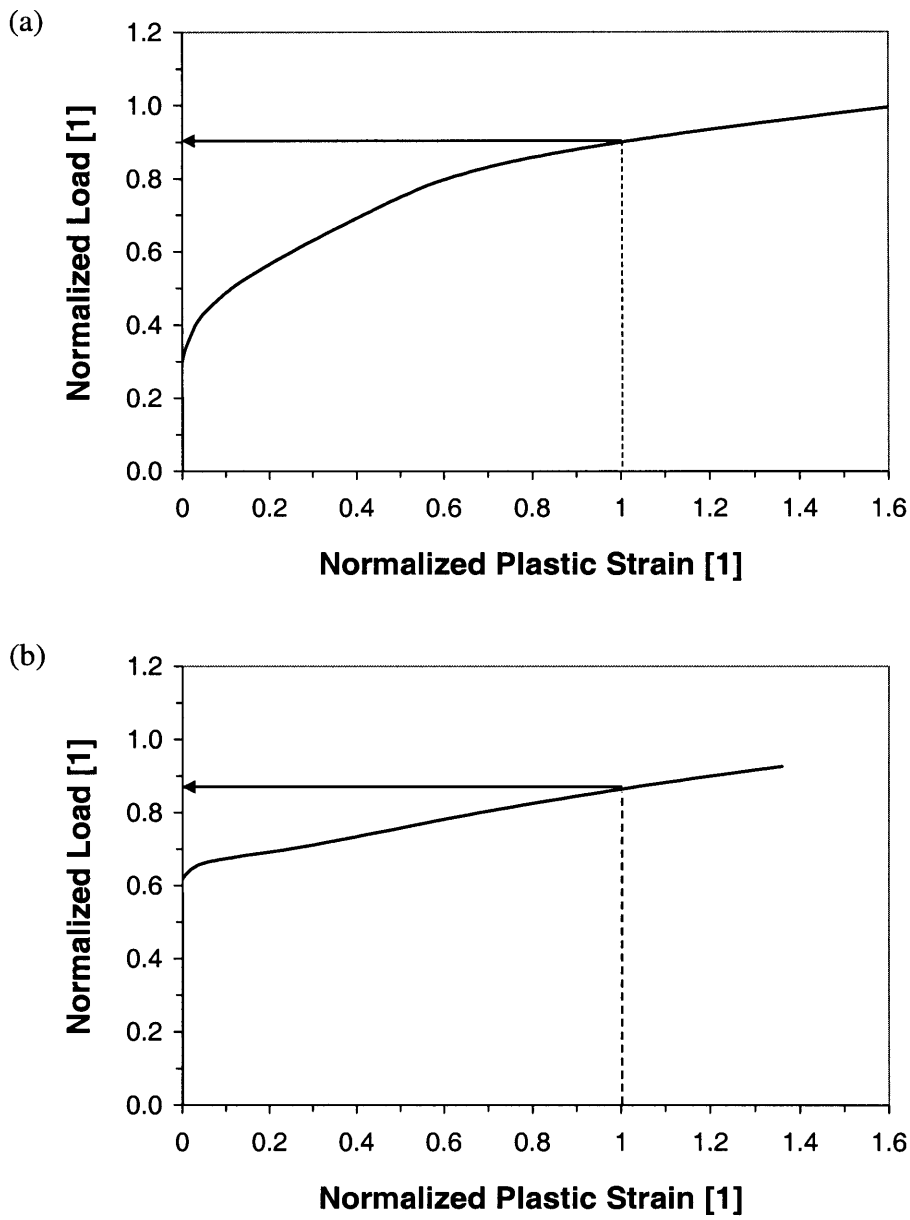

Figure 3-13: Normalized load F/F_u versus normalized plastic strain for: (a) FHWA flexure test ($F_u = 800\,\text{kN}$ (180 kips)); (b) FHWA shear test ($F_u = 3,400\,\text{kN}$ (765 kips)).

a safe allowable capacity F_{lim} compared to the actual load bearing capacity F_u of the structure, which we recall was tendon dependent. In other words, a restriction of the crack width of UHPC, simultaneously limits the deformability of the structure. This prevents excessive strains in the tendons, which may lead to tendon rupture (as in the FHWA flexure test), and may prevent unsafe strain differentials between the tendon and the UHPC which induce tendon slip (as in the FHWA shear test).

3.5 Summary of Model and Model Validation

The main findings of the first part of this report relate to the suitability of the two-phase constitutive model for UHPC, which will be employed for model-based optimization in subsequent chapters. These are:

- The employment of UHPC for structural applications is possible because of the capacity of the material to carry tensile loads after crack opening. UHPC, in contrast to normal concrete materials, exhibit small standard deviation in tensile properties, which makes it possible to safely utilize for this tensile behavior in structural applications. The *in situ* tensile behavior of the material in large-scale structural applications is best captured by a notched tension test, which can be viewed as a characteristic curve for a specific UHPC material, here DUCTAL^{TM}. Such a single notched tension test is capable of providing all the necessary tensile material parameters to execute an accurate large scale simulation.

- The finite element implementation of the UHPC model exhibited a clear capacity to simulate the behavior of large scale UHPC structures, as exemplified by the two large scale case studies presented in this chapter. Not only is the finite element simulation able to reproduce global effects, such as the load-deflection behavior of girders, but also local effects, such as strains at various locations on the girder.

- The key variable for the description of the ductile behavior of UHPC structures is the crack opening, which occurs in the cementitious matrix of UHPC. The two-phase material model accounts for this crack opening by distinguishing in the overall composite response the irreversible deformation in the matrix and fiber phase; thus providing a rational

means of realistically predicting cracking patterns and crack width densities in terms of composite matrix plastic strains.

- A suitable design criterion for large-scale structural applications is a criterion which restricts the maximum crack width to values that limit the deformability of structural components. Such a criterion prevents the occurrence of excessive deformation in UHPC and structural components that may trigger localized fracture or rupture. The values for maximum admissible crack widths from the AFGC guidelines appear to provide safe limits for the load bearing capacity of UHPC structures.

Part II

MODEL-BASED OPTIMIZATION

Chapter 4

UHPC SECTION DESIGN FORMULA, DESIGN CRITERIA AND DESIGN STRATEGY

The second part of this report is devoted to the development and implementation of a methodology for model-based optimization of UHPC highway bridge girders for the U.S. market. To motivate the following developments, this chapter begins with a simple section design scheme, a two-point section model based on section equilibrium and the 1-D UHPC model presented in Section 2.1. This section design scheme incorporates, in compact form, all the elements of an elaborate optimization procedure, design parameters, and design criteria. This design formula will also allow us to highlight the difference between normal concrete section design and UHPC section design. Then, by generalizing this simple design formula, we will identify pertinent design parameters and design criteria that will be employed in the next chapter for model-based optimization. By way of application, we illustrate the 1-D section modeling procedure, and determine primary section dimensions for single span bridge girders.

4.1 1-D Section Design Formula

In these optimizations, we focus on sections made of UHPC subjected to external loading. For highway bridge girders, these sections come in a variety of forms, ranging from $\mathcal{I}$-sections to

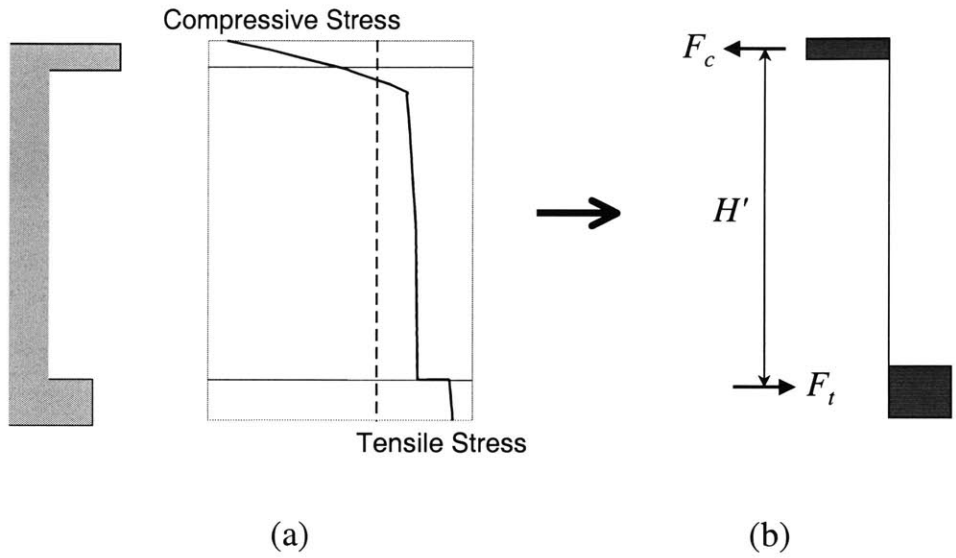

Figure 4-1: The two-point engineering section design model: (a) Realistic stress Distribution of a UHPC Section in bending; (b) Simplified design model.

π-sections, and more elaborated shapes as discussed in more detail later on. As far as the flexural load bearing capacity is concerned, the section performance in a very first approach can be approximated by a two point section model, sketched in Figure 4-1, in which the upper section represents the upper flange or deck, and the lower section the bottom flange, which accommodates prestressing tendons. As discussed in Section 3.2, this bottom flange governs the flexure behavior, that is the section moment load bearing capacity. For a UHPC section, subjected to a pure flexural loading, the maximum admissible moment of the two-point section model can be approximated by:

$$M_u \leq \max M = (\Sigma_y^B A_f) \times H' \tag{4.1}$$

where M_u is the design moment; $\Sigma_y^B = k_M + f_y^B$ is the effective tensile strength of the bottom flange of section A_f, and H' is the effective distance between the bottom and upper flange. Expression (4.1) is based on the assumption that the compressive deck, because of the high compressive strength of UHPC, is in an elastic state, while the UHPC bottom flange composite

composed of UHPC reinforced by prestressing tendons, is entirely at yield in tension[1]. This requires, for UHPC, to check the proper functioning of the fiber reinforced composite material via a maximum crack opening criterion of the form (3.8):

$$\max_{\underline{x}} \left(\varepsilon^{p}_{M,I} \left(\underline{x} \right) \right) \leq \varepsilon^{p,re}_{\lim} = \min \left(\frac{3L_f}{8H'}; \frac{3}{200} \right) \tag{4.2}$$

where $\varepsilon^{p,re}_{\lim}$ refers to the maximum admissible plastic strain in the composite matrix in a reinforced UHPC-section; here the bottom flange, while $\varepsilon^{p}_{M,I}\left(\underline{x}\right)$ stands for the plastic strain realized locally (at a point located by position vector $\underline{x}$) in the structure. The stress associated with this maximum plastic strain $\Sigma^{B}_{\lim} = \Sigma(\varepsilon^{p,re}_{\lim})$ may well be smaller than the effective yield strength Σ^{B}_{y} of the composite, and the moment capacity of the two-point section is reduced by a factor $f = \Sigma^{B}_{\lim}/\Sigma^{B}_{y} \leq 1$:

$$M_u \leq \max M = f \times (\Sigma^{B}_{y} A_f) \times H' \tag{4.3}$$

The design moment M_u is the sum of two terms: the moment M_u^{load} related to force application (dead weight, traffic load, etc.) and one related to prestress application, which can be approximated by $M_p = -pA_fH'$, where p is the effective prestress pressure of the bottom flange defined by (3.1); thus:

$$M_u = M_u^{load} - pA_fH' \leq f\Sigma^{B}_{y} A_f H' \tag{4.4}$$

or equivalently, in a dimensionless form:

$$\frac{M_u^{load}}{(\Sigma^{B}_{y} A_f)H'} \leq f + \bar{p} \tag{4.5}$$

where $\bar{p}$ is the dimensionless parameter representing the ratio of prestress pressure p to effective composite yield strength Σ^{B}_{y}. Despite its simplicity, relation (4.5), provides interesting insight into the design requirements for prestressed UHPC sections:

- As in classical reinforced concrete design, relation (4.5) limits the bending moment M_u^{load}

[1]The simplified section model neglects the contribution of the web to the overall section moment capacity.

induced by load application to a maximum value. In contrast to concrete design, this maximum value relates to the effective composite strength of the bottom flange, Σ_y^B, defined by the upper bound estimate (3.5), which we recall:

$$\Sigma_y^B \equiv \Sigma_y + c_T[(1-\gamma)f_y^T - \Sigma_y] \tag{3.5}$$

where $\Sigma_y = k_M + f_y$ is the overall composite yield strength of the UHPC material (see Section 2.1.1), which is enhanced by the strength reserve of the tendons $(1-\gamma)f_y^T$, available after prestressing to the initial prestress level γf_y^T is the strength of the tendon. c_T is the (geometrical) reinforcement ratio of the prestressed bottom flange.

- As in classical prestressed concrete design, the presence of prestressing enhances the maximum moment capacity, which is captured in (4.5) by the dimensionless quantity:

$$\bar{p} = \frac{p}{\Sigma_y^B} = c_T \frac{\gamma f_y^T}{\Sigma_y^B} \tag{4.6}$$

- In contrast to reinforced and prestressed concrete design is the presence of a factor f, which restricts the maximum crack opening:

$$f = \min\left(\frac{\Sigma_{\text{lim}}^B}{\Sigma_y^B}, 1\right) \tag{4.7}$$

The stress $\Sigma_{\text{lim}}^B = \Sigma\left(\varepsilon_{\text{lim}}^{p,re}\right)$ can be deduced from the 1-D state equations (2.2) by letting $\varepsilon_M^p = \varepsilon_{\text{lim}}^{p,re}$ and $\varepsilon_F^p = 0$, and noting that $\sigma_M = k_M$. This yields:

$$\Sigma_{\text{lim}}^B = \left[C_F^B + M\left(1 + \frac{C_F^B}{C_M}\right)\right]\varepsilon_{\text{lim}}^{p,re} + \left(1 + \frac{C_F^B}{C_M}\right)k_M \tag{4.8}$$

where C_F^B is the effective composite fiber stiffness defined by (3.4),

$$C_F^B \equiv C_F + c_T\left(E_T - C_F\right) \tag{3.4}$$

All parameters (C_M, C_F, M, k_M) are known UHPC material parameters (see Table 2.1).

Eq. (4.5) together with (3.4), (3.5), (4.2) and (4.6) to (4.8) are readily employed, in a first-

order engineering approach, as design formula for prestressed UHPC girder sections, idealized by the two-point section model. In contrast to reinforced and prestressed concrete design formulas, the proposed simplified UHPC section model accounts for the tensile strength contribution of the UHPC material through relation (3.5) and the maximum crack opening criterion (4.2).[2]

By way of example, we consider the FHWA flexural test from Section 3.2. From Figure 3-1, we determine for the bottom flange section (BF1+BF2): $A_f = 0.116\,\mathrm{m}^2$ ($180\,\mathrm{in}^2$), $c_T = 2.7\%$, $H' = 0.67\,\mathrm{m}$ (26 in), and $p = 27\,\mathrm{MPa}$ (3.9 ksi) (from (3.1)). Furthermore, with the characteristic UHPC values of Table 2.1, $\Sigma_y^B = 34.2\,\mathrm{MPa}$ (5.0 ksi) (from (3.5)), $C_F^B = 5.4\,\mathrm{GPa}$ (780 ksi) (from (3.4)), and $\Sigma_{\mathrm{lim}}^B = 47\,\mathrm{MPa}$ (6.8 ksi) (from (4.8) with $\varepsilon_{\mathrm{lim}}^{p,re} = 5.4 \times 10^{-3}$ from (3.9)). Relations (4.6) and (4.7) deliver $f = 1$, $\bar{p} = 0.8$, and finally the maximum bending moment $M_u^{load} \leq 4.75\,\mathrm{MN\,m}$ (3,500 kips ft) predicted by the design formula. This prediction comes very close to the actual ultimate limit moment ($4.8\,\mathrm{MN\,m}$ (3,550 kips ft)) of the FHWA beam due to dead weight and the four-point bending configuration.

4.2 Model-Based Design Strategy

The simple section design model developed above has all the elements of a more general design strategy for UHPC section models. These are:

1. Design parameters, which comprises geometrical parameters (e.g. bottom flange section A_f, height H'), material parameters (i.e. UHPC material properties and tendon properties), and load parameters (for instance bending moment M_u^{load}).

2. Design Criteria: Besides equilibrium conditions (e.g. section equilibrium), UHPC design requires a crack opening criterion, and this for both the service state and the ultimate strength limit state.

A combination of design parameters and design criteria allows one to define an optimization procedure.

[2] To apply the model to reinforced/prestressed concrete sections, it suffices to set $\Sigma_y = 0$ in (3.5), let $f = 0$ in (4.5), and add an appropriate strength design criterion for the compressive flange.

4.2.1 LRFD Design versus UHPC Design Criteria

The design strategy we employ here is adopted from the concept of AASHTO Load Resistance Factor Design (LRFD) [6]. The performance of a structure is evaluated for two limit states, the service limit state (SLS) and the ultimate strength limit state (ULS). AASHTO LRFD Bridge Design Specifications suggests the following load combinations for the SLS[3]:

$$F_{SLS} = 1.0 \times (g_1 + g_2) + 0.8 \times (\delta \times p_1 + p_2) \tag{4.9}$$

and for the ULS[4]:

$$F_{ULS} = 1.25 \times g_1 + 1.5 \times g_2 + 1.75 \times (\delta \times p_1 + p_2) \tag{4.10}$$

where g_1 stands for the dead load of structural components, g_2 for the dead load of wearing surfaces, p_1 for traffic load amplified by a dynamic load allowance factor $\delta = 1.33$, and p_2 for static traffic load. The multiplying factors in (4.9) and (4.10) are load factors.

While both limit states must satisfy static equilibrium, the first is a state where the structure is no longer able to perform the service for which it is designed; and the second is defined as the state of a structure subjected to the maximum possible load that it can sustain, so that any additional load would lead to a failure. Application of this concept to UHPC structures requires appropriate performance criteria that define the two limit states. In this work, we will adopt crack opening criteria, for both limit states:

- Restricting the crack width at the service limit to an admissible value may limit long-term durability problems, fatigue crack propagation problems under cyclic loading, etc. In this work, we will adopt a 'no cracking' criterion:

$$\max_{\underline{x}} \left[\left[w \left(F_{SLS} \right) \right] \right] \equiv 0 \Leftrightarrow \max_{\underline{x}} \left(\varepsilon^{p}_{M,I} \left(\underline{x} \right) \right) \equiv 0 \tag{4.11}$$

[3]The SLS load combination (4.9) corresponds to the "Service III" case of the Service Limit State of AASHTO LRFD Bridge Design Specification, related to tension in prestressed concrete structures with objective of crack control.

[4]The ULS load combination (4.10) refers to the "Strength I" case of the Strength Limit State defined in AASHTO LRFD Bridge Design Specification, which corresponds to the basic load combination related to normal vehicular use of the bridge without wind.

where $\varepsilon^p_{M,I}$ is the principal plastic strain of the UHPC matrix (first eigenvalue of plastic strain tensor $\underline{\underline{\varepsilon}}^p_M$).

- Restricting the crack width at the ultimate strength limit of UHPC is foremost a material performance criterion. It ensures the mechanical composite performance of the UHPC material in structural applications (i.e. stress transfer over cracks) and limits the risk of fiber pull-out or fiber breakage, which can induce localized cracks and ultimately, global structural softening and failure. In other words, it can be viewed as a ductility design criterion. In this work, we will adopt the crack width design criterion from the UHPC guidelines issued by the French Association of Civil Engineering (AFGC) [38], which distinguishes between unreinforced and reinforced UHPC sections:

$$\max_{\underline{x}} \left[[w\left(F_{ULS}\right)]\right] \leq \left\{ \begin{array}{l} [[w]]^{un}_{\text{lim}} = 0.3\,\text{mm}\left(= \dfrac{1}{85}\,\text{in}\right) \text{ for unreinforced section} \\ [[w]]^{re}_{\text{lim}} = \min\left(\dfrac{L_f}{4}; \dfrac{h}{100}\right) \text{ for reinforced section} \end{array} \right\} \tag{4.12}$$

or equivalently, in a dimensionless form, noting that $[[w]]_{\text{lim}}$ represent the total cumulative crack opening measured over a characteristic length $l_c = \frac{2}{3}h$:

$$\max_{\underline{x}} \left(\varepsilon^p_{M,I}\left(\underline{x}, F_{ULS}\right)\right) \leq \frac{[[w]]_{\text{lim}}}{l_c} = \left\{ \begin{array}{l} \varepsilon^{p,un}_{\text{lim}} = 1.5\dfrac{[[w]]^{un}_{\text{lim}}}{h} \text{ for unreinforced section} \\ \varepsilon^{p,re}_{\text{lim}} = \min\left(\dfrac{3L_f}{8h}; \dfrac{3}{200}\right) \text{ for reinforced section} \end{array} \right\} \tag{4.13}$$

L_f is the length of the fibers employed in the specific UHPC material, and h is the height of a beam- or plate-like UHPC structure. We have validated the AFGC design criterion for the FHWA tests in Section 3.4.

It is instructive to note that the AFGC crack opening design criterion for the reinforced section (4.12) actually defines the zero-stress cut-off of an overall stress-strain relation $\Sigma = \Sigma(E)$, following a material softening behavior (see Fig. 4-2). We do not consider this softening behavior in our material description (see Section 2.1) or in the design procedure, but only adopt the crack opening criterion in form of the plastic matrix strain criterion (4.13). In fact, the two-phase composite model for UHPC, which distinguishes the brittle behavior of the cementitious matrix from the ductile contribution of the reinforcing fibers in the overall

composite response, is a constitutive modeling interpretation of the overall stress-crack opening relation or a global stress-strain relation $\Sigma = \Sigma(E)$, which in our analysis is a result, not an input (as in the UHPC guideline [38]). Furthermore, the crack opening criterion –viewed as a ductility criterion– restricts the values of the plastic matrix strain $\underline{\underline{\varepsilon}}^p_M$ to values, for which a proper stress transfer from matrix to fiber is ensured. This allows us to avoid the use of global material softening relations, which are often the source of numerical (and physical) instability problems.

4.2.2 Optimization Procedure

We want to combine the design parameters and design criteria into an optimization procedure which will make it possible to find the optimized sections for UHPC bridge girders. For the sake of clarity, we will first consider the ultimate strength limit state. For the ULS, the control variable of the optimization problem is the maximum permanent strain of the UHPC matrix, $D = \max_{\underline{x}} \left(\varepsilon^p_{M,I}\left(\underline{x}\right)\right)$, which must satisfy the crack opening criteria $D \leq D_{\lim}$ (i.e. relation (4.13)).

The control variable D is a function of:

1. Structural geometric parameters, such as span L and section parameters, $S_{j=1,M}$ (such as slab width B, slab thickness T_s, the web-height H_w, the web thickness T_w, the bottom flange width and thickness, B_f and T_f, as detailed later on);

2. Prestressing parameters; the prestress pressure p and the effective level of prestressing γ;

3. The UHPC material parameters $R_{i=1,N}$, detailed in Section 2.3, and summarized in Table 2.1;

4. The load capacity F, which must be greater than or equal to the load level F_{ULS} defined by (4.10).

Thus, formally, for the ULS:

$$\left\{ \begin{array}{c} F \geq F_{ULS} \\ D = f\left(F, R_{i=1,N}, p, \gamma, L, S_{j=1,M}\right) \leq D_{\lim} \end{array} \right\} \tag{4.14}$$

- **Loi écrouissante** - *Strain hardening law*:

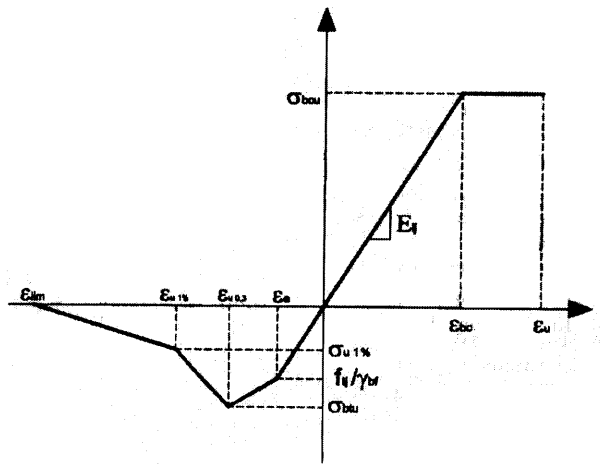

- **Loi adoucissante** - *Strain softening law* :

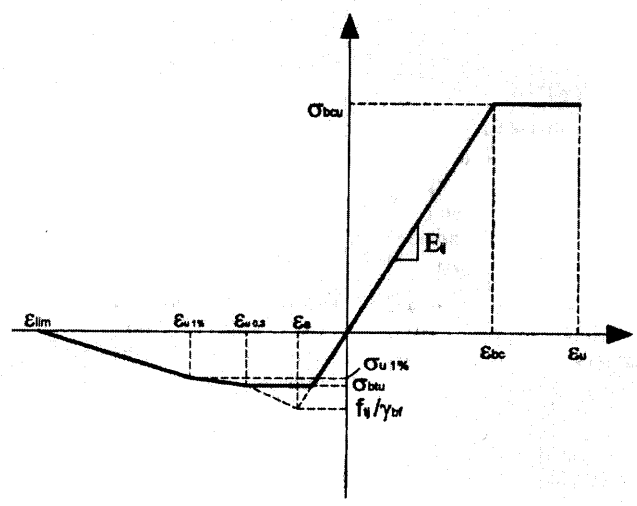

Figure 4-2: The stress-strain relation and the limiting strains of French UHPC guidelines [38]. $\varepsilon_{u,0.3}$ is the strain corresponding to the crack opening of $[[w]]^{un}_{\text{lim}} = 0.3\,\text{mm}$, i.e. $\varepsilon^{p,un}_{\text{lim}}$ in our report, and ε_{lim} is the same parameter as $\varepsilon^{p,re}_{\text{lim}}$ in our report.

or equivalently in a dimensionless form:

$$\left\{ \begin{array}{c} \bar{F}_{ULS} = \dfrac{F}{F_{ULS}} \geq 1 \\ \dfrac{D}{D_{\lim}} = \mathcal{F}\left(\bar{F}_{ULS}, \bar{R}_{i=1,N-1}, \bar{p} = \dfrac{p}{R_i}, \gamma, \bar{S}_{J=1,M} = \dfrac{S_{j=1,M}}{L}\right) \leq 1 \end{array} \right\} \tag{4.15}$$

$\bar{R}_i$ stands for the $N-1$ material property invariants of the UHPC material. For instance, the ductility ratio (2.28) is such a quantity; others are the postcracking-to-precracking stiffness ratio, the ultimate strength-to-cracking strength ratio, etc. (for details see [13]):

$$\bar{R}_1 = \frac{k_M}{f_t}; \bar{R}_2 = \frac{K_1}{K_0}; \bar{R}_3 = \frac{\Sigma_y^B}{\Sigma_t}; ... \tag{4.16}$$

$\bar{S}_{J=1,M}$ represent section parameters normalized by the span length. They are the focus of the optimization procedure for UHPC sections.

If we note that the UHPC material invariants $\bar{R}_{i=1,N}$ are fixed values in our optimization process, the optimization problem can be formulated as follows: Find the minimum values of the set of invariants $\bar{p}, \gamma, \bar{S}_{J=1,M}$ (or any combination of them) such that

$$\frac{D}{D_{\lim}} = \mathcal{F} \rightarrow 1 \text{ for } \bar{F}_{ULS} = 1 \tag{4.17}$$

Analogously, for the SLS for which $D_{\lim} = 0$:

$$\forall \bar{F}_{SLS} = \frac{F}{F_{SLS}} \geq 1; \ \mathcal{F}\left(\bar{F}_{SLS}, \bar{R}_{i=1,N-1}, \bar{p}, \gamma, \bar{S}_{J=1,M}\right) \equiv 0 \tag{4.18}$$

4.3 1-D Optimization: Primary Section Parameters

As a first application of the developed design strategy, we propose to determine the minimum section height H' required for single span bridge girders suitable for precast UHPC solutions, that correspond to the span range:

$$L \in [21.3\,\text{m}\ (70\,\text{ft})\,; 36.6\,\text{m}\ (120\,\text{ft})] \tag{4.19}$$

For this optimization problem, we will employ the 1-D section design formula developed in Section 4.1. Given the focus on the minimum section height H', the design parameters that will be fixed in this first application are:

1. The span length range (4.19) and the deck and bottom flange section of the two-point section model, leaving the height H' as the only free section geometry parameter to be optimized.

2. The prestressing parameters, $\bar{p}$ and γ: we consider two prestressing forces, 4.45 MN (1,000 kips) and 6.68 MN (1,500 kips) per traffic lane, and a prestress level $\gamma = 0.80$, which are within a large range of commonly accepted prestressing forces for mid-span bridge girders;

3. The material property invariants $\bar{R}_{i=1,N-1}$: we employ the DUCTAL^{TM} material properties given in Table 2.1; and standard values for the prestressing tendon properties, $f_y^T = 1,870$ MPa (270 ksi) and $E_T = 200$ GPa (29,000 ksi);

4. The load $\bar{F}_{ULS} = 1$: the ultimate strength limit state load combination (4.10) defines the design moment M_u^{load} for the section model.

4.3.1 Section Parameters

The design focus is a single span, one traffic lane girder. The span range is fixed by (4.19), and the traffic lane has a width of $B = 3.66$ m (12 ft). Given the high compressive strength of UHPC, it is advantageous to consider the slab to be integrated into the girder system as a top flange. For reasons which will be clarified later, we fix the deck thickness to $T_s = 0.102$ m (4 in).

4.3.2 Prestressing Parameters

The bottom flange section is fixed to the size required to accommodate the prestressing tendons. That is, the number N of prestressing tendons is restricted by two conditions: (1) N must be greater than or equal to the minimum number of tendons required to realize a specific prestressing forces in the section; (2) N must be smaller than or equal to the maximum number

of tendons that fit into the bottom flange. These conditions are expressed by:

$$\frac{P}{\gamma f_y^T A_{s,tendon}} = N_{\min} \leq N \leq N_{\max} = \left\langle \frac{B_f}{c} - 1 \right\rangle \times \left\langle \frac{T_f}{c} - 1 \right\rangle \tag{4.20}$$

where $P = pA_f$ is the total prestress force in the girder; $A_{s,tendon}$ is the cross-sectional area of an individual tendon; $\gamma \leq 1$ is the (effective) level of prestressing, f_y^T is the strength of the prestressing tendons; $\langle a \rangle$ denotes the greatest non-negative integer that satisfies $\langle a \rangle \leq a$; and c stands for the minimum distance between tendons and the concrete cover. In the optimization procedure, $c = 5.1\,\text{cm}$ (2 in) is considered, and the bottom flange size is fixed to $A_f = 0.90 \times 0.15\,\text{m}^2$ ($36 \times 6\,\text{in}^2$), which can host roughly 30 tendons. This number of tendons can achieve the two considered prestress force levels, $P_{1,000} = 4.45\,\text{MN}$ (1,000 kips) and $P_{1,500} = 6.68\,\text{MN}$ (1,500 kips) per traffic lane. For the considered prestress level $\gamma = 0.80$ with a prestressing ratio[5] of $c_T = 2.2\%$ and $c_T = 3.3\%$, we obtain an effective prestress pressures of $p_{1,000} = 33.0\,\text{MPa}$ (4.79 ksi) and $p_{1,500} = 49.5\,\text{MPa}$ (7.17 ksi).

4.3.3 UHPC Composite Material Parameters

The model parameters for the UHPC material are those of DUCTAL^{TM} given in Table 2.1. These model parameters are modified for the prestressed bottom flange to deliver the effective composite properties defined by (3.4) and (3.6). The parameter values for the UHPC with a tendon effect are provided in Table 4.1, where "UHPC-1,000" and "UHPC-1,500" stand for the effective UHPC properties of the bottom flange prestressed with $P_{1,000} = 4.45\,\text{MN}$ (1,000 kips) and $P_{1,500} = 6.68\,\text{MN}$ (1,500 kips), respectively.

4.3.4 Design Moment

The design moment is determined on the basis of the load combination (4.10) defined by current U.S. design codes for a bridge girder [5,6]. In addition to the dead load, the loads include the traffic load of a design truck (or a tandem load) and a uniform traffic lane.

[5] Note, from (3.1) and (3.2):

$$c_T = \frac{P/A_f}{\gamma f_y^P}$$

Model Parameter	UHPC Only		UHPC-1,000		UHPC-1,500	
	SI	IU	SI	IU	SI	IU
C_M	53.9 GPa	(7,820 ksi)	53.9 GPa	(7,820 ksi)	53.9 GPa	(7,820 ksi)
C_F	0	0	**4.4** GPa	(**640** ksi)	**6.5** GPa	(**950** ksi)
M	1.65 GPa	(240 ksi)	1.65 GPa	(240 ksi)	1.65 GPa	(240 ksi)
ν	0.17		0.17		0.17	
f_t	0.7 MPa	(0.1 ksi)	0.7 MPa	(0.1 ksi)	0.7 MPa	(0.1 ksi)
k_M	6.9 MPa	(1.0 ksi)	6.9 MPa	(1.0 ksi)	6.9 MPa	(1.0 ksi)
σ_{Mc}	190 MPa	(28 ksi)	190 MPa	(28 ksi)	190 MPa	(28 ksi)
σ_{Mb}	220 MPa	(32 ksi)	220 MPa	(32 ksi)	220 MPa	(32 ksi)
f_y	4.6 MPa	(0.67 ksi)	**12.7** MPa	(**1.85** ksi)	**16.7** MPa	(**2.43** ksi)
σ_{Fc}	10 MPa	(1.5 ksi)	**30** MPa	(**4.4** ksi)	**30** MPa	(**4.4** ksi)
Σ_y^B	11.5 MPa	(1.67 ksi)	**19.6** MPa	(**2.81** ksi)	**23.6MPa**	(**3.42** ksi)

Table 4.1: Values of 'effective' UHPC model parameters. Bold characters denote changes made in material parameters.

Dead Loads

The nominal self-weight of the UHPC-bridge girder is calculated by integration of the product of mass density of UHPC ($\rho = 2,500\,\mathrm{kg}\,/\,\mathrm{m}^3$ ($0.09\,\mathrm{lb}\,/\,\mathrm{in}^3$)) and gravity $g = 9.81\,\mathrm{m}\,/\,\mathrm{s}^2$ over the structural volume V:

$$\text{in}\, V : G_1 = \int_V g_1 dV; \;\; g_1 = \rho g = 24.5\,\mathrm{kN}\,/\,\mathrm{m}^3 \;\; (0.09\,\mathrm{lbf}\,/\,\mathrm{in}^3) \tag{4.21}$$

In addition to the self-weight of the girder, most states in the U.S. require consideration of a future wearing surface that represents an overlay of concrete or asphalt acting on the composite section of the girder and slab [22, 41]. A typical value is $122\,\mathrm{kg}\,/\,\mathrm{m}^2$ ($25\,\mathrm{lb}\,/\,\mathrm{ft}^2$):

$$\text{on}\, A : g_2 = 1.2\,\mathrm{kPa} \;\; (0.17\ \mathrm{psi}) \tag{4.22}$$

While consideration of this load case in the optimization process can be debated, its inclusion provides a conservative estimates for the applied dead loads. Dead loads from other structural components, such as traffic barriers, are not taken into account in the design process.

Live Loads

The live load scenario we consider here consists of:

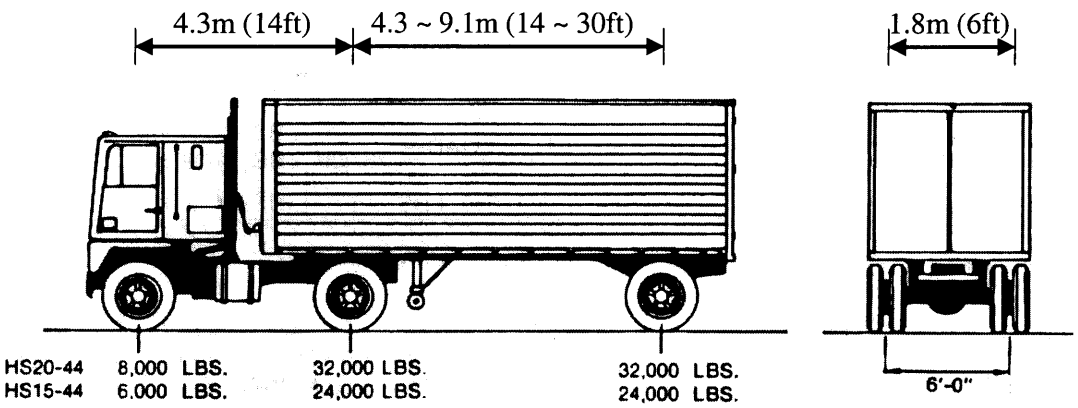

Figure 4-3: Design truck load from AASHTO Standard Specifications [5].

1. The design truck load, HS-20, or alternatively a design tandem load, whichever is governing;

2. A distributed lane load.

While AASHTO Standard Specifications stipulates the use of either truck or distributed lane load, LRFD Specifications requires superposition of the truck and the lane load. This superposition, named HL-93, is adopted in the design procedure here.

Design Truck Load HS-20 The design truck load HS-20, listed in the AASHTO Standard Specifications, has a total load $P_1 = 320\,\text{kN}$ (72 kips) that is distributed over three axles as shown in Figure 4-3. The first and the second axle are spaced $4.27\,\text{m}$ ($14\,\text{ft}$) apart, and the spacing between the second and the third axle can vary between $4.27 - 9.14\,\text{m}$ ($14 - 30\,\text{ft}$) to achieve the maximum force effect. Each axle is composed of two sets of wheels, such that each wheel load corresponds to:

$$\text{on the first axle} \quad : \quad P_{w1} = 17.8\,\text{kN} \ \ (4 \text{ kips}) \tag{4.23}$$

$$\text{on the second and third axle} \quad : \quad P_{w2} = 71.2\,\text{kN} \ \ (16 \text{ kips}) \tag{4.24}$$

and the total load is:

$$P_1 = 2P_{w1} + 2 \times (2P_{w2}) \tag{4.25}$$

AASHTO Standard Specifications provides for a "tire contact area" $b_w = 0.51$ m (20 in) wide (transverse to the bridge) and $l_w = 0.25$ m (10 in) long (along the length of the bridge). A wheel load, consisting of either one or two tires, is uniformly distributed over this contact area $A_w = 0.129$ m^2 (200 in^2). The wheel surface pressure on A_w is:

$$\text{on the first axle } A_{w1} \quad : \quad p_1^1 = \frac{P_{w1}}{A_w} = 138\,\text{kPa} \ \ (20 \text{ psi}) \tag{4.26}$$

$$\text{on the second and third axle } A_{w2} \text{ and } A_{w3} \quad : \quad p_1^{2-3} = \frac{P_{w2}}{A_w} = 552\,\text{kPa} \ \ (80 \text{ psi}) \tag{4.27}$$

As an alternative to the truck load model, AASHTO Standard Specifications defines a design tandem load: a pair of 111 kN (25 kips) axle loads spaced 1.22 m (4 ft) apart. The nominal value of the tandem load is much smaller than the design truck load and therefore is not further investigated for the design of the beam girders in the considered span range.

Distributed Lane Load AASHTO Standard Specifications defines a uniformly distributed lane load of 950 kg / m (640 lb / ft) per traffic lane, which translates into a surface load on the bridge slab of width $B = 3.66$ m (12 ft):

$$\text{on } A : p_2 = 2.6\,\text{kPa} \ \ (0.37 \text{ psi}) \tag{4.28}$$

Table 4.2 summarizes the nominal values for the loads considered in this study, along with the partial load factors for SLS and ULS for the load combinations specified by (4.9) and (4.10). Note that the nominal values of the truck load (p_1^1 and p_1^{2-3}) are multiplied by the dynamic impact factor of $\delta = 1.33$.

Determination of the Design Moment

The design moment is obtained by positioning the truck load at the location where it produces the maximum flexural load. The maximum moment occurs if the truck is positioned near the center with its middle axle located off-center by 0.710 m (2.33 ft). For the single span beam,

Load	γ_{SLS}	γ_{ULS}	Domain	Nominal Load	
			Dead Loads		
$g_1 = \rho g$	1.0	1.25	V	24.5 kPa / m	(0.09 lbf / in^3)
g_2	1.0	1.5	A	1.2 kPa	(0.17 psi)
			Live Loads		
p_1^1	0.8	1.75	$A_w^{(3D)} = l_w b_w$ $A_w^{(2D)} = l_w B^{(*)}$	138 kPa 19.2 kPa	(20 psi) (2.8 psi)
p_1^{2-3}	0.8	1.75	$A_w^{(3D)} = l_w b_w$ $A_w^{(2D)} = l_w B^{(*)}$	552 kPa 76.6 kPa	(80 psi) (11 psi)
p_2	0.8	1.75	A	2.6 kPa	(0.37 psi)

Table 4.2: Summary of loads: nominal loads, partial load factors, and design loads. (*) For 2-D simulations, the wheel load p_2 is smeared out over the traffic lane of width $B = 3.6576$ m (12 ft), i.e. $p_2(2D) = p_2(3D)b_w/B$, where $b_w = 0.51$ m (20 in) is the transversal tire width.

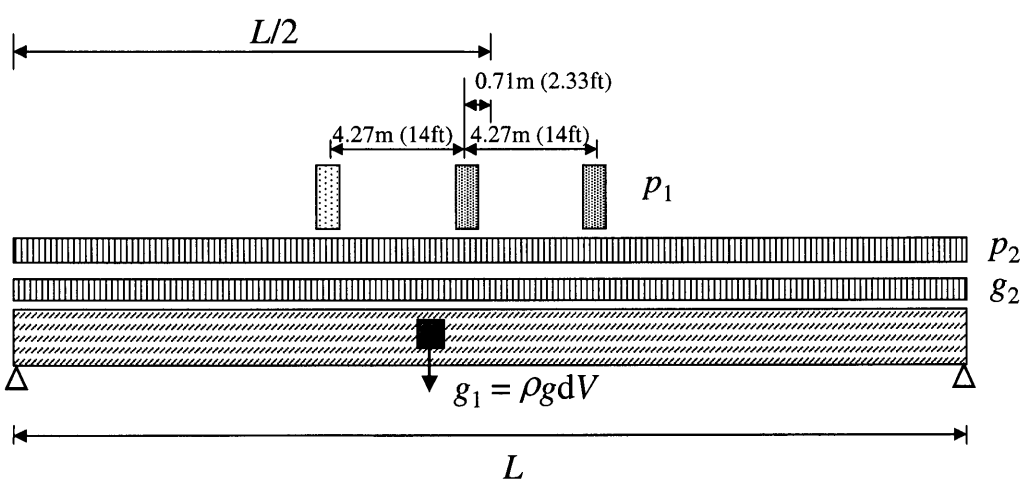

Figure 4-4: Load configuration for maximum moment.

Span (L) (m/ft)	Dead Loads		Live Loads		M_u^{load} (MN m/kips ft)
	M_{g1} (*) (MN m/kips ft)	M_{g2} (MN m/kips ft)	M_{p1} (MN m/kips ft)	M_{p2} (MN m/kips ft)	
21.3 (70)	0.90 (660)	0.25 (180)	1.34 (990)	0.53 (390)	5.53 (4,080)
24.4 (80)	1.17 (860)	0.33 (240)	1.58 (1,160)	0.69 (510)	6.84 (5,040)
27.4 (90)	1.48 (1,090)	0.41 (300)	1.82 (1,340)	0.88 (650)	8.25 (6,080)
30.5 (100)	1.83 (1,350)	0.51 (380)	2.07 (1,520)	1.08 (800)	9.76 (7,200)
33.5 (110)	2.22 (1,640)	0.62 (450)	2.31 (1,700)	1.31 (970)	11.36 (8,380)
36.6 (120)	2.64 (1,950)	0.73 (540)	2.55 (1,880)	1.56 (1,150)	13.07 (9,640)

Table 4.3: Summary of maximum moment for various spans. (*) The self-weight is calculated assuming cross sectional area of $A = 0.645\text{m}^2$ (1000in^2).

the moment is readily calculated considering the load configuration in Figure 4-4. Table 4.3 provides details of this calculation of the form:

$$M_u^{load} = \max\left(1.25M_{g1} + 1.5M_{g2} + 1.75\left(1.33 \times M_{p1} + M_{p2}\right)\right) \tag{4.29}$$

where M_i represent the bending moment of load case i.

4.3.5 Minimum Height Prediction

The determination of the minimum height H' from the two-point section model may be an iterative process. First, we will assume that the crack opening criterion is satisfied, and determine the height from the design formula (4.5), for $f = 1$, in the dimensionless form:

$$\frac{H'}{L} \geq \frac{\bar{m}_u}{1+\bar{p}}; \quad \bar{m}_u = \frac{M_u^{load}}{\Sigma_y^B A_f L} \tag{4.30}$$

where $\bar{p}_{1,000} = 1.684$ and $\bar{p}_{1,500} = 2.098$ for the two considered prestress cases (UHPC-1,000 and UHPC-1,500). Then, with the values of determined from (4.30) we check the crack opening assumption at yield, i.e.,

$$f = \min\left(\frac{\Sigma_{\text{lim}}^B}{\Sigma_y^B}, 1\right) \equiv 1 \tag{4.31}$$

where we employ relation (4.8) for Σ_{lim}^B along with the crack opening criterion (4.13), in which the admissible plastic crack opening criterion is a function of the previously determined girder height, i.e. $\varepsilon_{\text{lim}}^{p,re}(H')$. If $f = 1$, the determined girder height H' is the solution of the design

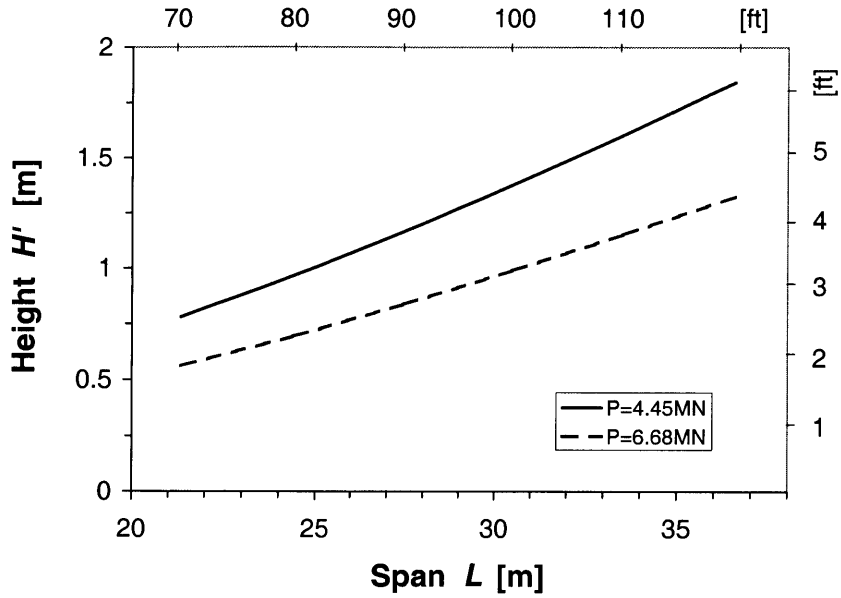

Figure 4-5: H' versus span L using the design formula, for two prestressing forces.

problem. By contrast, if $f < 1$, iterations are required,

$$\left(\frac{H'}{L}\right)_{iter} \geq \frac{\bar{m}_u}{f_{iter-1} + \bar{p}} \tag{4.32}$$

until criterion (4.31) is met.

Table 4.4 summarizes the dimensionless input and output parameters for the considered span range. Figure 4-5 displays the results of the optimization process: total girder height $H = H' + \frac{1}{2}(B_f + T_s)$ versus span L for the two prestress cases. In the considered span range, the difference in minimum height between the two prestress scenarios is roughly 30%. That is, an increase of the prestressing by 50% allows a reduction of the beam height by 30%.

4.4 Summary of UHPC Design Strategy

The 1-D section model outlined in this chapter provides a first-order engineering design formula for the optimization of prestressed UHPC girder sections as well as insight into how to optimize UHPC structures:

Span (L) (m/ft)	Input $\bar{m}_u = \frac{M_u^{load}}{\Sigma_y^B A_f L}$ [×1000]		Output H'/L [×1000]	
	UHPC-1,000 $\bar{p}_{1,000} = 1.684$	UHPC-1,500 $\bar{p}_{1,500} = 2.098$	UHPC-1,000	UHPC-1,500
21.3 (70)	97.9	81.3	36.5	26.3
24.4 (80)	106	88.0	39.5	28.4
27.4 (90)	114	94.4	42.3	30.5
30.5 (100)	121	100	45.1	32.4
33.5 (110)	128	106	47.7	34.3
36.6 (120)	135	122	50.3	36.2

Table 4.4: Input - output parameters of the optimization process.

- Beside equilibrium conditions (section equilibrium in the 1-D section design formula), UHPC design requires crack opening criteria to define the service limit state and the ultimate strength limit state. In this work, we adopt a 'no cracking' criterion for the SLS and the ULS crack opening criterion from the UHPC guidelines issued by AFGC [38]. Optimization requires a UHPC structural performance which satisfies both conditions, equilibrium of the SLS and ULS load levels and the crack opening criteria. We will employ this design strategy in the next chapter, which is devoted to a detailed model-based design of highway bridge girders made of UHPC.

- Significant design parameters of UHPC structures relate to geometry, material behavior and loads. They are suitably represented in a dimensionless form. This not only reduces the number of varying parameters considerably, but also enables the identification of key invariants of UHPC design. Beside load, section, and material invariants, the dimensionless parameter $\bar{p}$ (defined by (??)) appears to be of particular importance, since it represents an effective tendon-to-UHPC strength ratio. The higher $\bar{p}$ is, the more pronounced the contribution of the prestressing tendon to the overall moment capacity of the UHPC section, which increases linearly with $\bar{p}$. We will investigate this invariant further in the next chapter.

Chapter 5

MODEL-BASED DESIGN

In this second chapter on model-based optimization, there are three main objectives: (1) to apply the design strategy developed in Chapter 4 to the detailed section design of UHPC highway bridge girders and by doing so (2) to validate the developed 1-D design formula by means of detailed 2-D and 3-D nonlinear finite element simulations; and finally, (3) to check the feasibility of the solution for one-span and two-span bridge girder systems. The 3-D UHPC model and its finite element implementation are at the heart of the model-based design methodology. The chapter begins with a brief review of section solutions for prestressed concrete, which are then adapted for UHPC section design. Using double-tee girders, we perform a systematic study on minimum section parameters of single-span bridge girders in the $21 - 36\,\mathrm{m}$ ($70 - 120\,\mathrm{ft}$) span range and compare these results with those obtained from the 1-D section design formula of Section 4.1. Optimized sections for the considered span range for single-span bridge girder systems are proposed and the suitability of the section solutions for two-span continuous girder systems is discussed.

5.1 Design Parameters

The efficiency of a bridge girder design depends not only on the traffic load, but also on constructibility, availability of formwork, and transportability to the site. It is common practice to categorize bridge systems in three span ranges: short span ($6 - 21\,\mathrm{m}$ ($20 - 70\,\mathrm{ft}$)), medium span ($21 - 36\,\mathrm{m}$ ($70 - 120\,\mathrm{ft}$)) and long span ($36 - 107\,\mathrm{m}$ ($120 - 350\,\mathrm{ft}$)). The current bridge

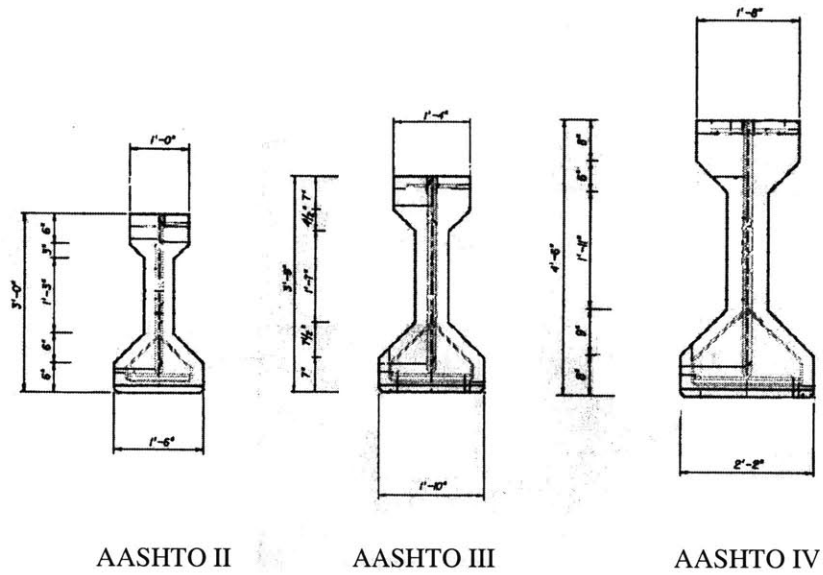

Figure 5-1: AASHTO standard girder types. [3]

system in the U.S. is composed primarily of precast short and medium span bridges, and though the higher strength of UHPC allows longer spans than traditional concrete, transportation considerations such as weight and stability will typically limit the length of an individual precast element to roughly 45 m (150 ft) [22].

5.1.1 Common Section Types

Because of their efficient flexural resistance, $\mathcal{I}$-section type girders currently dominate the domestic precast bridge system. Some of the standard section profiles issued by the American Association of State Highway and Transportation Officials (AASHTO) are shown in Figure 5-1. While $\mathcal{I}$-sections may also be useful for UHPC girders, the superior tensile, shear, and compressive properties of UHPC should enable slimmer and shallower profile designs for UHPC girders while completely eliminating the need for passive reinforcement and shear stirrups. Similarly, a UHPC slab, which does not require transverse reinforcement, can be significantly thinner than standard reinforced concrete decks. It is suggested that the slab and the girder be cast and erected in a single piece, which will significantly reduce construction costs. Furthermore, the

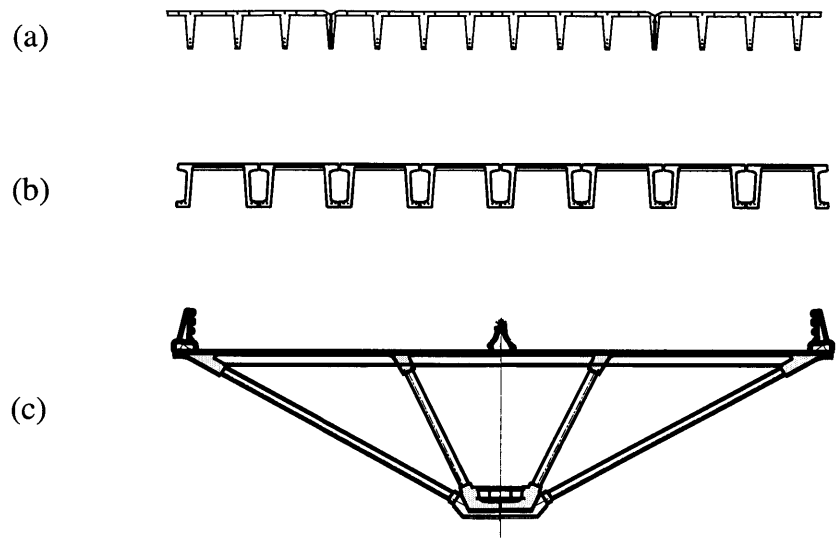

Figure 5-2: Examples of UHPC girder design for (a) Short spans ($L < 21\,\mathrm{m}$ (70 ft)); (b) Medium spans ($21 - 36\,\mathrm{m}$ ($70 - 120\,\mathrm{ft}$)); and (c) long spans ($L > 36\,\mathrm{m}$ (120 ft)); from [35].

high durability of UHPC (high abrasion resistance, extremely low permeability, etc.) should make the integrated UHPC girder-slab system economically efficient in the long term. Examples of UHPC girder designs for different span ranges are illustrated in Figure 5-2: deck panel type sections (Fig. 5-2 (a)) are appropriate for shorter spans ($L < 21\,\mathrm{m}$ (70 ft)) in which a small number of prestressing tendons (if any) is needed. For medium spans ($21 - 36\,\mathrm{m}$ ($70 - 120\,\mathrm{ft}$)), double tee or π-sections (Fig. 5-2 (b)) are appropriate design solutions as their box-shaped assembly minimizes the exposure of the prestressed bottom flange to aggressive environments. For longer spans ($L > 36\,\mathrm{m}$ (120 ft)), space truss structures (Fig. 5-2 (c)) or post-tensioned segmental systems are required.

5.1.2 Choice of Section Profile and Section Parameters

In this study, we focus on the medium span range for precast UHPC applications and select the double-tee (or π-section) type for further optimization. A more detailed illustration of this section type is given in Figure 5-3 which displays the main section parameters that will be

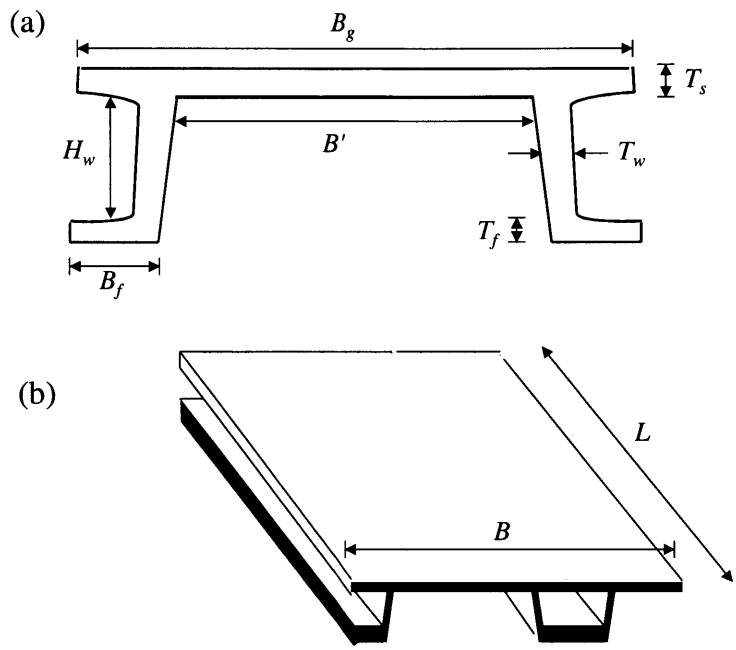

Figure 5-3: Double-tee or π-section girder: (a) Section; (b) 3-D view of a traffic lane, where $B_g = 2B/3$.

considered in the optimization procedure. These are:

- The girder slab width B_g, which is determined by the number of girders per traffic lane of width $B = 3.66\,\mathrm{m}$ (12 ft). For double-tee sections, it is customary to use one girder per lane (i.e. $B_g \equiv B$) or three girders for every two traffic lanes (i.e. $B_g \equiv 2B/3$). The latter case will be pursued in this study.

- The slab thickness T_s and the web spacing $B' = B_g - 2B_f$ (B_f stands for the bottom flange width). Both play an important role in the 3-D structural performance of the slab system.

- The web height and web width, H_w and T_w. The first plays an important role for deflection and vibration control in service conditions and the flexural resistance vis-à-vis failure. The second affects the shear resistance, which is important since no shear reinforcement is used in UHPC girders.

- The bottom flange size, width B_f and height T_f. The primary function of the bottom flange is to accommodate the required number N of prestressing tendons. For the double-tee section displayed in Figure 5-3, the maximum number of prestressing tendons is constrained by[1]:

$$N \leq N_{\max} = 3 \times \left[\left\langle \frac{B_f}{c} - 1 \right\rangle \times \left\langle \frac{T_f}{c} - 1 \right\rangle \right] \tag{5.1}$$

  where $\langle a \rangle$ denotes the greatest non-negative integer that satisfies $\langle a \rangle \leq a$; and $c = 5.1\,\text{cm}$ ($2\,\text{in}$) stands for the minimum distance between tendons and the concrete cover.

The set of section parameters $S_{j=1,M} = (B_g, T_s, H_w, T_w, B_f, T_f)$ are considered in the section optimization procedure defined by (4.15), (4.17) and (4.18).

5.1.3 Load and Modeling of Loading

The load cases we consider in the 2-D and 3-D finite element simulations are those defined by current U.S. design codes for bridge girders [5, 6]. We introduced these load cases in Section 4.3.4 and refer to the nominal values in Table 4.2. In addition, in model-based simulations, the nonlinear nature of the stress-strain relation of UHPC materials makes it necessary to define a chronology of load application to reach the target level of the service limit state (SLS),

$$F_{SLS} = 1.0 \times (g_1 + g_2) + 0.8 \times (\delta \times p_1 + p_2) \tag{4.9}$$

and of the ultimate strength limit state (ULS):

$$F_{ULS} = 1.25 \times g_1 + 1.5 \times g_2 + 1.75 \times (\delta \times p_1 + p_2) \tag{4.10}$$

The loads are applied in an incremental way to the structural system according to the following load application chronology (Fig. 5-4):

1. Dead load $\gamma_{g_1} \times g_1$ + Prestressing. In the first step, the girder's self-weight and the

[1] Relation (5.1) is similar to (4.20) which we employed in the 1-D section optimization. The factor 3 in (5.1) refers to the number of bottom flange sections per traffic lane under consideration.

equivalent prestressing stress p is applied simultaneously. This load phase mimics the pre-tensioning and load prior to employment of the girder in structural application.

2. Dead load $\gamma_{g_2} \times g_2$. The second load phase corresponds to the potential future (non-load bearing) wearing surface.

3. Live load $\gamma_p \times (\delta \times p_1 + p_2)$. The combination of the live loads is applied in a third loading phase, after the complete application of the dead loads. The live loads are gradually increased in load steps of 10% of the nominal value $\delta \times p_1 + p_2$ up to γ_p times the nominal value.

This load chronology scheme is employed for both the service limit state analysis and the ultimate strength limit state analysis. The analyses are carried out with the finite element implementation of the UHPC model in CESAR-LCPC (for validation see Chapter 3). In the simulations, iterations are performed at each load step to ensure convergence of the magnitude of the vector of residual forces to a tolerance of less than 5%.

5.2 2-D Optimization: Validation of Design Formula

The first objective of the model-based simulations is to validate the 1-D section design formula developed in Chapter 4. This is achieved by using 2-D finite element simulations of the considered bridge girder sections. Furthermore, the bridge girder section was optimized for the ULS using an iterative procedure. Finally, the optimized section was checked for viability with respect to the SLS and shear loads. For this 2-D optimization, we considered a single span, simply supported double-tee girder section in the span range $21 - 36\,\mathrm{m}$ $(70 - 120\,\mathrm{ft})$ meant to support one lane of traffic.

5.2.1 2-D Section Modeling

In the finite element simulations, the double-tee section girders are modeled in 2-D with solid plane stress finite elements. The FE meshes are comprised primarily of four-noded quadrilateral elements with some three-noded triangular elements. To model the irregular girder cross section, the girder is partitioned along its height into three subdivisions of varying width as illustrated

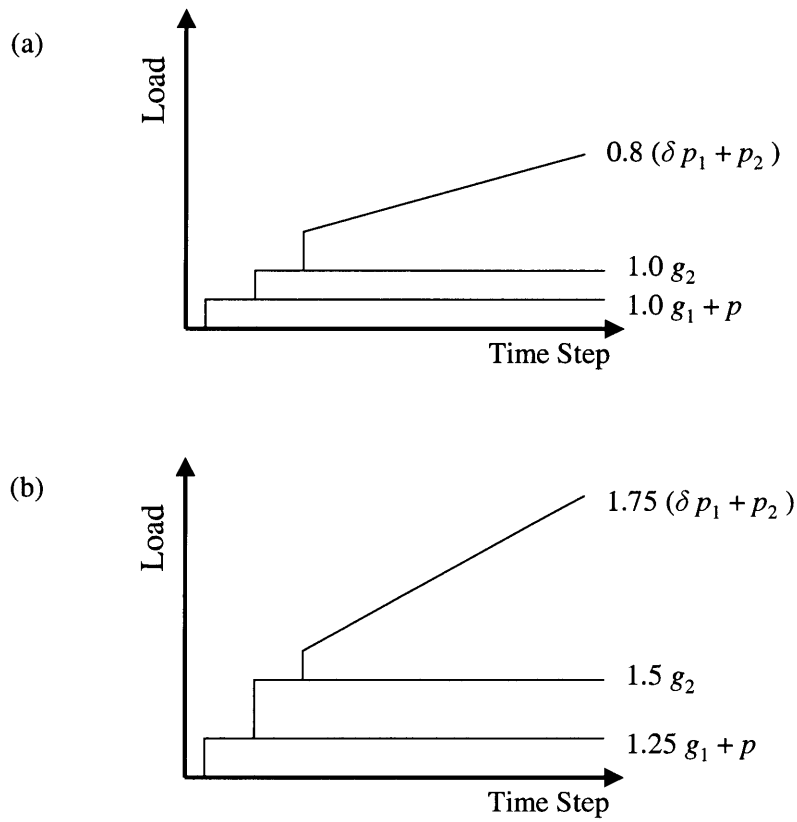

Figure 5-4: Load chronology scheme applied in model-based simulations for (a) Service limit state analysis; (b) Ultimate strength limit state analysis.

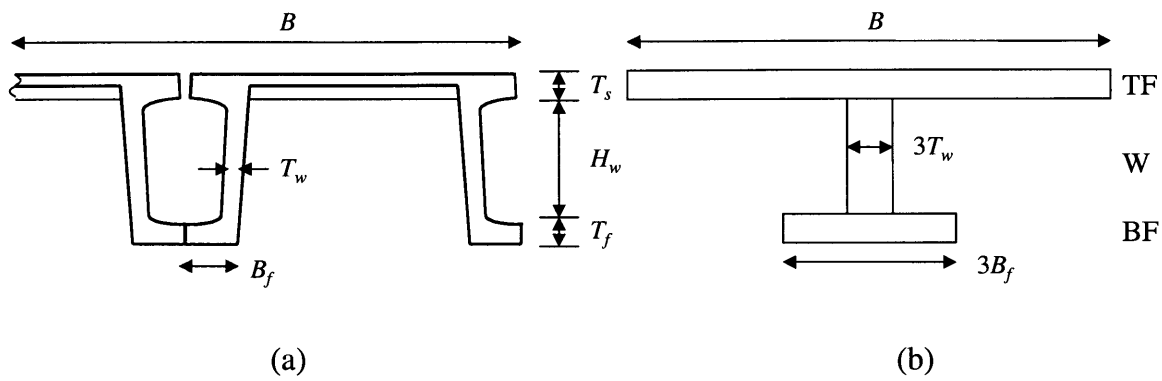

Figure 5-5: Cross section of double-tee girder: (a) Actual beam; (b) Idealized 2-D modeling in finite element simulation.

in Figure 5-5 (b): the prestressed bottom flange (BF, total width per traffic lane $3B_f$, height T_f), the unreinforced web (W, web height H_w, total web width per traffic lane $3T_w$), and the unreinforced top deck (TF, slab width B, slab thickness T_s). Each 2-D solid finite element was assigned a thickness according to its width.

5.2.2 Global Optimization Results: ULS Flexural Resistance

The loading scheme for flexure resistance is illustrated in Figure 5-6 (a). It is the same as the one used in Section 4.3 (i.e. Fig. 4-4). Figure 5-7 (a) displays a typical 2-D mesh with the boundary conditions and load application locations; Figure 5-7 (b) shows a typical deformed shape obtained by finite element simulation and Figure 5-7 (c) the corresponding principal plastic strain in the composite matrix at the ultimate strength limit state.

Within the considered span range, the beam height was optimized according to the ULS optimization criterion (4.15) and (4.17):

$$\left\{ \begin{array}{c} \bar{F}_{ULS} = \dfrac{F}{F_{ULS}} = 1 \\ \dfrac{D}{D_{\lim}} = \mathcal{F}\left(\bar{F}_{ULS}, \bar{R}_{i=1,N-1}, \bar{p}, \gamma, \bar{S}_{J=1,M} = \dfrac{S_{j=1,M}}{L}\right) \rightarrow 1 \end{array} \right\} \tag{5.2}$$

The parameters which were first set in Section 4.3 for the 1-D optimization were unchanged for

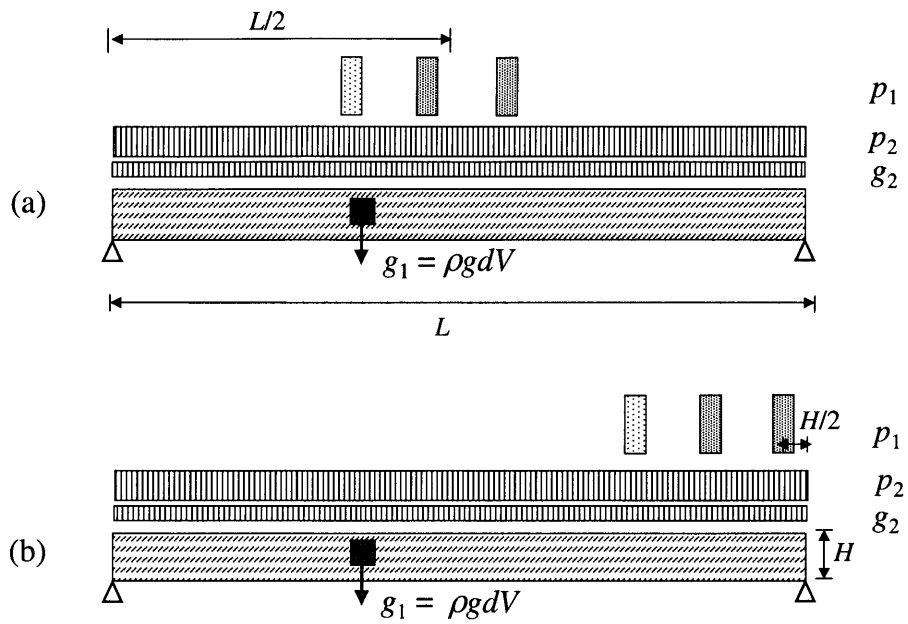

Figure 5-6: Loading scheme for (a) flexure and (b) shear.

the 2-D optimization:

1. Among the 2-D section parameters $S_{j=1,M} = (B, T_s, H_w, 3T_w, 3B_f, T_f)$,

$$\begin{aligned} S_{j=1,M} &= (B = 3.66\,\mathrm{m}, T_s = 0.10\,\mathrm{m}, H_w, 3T_w = 0.15\,\mathrm{m}, 3B_f = 0.90\,\mathrm{m}, T_f = 0.15\,\mathrm{m}) \\ &= (B = 12\,\mathrm{ft}, T_s = 4\,\mathrm{in}, H_w, 3T_w = 6\,\mathrm{in}, 3B_f = 3\,\mathrm{ft}, T_f = 6\,\mathrm{in}) \end{aligned} \tag{5.3}$$

   leaving the web height H_w as the only free geometrical degree of freedom in the optimization procedure. The web height also enters the maximum crack opening criterion (4.13) for reinforced sections (here the prestressed bottom flange):

$$D_{\lim} \equiv \varepsilon_{\lim}^{p,re} = \frac{3L_f}{8\,(H_w + T_s + T_f)} \tag{5.4}$$

   where $L_f = 13\,\mathrm{mm}$ (0.5 in) is the length of the reinforcing fibers in DUCTAL^{TM}.

2. The prestressing parameters, $\bar{p}$ and γ: we consider a prestress level $\gamma = 0.80$ for two

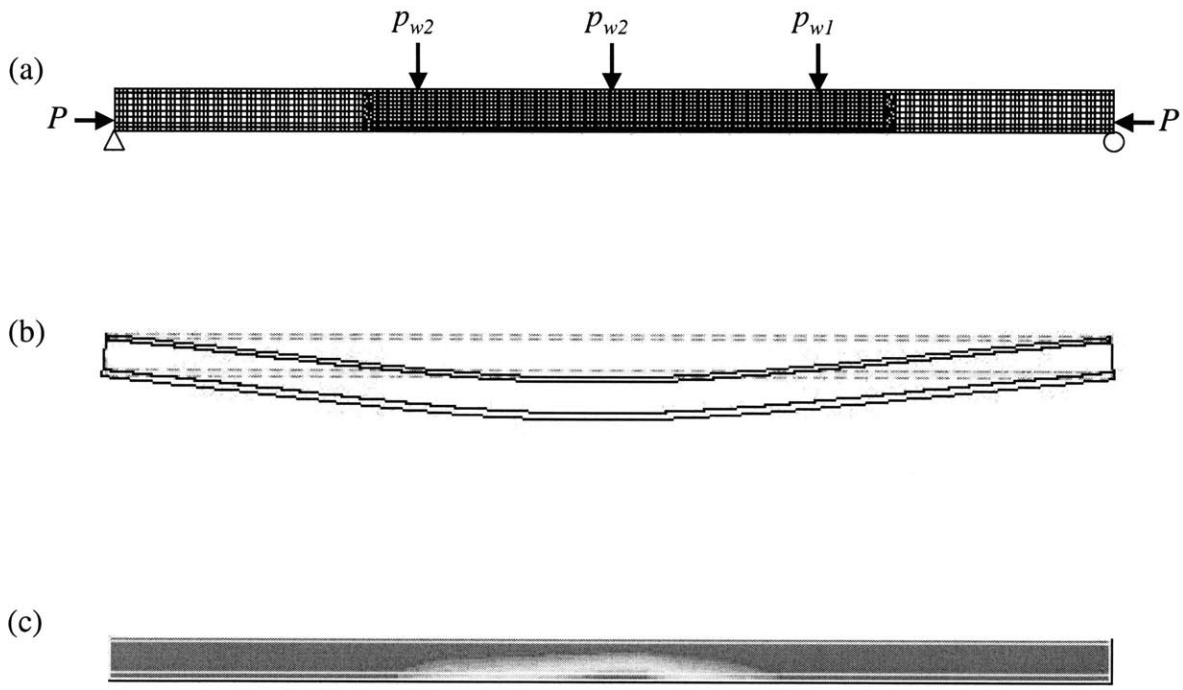

Figure 5-7: Model-based simulation of flexural loading of the girder with $L = 21.3\,\mathrm{m}$ (70 ft): (a) Mesh with boundary conditions and loads; (b) Deformed shape; (c) Composite matrix plastic strains.

prestressing cases, $P_{1,000} = 4.45\,\text{MN}$ (1,000 kips) and $P_{1,500} = 6.68\,\text{MN}$ (1,500 kips) per traffic lane. Using Eq. ?? with values from Table 4.1 we obtain:

$$\bar{p}_{1,000} = 1.684;\ \bar{p}_{1,500} = 2.098 \tag{5.5}$$

3. The material property invariants $\bar{R}_{i=1,N-1}$ of DUCTAL^{TM} (see Table 4.1).

Figure 5-8 displays typical results of the optimization iteration process in form of plots of normalized ULS live load force[2] $\bar{F}_{ULS}$ versus normalized crack opening criterion D/D_{lim}, for three spans $L = 21.3\,\text{m}$ (70 ft), 30.5 m (100 ft), 36.6 m (120 ft). The starting point of the optimization iterations is the height H determined from the 1-D section design model, graphed in Figure 5-8 (a). From this figure, it is readily understood that the design formula overestimates the minimum height, as $D/D_{\text{lim}} < 1$ for $\bar{F}_{ULS} = 1$. The web height is then reduced in an iterative fashion, until $D/D_{\text{lim}} \simeq 1$ for $\bar{F}_{ULS} = 1$, which is the solution of the 2-D optimization procedure (Fig. 5-8 (b)). The results are summarized in Table 5.1. Figure 5-9 compares the results of the 2-D optimization procedure with those obtained with the 1-D section design model (Fig. 4-3, Table 4.3). The general trend is that the 1-D section design model, in the considered span range $L \in [21.3\,\text{m}\ (70\,\text{ft})\,;36.6\,\text{m}\ (120\,\text{ft})]$ and for the two prestress levels, overestimates the minimum height H, thus underestimating the moment capacity of the section. This most likely results from neglecting, in the 1-D model, the contribution of the web and the elastic stress gradient in the slab, which are taken into account in the more realistic 2-D finite element simulations. While the 2-D optimization results highlight the added value of refined analysis, the design formula provides safe lower bound values for the actual ULS flexural resistance. Thus, it is a suitable starting point for the engineering design of UHPC sections.

[2] Expressed in terms of the load combination (4.10), $\bar{F}_{ULS}$ represents:

$$F_{ULS} = 1.25 \times g_1 + 1.5 \times g_2 + \bar{F}_{ULS} \times 1.75\,(\delta \times p_1 + p_2)$$

Thus $\bar{F}_{ULS} \rightarrow 1$ corresponds to the design load level.

(a)

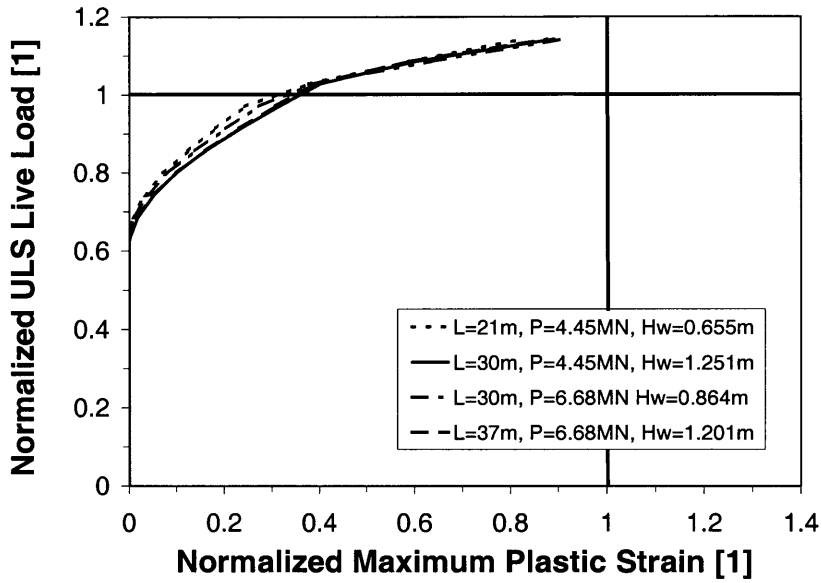

(b)

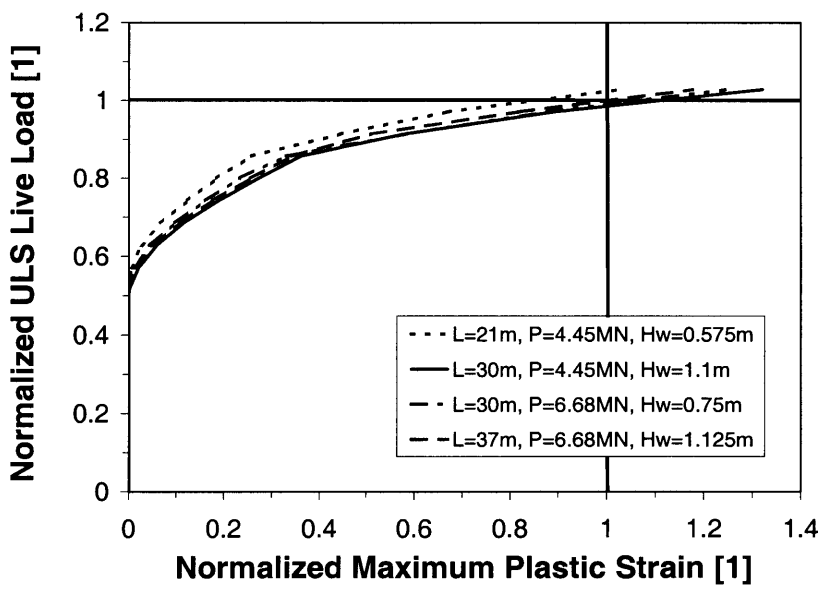

Figure 5-8: Model-based simulation results: Normalized ULS live load versus normalized plastic strain for: (a) Web height H_w from design formula (starting point of model-based optimization); (b) Optimized web height.

Span (L)	21.3 m (70 ft)	24.4 m (80 ft)	27.4 m (90 ft)	30.5 m (100 ft)	33.5 m (110 ft)	36.6 m (120 ft)
H_w for $P_{1,000} = 4.45$ MN	0.575 m (23 in)	0.725 m (29 in)	0.900 m (36 in)	1.100 m (44 in)	1.325 m (53 in)	
H_w for $P_{1,500} = 6.68$ MN			0.625 m (25 in)	0.750 m (30 in)	0.925 m (37 in)	1.125 m (45 in)

Table 5.1: Minimum web heights for single span UHPC girders.

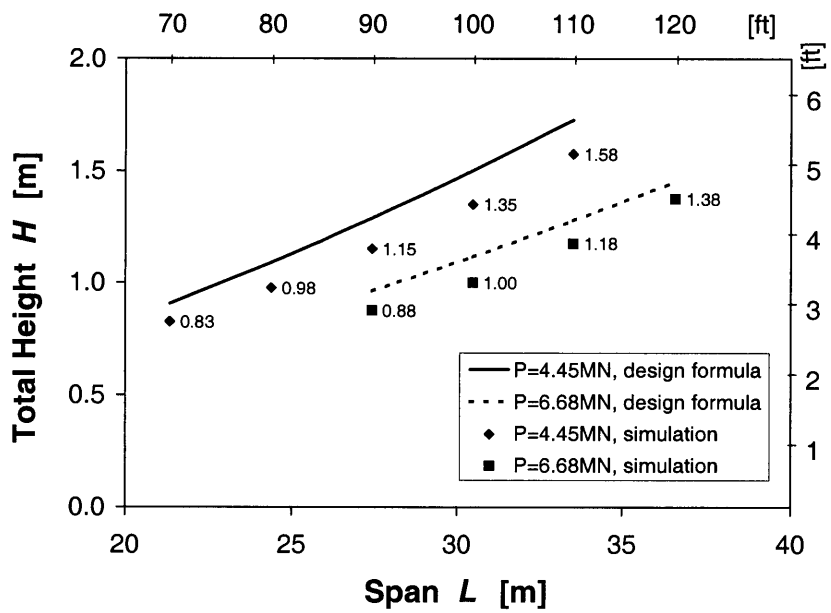

Figure 5-9: Results of 2-D optimization procedure: Minimum girder height $H = H_w + T_s + T_f$ versus span L. ($T_s = 0.10\,\text{m}\,(4\,\text{in})\,, T_f = 0.15\,\text{m}\,(6\,\text{in})$ were fixed values in the optimization procedure). For purpose of comparison, the figure also displays the results of the 1-D optimization procedure for two prestress force levels of $P_{1,000} = 4.45\,\text{MN}$ $(1,000\,\text{kips})$ and $P_{1,500} = 6.68\,\text{MN}$ $(1,500\,\text{kips})$ per traffic lane.

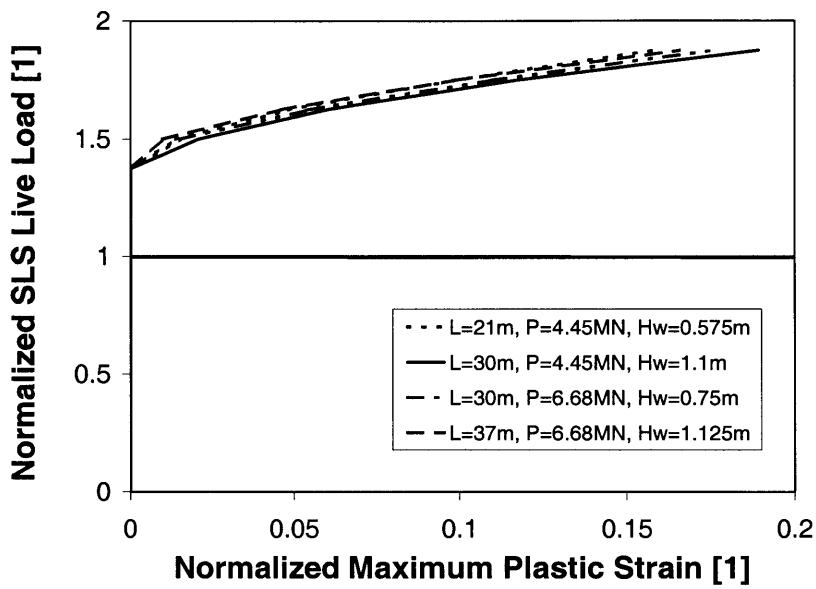

Figure 5-10: Model-based simulation results for optimized section heights: normalized SLS live load versus normalized plastic strain.

5.2.3 Design Control #1: Service Limit State

The optimized section height solution was checked with regard to the viability in the service limit state (SLS). The normalized load-crack opening curves of the SLS for three spans $L = 21.3\,\mathrm{m}$ (70 ft), 30.5 m (100 ft), 36.6 m (120 ft) are plotted in Figure 5-10, in which $\bar{F}_{SLS}$ stands for the normalized service live load[3], and D/D_{lim} for the crack opening normalized, for pure reasons of dimensional consistency, by the ULS crack opening criterion (5.4). We verify that the 'no cracking' criterion (4.18) is achieved, as $D/D_{\mathrm{lim}} = 0$ for $\bar{F}_{SLS} = 1$. That is, the optimal web height suggested by the ULS also satisfies the SLS conditions.

Finally, note that the rotation of the girder at the supports is very small: for a $L = 30.5\,\mathrm{m}$ (100 ft) girder, the support rotation was $\phi \approx 0.003\,\mathrm{rad} = 0.2\,^\circ$ at SLS, and $\phi \approx 0.02\,\mathrm{rad} = 1\,^\circ$

[3]Recall that $D_{\mathrm{lim}}^{SLS} \equiv 0$. The normalized service live load is defined in (4.9) by:

$$F_{SLS} = 1.0 \times (g_1 + g_2) + \bar{F}_{SLS} \times 0.8\,(\delta \times p_1 + p_2)$$

at ULS.

5.2.4 Design Control #2: Shear Resistance

The optimized section height solution was also examined with regard to shear resistance. For constructibility reasons, we assumed a minimum web width of $T_w = 0.05\,\mathrm{m}$ (2 in), which gives a total web width per lane of $3 \times T_w = 0.15\,\mathrm{m}$ (6 in) in the 2-D simulations. (see Figure 5-5 (b)). The loading scheme for shear resistance is illustrated in Figure 5-6 (b), in which the design truck load is shifted to position the rear axle at a distance $h/2$ from the support causing the maximum shear force. In the finite element simulations, the tendon effect on strength and stiffness were not considered and the entire structure was modeled as an 'UHPC Only' structure (for details, see Section 3.3). Even under these lower bound conditions, it was found that the structural performance was not limited by shear in the web, but by the flexural resistance in the bottom flange for all the spans considered. Furthermore, the shear load resistance was roughly twice the flexural design load. That is, for the studied cross sections, spans, and load cases, shear failure is not an issue since bending will always dominate in both the service limit state and the ultimate strength limit state.

5.2.5 Design Remark

The employed minimum bottom flange section $A_f = 3B_f \times T_f$ was based on its ability to host the prestress tendons (5.1). It could be argued that a larger bottom flange could contribute more to the load bearing capacity through the ductile yield strength UHPC realizes after cracking. It is instructive to examine this presumption through the design formula (4.5), which can be

combined with (3.5) to achieve:[4]

$$\frac{M_u^{load}}{f_y^T A_f H'} \leq \rho + c_T (1 - \rho) \tag{5.6}$$

where $\rho = \Sigma_y / f_y^T$ is the UHPC-to-tendon strength ratio ($\rho = 1/162$ for DUCTAL^{TM}). From (5.6), it is readily understood that the most efficient way of increasing the moment capacity is achieved by increasing the tendon concentration c_T (which, with all other parameters constant, is equivalent to increasing the prestress force), the effective height H' or the UHPC-to-tendon strength ratio $\rho = \Sigma_y / f_y^T$. It is clearly less efficient to use the bottom flange section, since an increase of A_f reduces simultaneously the prestress concentration c_T. For typical values of UHPC, relation (5.6) reveals that an increase in load bearing capacity by increasing the bottom flange section is marginal ($\propto 1 + \rho (n - 1)$, where n stands for the section increase). This validates our choice of a minimum bottom flange section defined by relation (5.1).

5.3 3-D Optimization: Minimum UHPC Slab Thickness

Finite element simulations were performed to determine possible 3-D failure mechanisms on the UHPC bridge girder system, especially those which may occur in the slab. The slab system resists the wearing surface load and traffic loads (HL-93 load, which is design truck HS-20 + distributed lane load as discussed in Section 4.3.4) through a combination of transverse and longitudinal bending and shear. In addition to the 2-D slab design parameters, two additional 3-D slab design parameters may be of importance:

- The design truck location which delivers the maximum transversal moment (see Figs. 5-11 (a) and (b)): for a web spacing $B' = B_g - 2B_f$ smaller than or equal to the transversal

[4] By using the invariants $\bar{m}_u$ and $\bar{p}$, which are described by:

$$\bar{m}_u = \frac{M_u^{load}}{\Sigma_y^B A_f L} = \frac{M_u^{load}}{f_y^T A_f L (\rho + c_T (1 - \gamma - \rho))}$$

$$\bar{p} = \frac{P}{\Sigma_y^B A_f} = \frac{\gamma c_T}{\rho + c_T (1 - \gamma - \rho)}$$

in the design formula:

$$\bar{m}_u \leq (1 + \bar{p}) \frac{H'}{L}$$

one obtains Eq. (5.6).

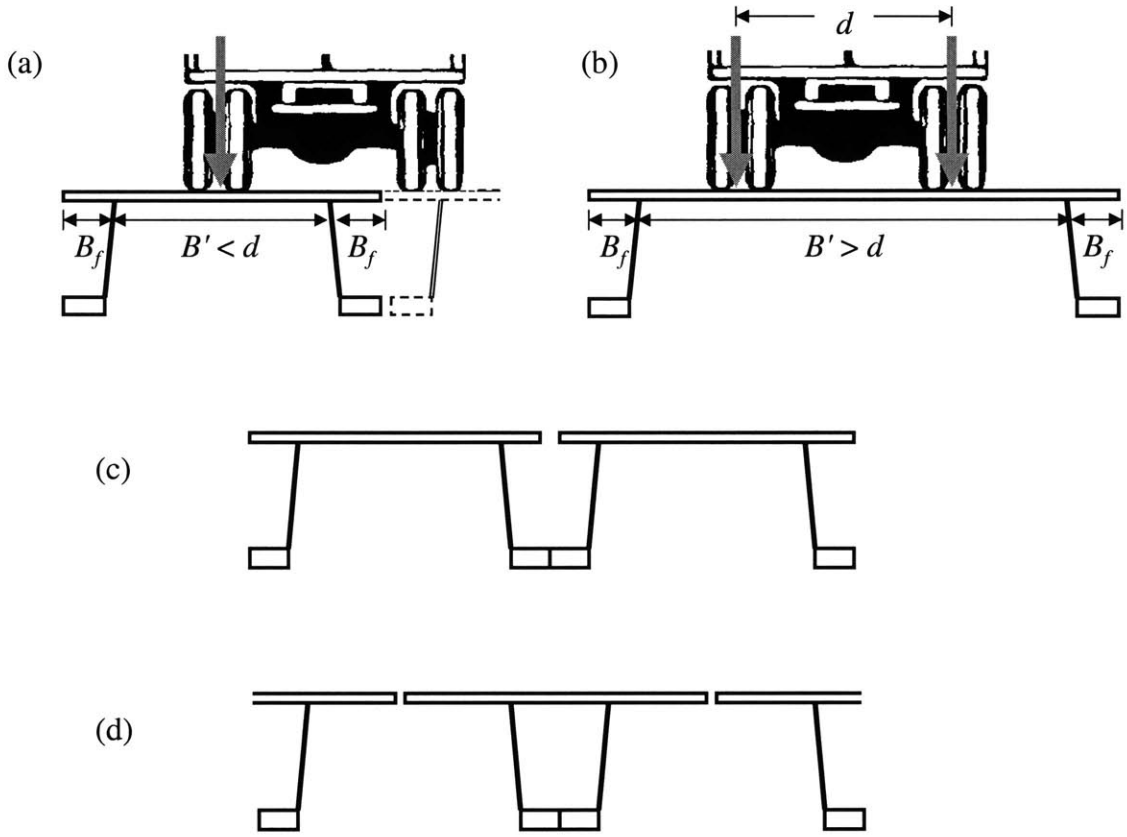

Figure 5-11: Design parameters for slab thickness optimization: (a-b) Design truck location; (c-d) Slab joint location.

axle distance $d = 1.8\,\mathrm{m}$ (6 ft) (see Fig. 4-3), one centered wheel load can be considered the characteristic loading case; for $B' > d$, one may assume two centered wheel loads. From a straightforward estimate of the transverse bending moments in the slab for these two cases, the most severe load case is the one for which $B' = d$, which corresponds to 1.5 girders per traffic lane[5]. Since this case is the most severe loading configuration, it is the one we consider here.

- The location of the longitudinal slab joint (see Figs. 5-11 (c) and (d)): the slab joint represents a 'stress free boundary' (no moment, no axial or shear force transmission) and can be placed in either the girder axis (Fig. 5-11 (c)) or slab mid-span axis (Fig. 5-11 (d)). The first case is considered here, and the effect of changing the location of the joint is studied further in Section 5.3.4.

Finally, the 3-D finite element simulations are used to investigate local cracking effects that may occur in the bridge girder system during transfer of prestressing, particularly at the web-flange interfaces at the ends of the girder.

---

[5] Neglecting slab effects, the maximum bending moment for $B' = d = 1.8\,\mathrm{m}\,(6\,\mathrm{ft})$, corresponding to 1.5 girders per traffic lane, occurs in slab mid span (Fig. 5-11 (a)):

$$\begin{aligned} M_{SLS}\left(B' = d\right) &= \left(1.0\left(g_1 T_s + g_2\right) + 0.8 p_2\right) 1_x \left(\frac{d^2}{8} - \frac{\left(B_f\right)^2}{2}\right) + 0.8\delta \frac{P_{w2}}{4} d \\ M_{ULS}\left(B' = d\right) &= \left(1.25 g_1 T_s + 1.5 g_2 + 1.75 p_2\right) 1_x \left(\frac{d^2}{8} - \frac{\left(B_f\right)^2}{2}\right) + 1.75\delta \frac{P_{w2}}{4} d \end{aligned}$$

and for $B' = 1.5d$ which corresponds to 1 girder per traffic lane (Fig. 5-11 (b)):

$$\begin{aligned} M_{SLS}\left(B' = 1.5d\right) &= \left(1.0\left(g_1 + g_2\right) + 0.8 p_2\right) 1_x \left(\frac{(1.5d)^2}{8} - \frac{(1.5B_f)^2}{2}\right) + 0.8\delta \frac{P_{w2}}{2}\frac{d}{2} \\ M_{ULS}\left(B' = 1.5d\right) &= \left(1.25 g_1 T_s + 1.5 g_2 + 1.75 p_2\right) 1_x \left(\frac{(1.5d)^2}{8} - \frac{(1.5B_f)^2}{2}\right) + 1.75\delta \frac{P_{w2}}{2}\frac{d}{2} \end{aligned}$$

where $P_{w2} = 71.2\,\mathrm{kN}$ (16 kips) is the maximum HS-20 wheel load and 1_x is a unit length of slab in the longitudinal direction. With the values from Table 4.2, we determine for a slab thickness of $T_s = 0.10\,\mathrm{m}$ (4 in):

$$\begin{aligned} M_{SLS}\left(B' = d\right) &= 36.2\,\mathrm{kN\,m}\ (26.7\ \text{kips ft}) > M_{SLS}\left(B' = 1.5d\right) = 27.4\,\mathrm{kN\,m}\ (20.2\ \text{kips ft}) \\ M_{ULS}\left(B' = d\right) &= 78.0\,\mathrm{kN\,m}\ (57.5\ \text{kips ft}) > M_{ULS}\left(B' = 1.5d\right) = 57.3\,\mathrm{kN\,m}\ (42.3\ \text{kips ft}) \end{aligned}$$

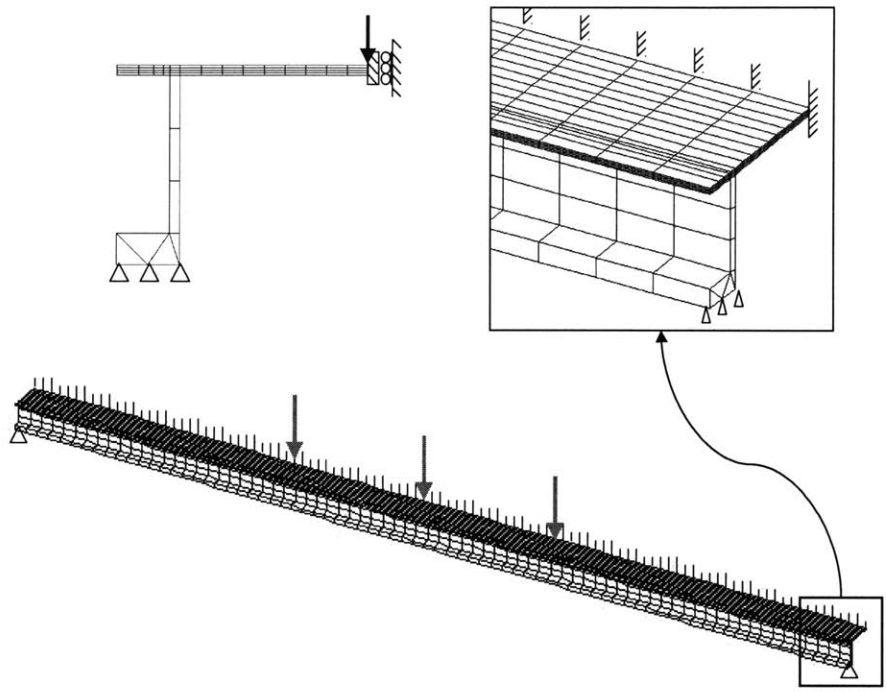

Figure 5-12: Employed mesh for the the slab thickness optimization: Section and 3-D view of 3D-30H-5S girder (in Table 5.2) mesh, with the location of HS-20 truck load and the boundary conditions.

5.3.1 3-D Section Modeling

In the finite element simulations, the girders are modeled in 3-D with solid finite elements for three girder lengths, $L = 21.3\,\mathrm{m}$ (70 ft), $30.5\,\mathrm{m}$ (100 ft), $36.6\,\mathrm{m}$ (120 ft). A typical FE mesh is graphed in Figure 5-12. Only single π-sections, corresponding to 2/3 of a traffic lane, are modeled, which, along with symmetry conditions, allow us to employ a reduced half-section model. The meshes are comprised primary of 8-noded cube elements with some 6-noded trigonal prism elements. The slab thickness is discretized into four elements to appropriately represent stress and strain gradients in the slab. The web and the bottom flange are coarsely meshed. Indeed, they are only modeled in order to capture the overall beam response of the girders.

The section parameters that are fixed in the 3-D simulations are the slab width ($B_g = 2.44\,\mathrm{m}$ (8 ft)), the bottom flange dimensions ($B_f = 0.30\,\mathrm{m}$ (12 in), $T_f = 0.15\,\mathrm{m}$ (6 in)), and the web dimensions. The web thickness is set at $T_w = 0.05\,\mathrm{m}$ (2 in), and the web height H_w is taken

Mesh Name	L	B_g	T_s	H_w	T_w	B_f	T_f
3D-21L-5S	21.3 m	2.44 m	0.05 m (2 in)	0.575 m	0.05 m	0.30 m	0.15 m
3D-21L-7.5S	(70 ft)	(8 ft)	0.075 m (3 in)	(23 in)	(2 in)	(12 in)	(6 in)
3D-21L-10S			0.10 m (4 in)				
3D-30L-5S	30.5 m	2.44 m	0.05 m (2 in)	1.10 m	0.05 m	0.30 m	0.15 m
3D-30L-7.5S	(100 ft)	(8 ft)	0.075 m (3 in)	(44 in)	(2 in)	(12 in)	(6 in)
3D-30L-10S			0.10 m (4 in)				
3D-30H-5S	30.5 m	2.44 m	0.05 m (2 in)	0.75 m	0.05 m	0.30 m	0.15 m
3D-30H-7.5S	(100 ft)	(8 ft)	0.075 m (3 in)	(30 in)	(2 in)	(12 in)	(6 in)
3D-30H-10S			0.10 m (4 in)				
3D-36H-5S	36.6 m	2.44 m	0.05 m (2 in)	1.125 m	0.05 m	0.30 m	0.15 m
3D-36H-7.5S	(120 ft)	(8 ft)	0.075 m (3 in)	(45 in)	(2 in)	(12 in)	(6 in)
3D-36H-10S			0.10 m (4 in)				

Table 5.2: List of meshes for 3D analysis of the slabs. The "L" and "H" in the mesh name stand for the low (4.45 MN (1,000 kips)) and the high level (6.68 MN (1,500 kips)) of prestressing.

from the 2-D optimization results (Table 5.1). The only free parameter in the simulations, therefore, is the slab thickness T_s. For each girder length, three slab thicknesses were considered, T_s = 0.05 m (2 in), 0.075 m (3 in), 0.10 m (4 in). Table 5.2 summarizes the considered sets of section parameters employed in the finite element simulations.

Because of the loading chronology (Fig. 5-4), two separate sets of simulations were performed -one for the service limit state (4.9), and the other for the ultimate strength limit state (4.10). After application of the factored dead loads, the live loads were gradually applied until the required load resistance levels were reached, i.e. $F/F_{SLS} = 1$ or $F/F_{ULS} = 1$, or until the crack opening criteria were violated.

5.3.2 3-D ULS Design

The slab thickness was optimized according to the ULS optimization criterion (4.15) and (4.17), which reduces here to:

$$\left\{ \begin{array}{c} \bar{F}_{ULS} = \dfrac{F}{F_{ULS}} = 1 \\ \dfrac{D}{D_{\text{lim}}} = \mathcal{F}\left(\bar{F}_{ULS}, \dfrac{T_s}{L}\right) \rightarrow 1 \end{array} \right\} \tag{5.7}$$

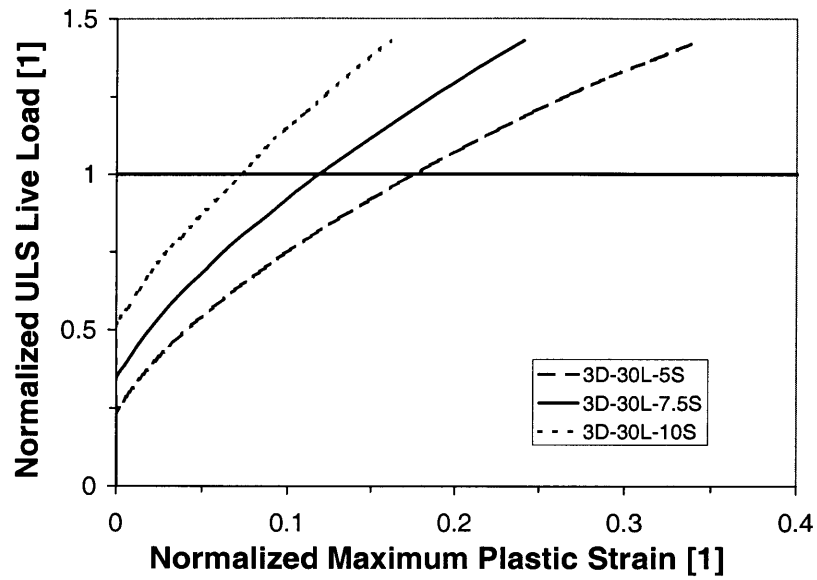

Figure 5-13: Model-based simulation results for 3D-30L girders: Normalized ULS live load versus normalized plastic strain for three slab thicknesses $T_s = 0.05\,\mathrm{m}$ (2 in), 0.075 m (3 in), 0.10 m (4 in). The admissible ULS plastic strains according to (5.8) decrease with increasing T_s: $D_{\mathrm{lim}} = 1/110...1/170...1/220$.

where D_{lim} is the the maximum admissible plastic strain for unreinforced UHPC sections, which according to (4.13) depends on the slab thickness:

$$D = \max\left\{\varepsilon^{p}_{M,I}(\mathbf{x})\right\} \leq D_{\mathrm{lim}} \equiv \varepsilon^{p,un}_{\mathrm{lim}} = 1.5\frac{[[w]]^{un}_{\mathrm{lim}}}{T_s} \tag{5.8}$$

where $[[w]]^{un}_{\mathrm{lim}} = 0.3\,\mathrm{mm}$ (1/85 in) and T_s is the slab thickness.

The effect of the slab thickness on the ULS-performance of the girder is elucidated with Figure 5-13, which plots the normalized ULS live load $\bar{F}_{ULS}$ versus the normalized composite matrix plastic strain D/D_{lim} for the girder of span $L = 30.5\,\mathrm{m}$ (100 ft). Similar curves were obtained for other spans. The main conclusion to be drawn from these results is that even a small slab thickness of $T_s = 0.05\,\mathrm{m}$ (2 in) is more than sufficient for the ultimate load resistance, as $D/D_{\mathrm{lim}} < 1$ for $\bar{F}_{ULS} = 1$.

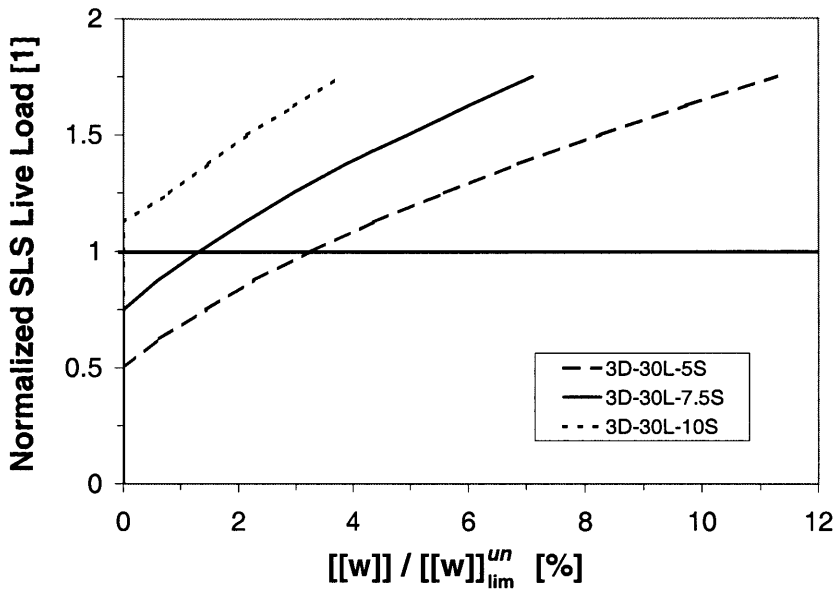

Figure 5-14: Model-based simulation results for 3D-30L girders: Normalized SLS live load versus cumulative crack opening for three slab thickness $T_s = 0.05\,\mathrm{m}$ (2 in), $0.075\,\mathrm{m}$ (3 in), $0.10\,\mathrm{m}$ (4 in).

5.3.3 3-D SLS Design and Appraisal of the 'No Cracking' Criterion

In contrast to the ULS, the 'no cracking' criterion set (4.18) for the SLS becomes a significant design consideration. As an example, for the $L = 30.5\,\mathrm{m}$ (100 ft) girders, Figure 5-14 displays the normalized SLS live load $\bar{F}_{SLS}$ versus the cumulative maximum crack opening $[[w]]$ that we estimate, by analogy with (5.8), from the plastic strain obtained by model-based simulations:

$$[[w]] = \frac{2}{3} T_s \max\left\{\varepsilon^p_{M,I}(\mathbf{x})\right\} \tag{5.9}$$

For dimensional reasons, this crack opening is normalized by the ULS limit crack opening $[[w]]^{un}_{\mathrm{lim}} = 0.3\,\mathrm{mm}$ (1/85 in). It is notable from this figure that slab thicknesses smaller than $T_s = 0.10\,\mathrm{m}$ (4 in) violate the 'no cracking' SLS design criterion. Figure 5-15 recasts these results, for all girder configurations of Table 5.2, in form of a plot of the normalized live load $\bar{F}_{SLS}$ at which first cracking was observed in the simulations. First cracking was observed at the same normalized live load level for a given slab thickness irrespective of the span, prestressing,

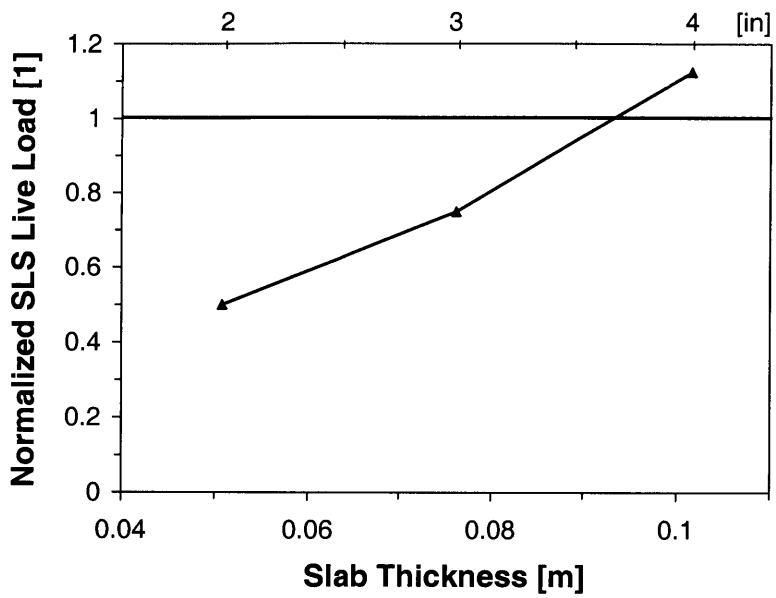

Figure 5-15: Slab thickness versus normalized SLS live load at which the first cracking occurs in the simulations.

girder height, etc. While this result may be a consequence of the large increments of load application (by steps of 10% of the nominal live load), it is still clear from the SLS analysis that a 'no cracking' SLS criterion requires a minimum slab thickness of:

$$T_s \geq \min T_s^{SLS} = 0.10\,\mathrm{m}\,(4\,\mathrm{in}) \tag{5.10}$$

Remarks:

1. It could be argued that the 'no cracking' criterion is a too severe a criterion for the SLS of UHPC, given the ductile tensile behavior of UHPC after first cracking. Indeed, on a material level, the ratio of total yield strength ($\Sigma_y = k_M + f_y$) to first cracking strength ($\Sigma_t = k_M + f_t$) for UHPC is typically on the order of (values for DUCTAL^{TM}, Table 2.1):

$$R = \frac{k_M + f_y}{k_M + f_t} = 1.5 \tag{5.11}$$

Given the low scattering of UHPC tensile properties, it could be appropriate to permit,

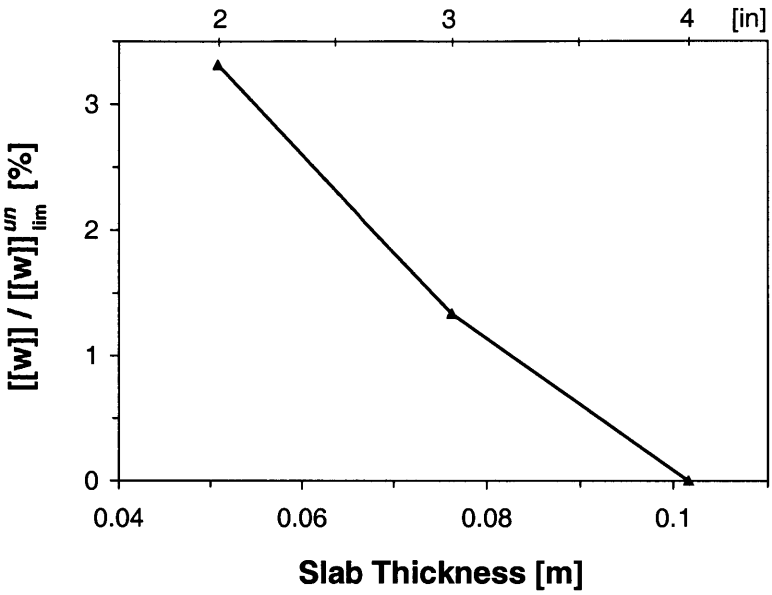

Figure 5-16: Normalized crack width at the SLS design load (normalized by the ULS limit crack opening of $[[w]]^{un}_{\text{lim}} = 0.3\,\text{mm}\,(\frac{1}{85}\,\text{in})$) versus slab thickness.

on a structural level, some crack opening in the SLS. Figure 5-16 displays the normalized cumulative crack opening $[[w]]$ realized by the girders with different slab thicknesses at the SLS load $\bar{F}_{SLS} \equiv 1$. The crack opening $[[w]]$ in this figure was determined from (5.9), then normalized by the ULS limit crack opening $[[w]]^{un}_{\text{lim}}$. The insignificant values of the maximum crack opening realized with smaller slab thicknesses at the SLS load level (roughly 3.5% of $[[w]]^{un}_{\text{lim}}$ for $T_s = 0.05\,\text{m}$ (2 in) and 1.5% for $T_s = 0.075\,\text{m}$ (3 in)) suggest that a small relaxation in the SLS criterion would reduce the minimum required slab thickness substantially. Furthermore, a relaxed SLS crack opening criterion could maintain the fatigue resistance of UHPC structures.

2. A second argument in favor of permitting some crack opening in the service limit state relates to the nature and location of the cracking in the slab. Figures 5-17 and 5-18 display for a slab of thickness $T_s = 0.05\,\text{m}$ (2 in), the plastic strain distribution and the direction of principal plastic strain at SLS and ULS. It is clearly shown in these figures, that the plastic strains are extremely localized under the HS-20 truck wheel loads, p_1^2

and p_1^3 in particular, shown with thicker arrows. From Figure 5-17, we can identify three main sources of cracking: cracking due to the transversal and the longitudinal moment of the slab and the plastic strain from the punching shear at the circumference of the plastic zone. As the load increases the flexural cracks become dominant but the plastic strains are still very localized, and what is more notable, do not propagate to the top surface of the slab even with $T_s = 0.05\,\mathrm{m}$ (2 in) and at ULS (see Fig. 5-18). Since one of the purposes of the SLS 'no cracking' criterion is to reduce the harmful exposure of structural elements to aggressive (corroding) agents, penetrating typically through cracks at the top surface into the structural bulk, it could be argued that these cracks would not be detrimental to the overall durability performance of the slab.

3. A final argument in favor of a thinner slab relates to the overall structural performance. Figure 5-19 displays 2-D simulation results in form of the normalized ULS live load - crack opening curves for a $L = 30.5\,\mathrm{m}$ (100 ft) girder with different slab thicknesses, $T_s = 0.10\,\mathrm{m}$ (4 in) and $T_s = 0.15$ m (6 in). All other dimensions and parameters kept constant (corresponding to the optimized height for a total prestress of $P_{1,000} = 4.45\,\mathrm{MN}$ (1,000 kips) per traffic lane), the results indicate an increase of the slab thickness does not improve the overall structural performance as an increase in self weight of the girder reduces live load carrying capacity.

5.3.4 Design Control #1: Slab Joint Position

Up to this point, we assumed that the slab joint was placed in the girder axis (Fig. 5-11 (c)) for all of the finite element simulations. Neglecting web effects, the maximum bending moment for $B' = d = 1.8\,\mathrm{m}$ (6 ft), which corresponds to 1.5 girders per traffic lane, occurs in the slab mid span:

$$M_{SLS}^{SLAB} = (1.0\,(g_1 T_s + g_2) + 0.8 p_2)\, 1_x \left(\frac{B'^2}{8} - \frac{B_f^2}{2} \right) + 0.8\delta \frac{P_{w2}}{4} B' \tag{5.12}$$

$$M_{ULS}^{SLAB} = (1.25 g_1 T_s + 1.5 g_2 + 1.75 p_2)\, 1_x \left(\frac{B'^2}{8} - \frac{B_f^2}{2} \right) + 1.75\delta \frac{P_{w2}}{4} B' \tag{5.13}$$

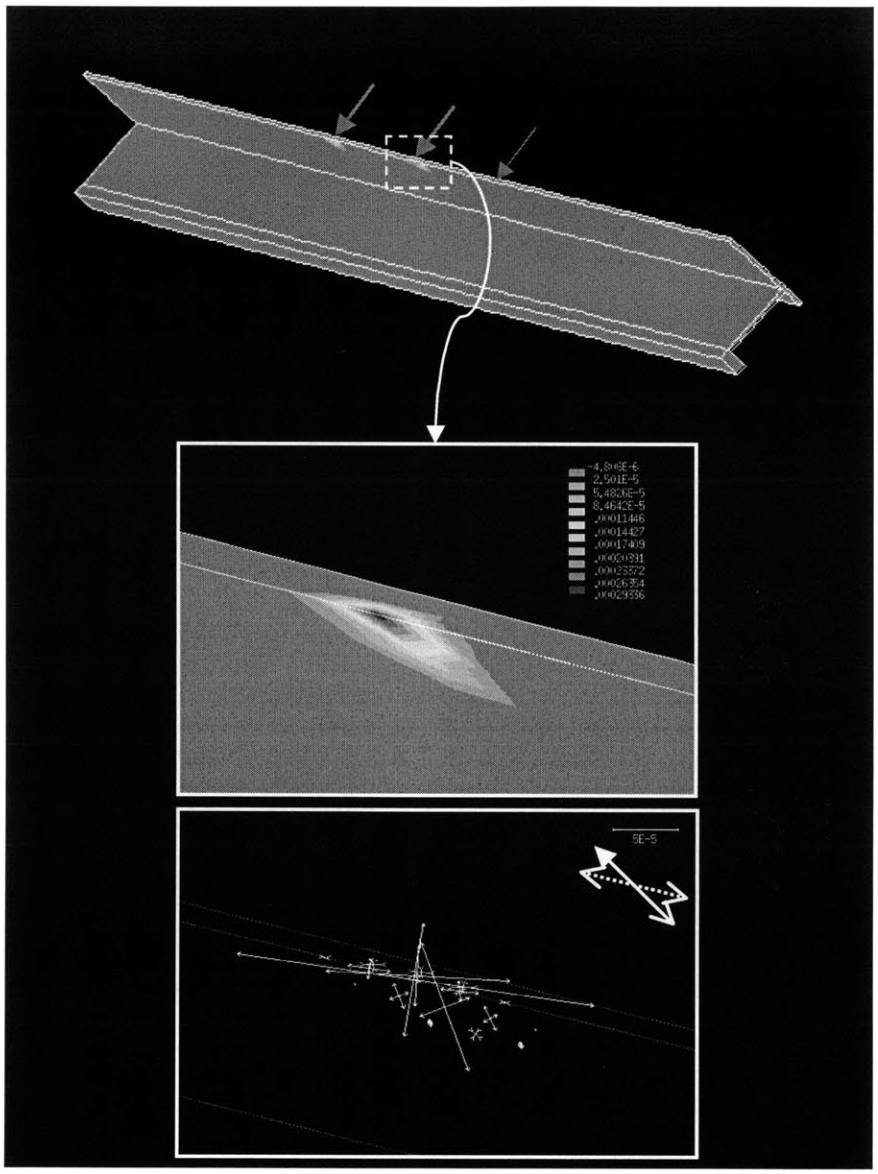

Figure 5-17: Plastic strains of 3D-30L-5S girder slab at SLS. Top: the plastic strain distribution. Bottom: the direction of principal plastic strains. The mesh is tilted to show the cracking at the bottom of the slab. A dashed and a solid arrow is given as references for the longitudinal and transversal direction of the girder, respectively.

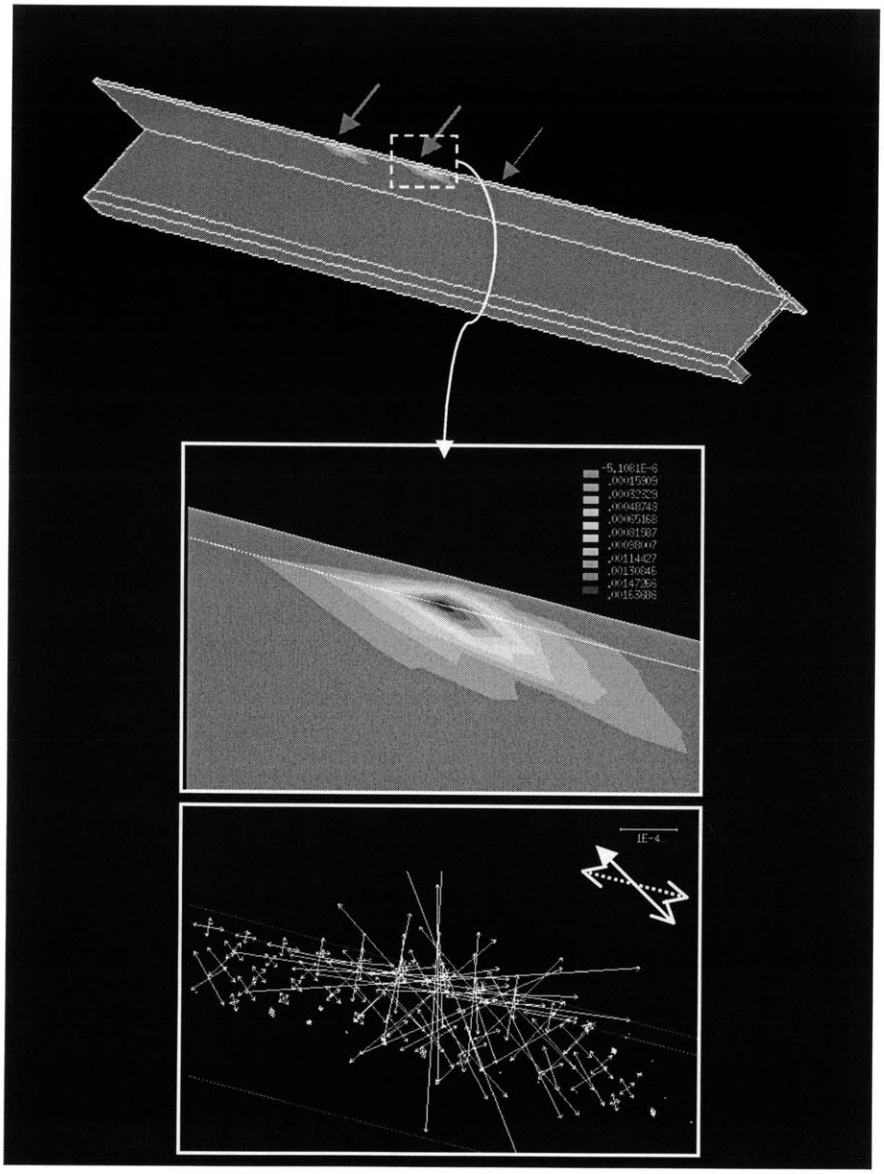

Figure 5-18: Plastic strains of 3D-30L-5S girder slab at ULS. Top: the plastic strain distribution. Bottom: the direction of principal plastic strains. The mesh is tilted to show the cracking at the bottom of the slab. A dashed and a solid arrow is given as references for the longitudinal and transversal direction of the girder, respectively.

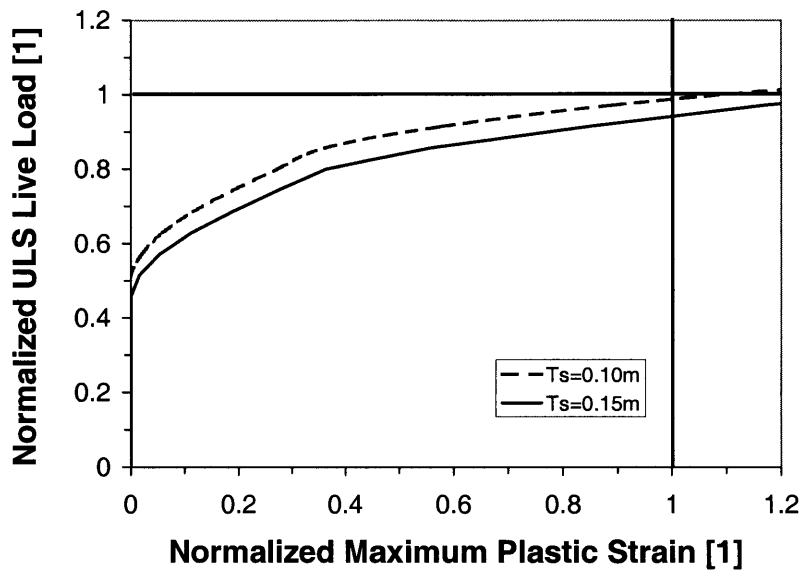

Figure 5-19: 2-D Model-based simulation results for girders of span $L = 30.5\,\mathrm{m}$ (100 ft): Normalized ULS live load versus normalized plastic strain for two slab thickness $T_s = 0.10\,\mathrm{m}$ (4 in) and $0.15\,\mathrm{m}$ (6 in). Effect of the increase in slab thickness on the overall structural performance.

where $P_{w2} = 71.2\,\mathrm{kN}$ (16 kips) is the maximum HS-20 wheel load and 1_x represents a unit length of slab in longitudinal direction. By contrast, when the slab joint is placed in the slab midspan (Fig. 5-11 (d)), the maximum (negative) moment occurs over the web:

$$M_{SLS}^{WEB} = -\left(1.0\left(g_1 T_s + g_2\right) + 0.8 p_2\right) 1_x \frac{B'^2}{2} - 0.8\delta \frac{P_{w2}}{4} B' \tag{5.14}$$

$$M_{ULS}^{WEB} = -\left(1.25 g_1 T_s + 1.5 g_2 + 1.75 p_2\right) 1_x \frac{B'^2}{2} - 1.75\delta \frac{P_{w2}}{4} B' \tag{5.15}$$

From the previous relations, it is readily understood that a slab joint in the slab mid span axis delivers higher nominal values of the transversal moment. For example, for a slab thickness of $T_s = 0.10\,\mathrm{m}$ (4 in), a web distance of $B' = 1.8\,\mathrm{m}$ (6 ft), and the values from Table 4.2:

$$M_{SLS}^{SLAB} = 36.2\,\mathrm{kN\,m}\ (26.7\ \text{kips ft}) < \left|M_{SLS}^{WEB}\right| = 43.4\,\mathrm{kN\,m}\ (32.0\ \text{kips ft}) \tag{5.16}$$

$$M_{ULS}^{SLAB} = 78.0\,\mathrm{kN\,m}\,(57.5\ \text{kips ft}) < \left|M_{ULS}^{WEB}\right| = 89.8\,\mathrm{kN\,m}\ (66.2\ \text{kips ft}) \tag{5.17}$$

Though these analytical results show that the transversal moment would be larger with a

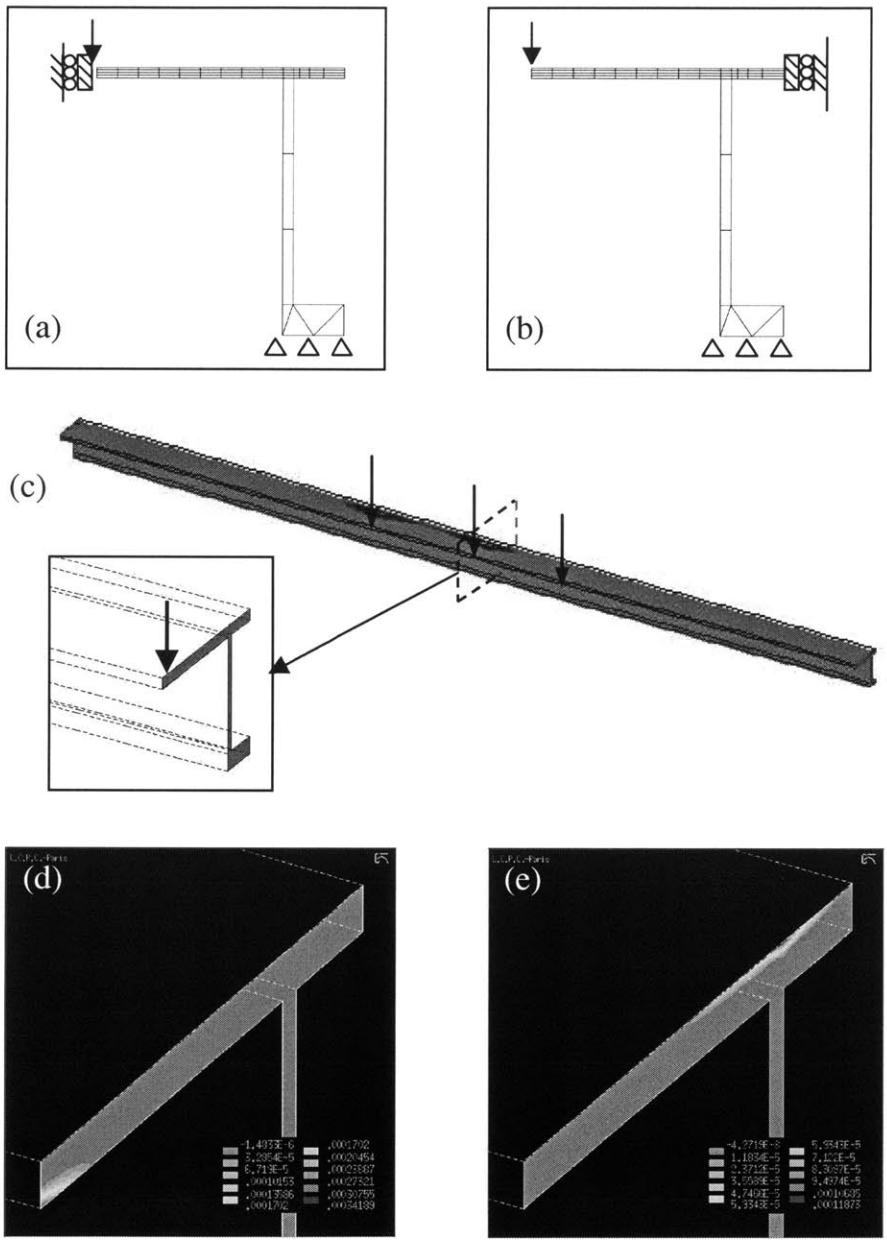

Figure 5-20: 3-D Model-based investigation of the effect of the slab joint position: (a-b) Section models with load and boundary conditions; (c) 3D–view of mesh with joint in slab mid span, showing the location of HS-20 truck loads; (d-e) Plastic strain distribution under the truck wheel load.

joint at the slab mid span, it turns out that this location of joint is more beneficial in controlling the overall plastic strain of the slab. Figure 5-20 displays, for the two slab joint locations, the section models with load and boundary conditions (Figs. 5-20 (a) and (b)) employed in 3-D finite element simulations. As expected, the maximum plastic strains occur over the web in the case of a joint placed in the slab mid span axis (Figs 5-20 (b), (c) and (e)), while for the other case the maximum plastic strain occurs in a very localized manner at the slab's bottom surface, as previously shown in Figures 5-17 and 5-18. Figures 5-20 (d) and (e) show the plastic strain distribution in the transversal section of the girder ($T_s = 0.10\,\mathrm{m}$ (4 in), $L = 30.5\,\mathrm{m}$ (100 ft); other dimensions from mesh 3D-30L-10S in Table 5.2), cut at the plane where the concentrated wheel load p_1^2 is applied (Fig. 5-20 (c)).

Figures 5-21 and 5-22 further illustrate the plastic strain evolution related to the joint locations for both SLS and the ULS using three different slab thicknesses -$T_s = 0.05\,\mathrm{m}$ (2 in), $T_s = 0.075\,\mathrm{m}$ (3 in) and $T_s = 0.10\,\mathrm{m}$ (4 in):

- In Figure 5-21, the normalized SLS live load is plotted against the normalized crack opening $[[w]]/[[w]]^{un}_{\mathrm{lim}}$ for slab thicknesses of $T_s = 0.05\,\mathrm{m}$ (2 in) and $T_s = 0.075\,\mathrm{m}$ (3 in) ($L = 30.5\,\mathrm{m}$ (100 ft), other dimensions from mesh 3D-30L-5S and 3D-30L-7.5S in Tab. 5.2). For $T_s = 0.05\,\mathrm{m}$ (2 in) (5-21 (a)), the SLS 'no cracking' criterion is breached at the same load level for both slab joint positions. In turn, for $T_s = 0.075\,\mathrm{m}$ (3 in) (5-21 (b)), the SLS live load at cracking is roughly 30% higher for a joint in mid span.

- In Figure 5-22, the normalized ULS live load is plotted against the normalized crack opening $[[w]]/[[w]]^{un}_{\mathrm{lim}}$ for a slab thickness of $T_s = 0.10\,\mathrm{m}$ (4 in) ($L = 30.5\,\mathrm{m}$ (100 ft), other dimensions from mesh 3D-30L-10S in Tab. 5.2). For the mid span slab joint location, the crack opening at ULS load level ($\bar{F}_{ULS} = 1$) is only 35% of the crack opening obtained for the reference solution (slab joint placed in girder axis).

In summary, a slab joint placed in slab mid span may be a viable design solution, as we find an improved performance at SLS and ULS despite the higher transversal moment. However, cracks in this solution will occur at the top surface of the slab making it less attractive with regard to the durability performance of the UHPC slab system.

(a)

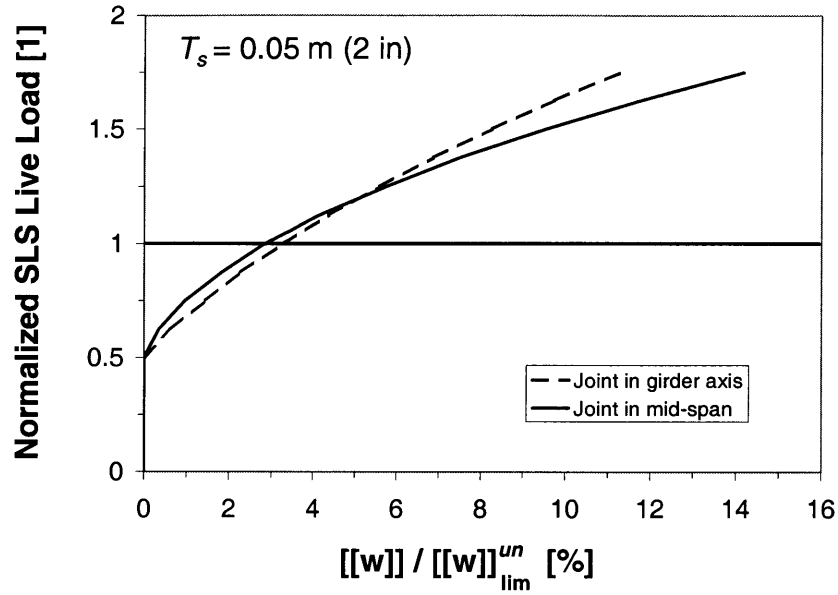

(b)

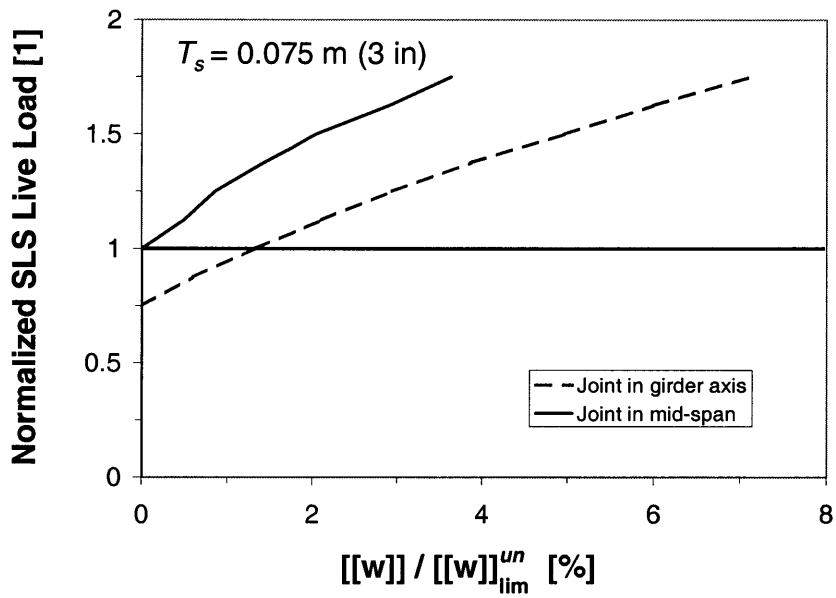

Figure 5-21: Normalized service live load versus normalized crack opening for: (a) $T_s = 0.05\,\mathrm{m}$ (2 in) and (b) $T_s = 0.075\,\mathrm{m}$ (3 in).

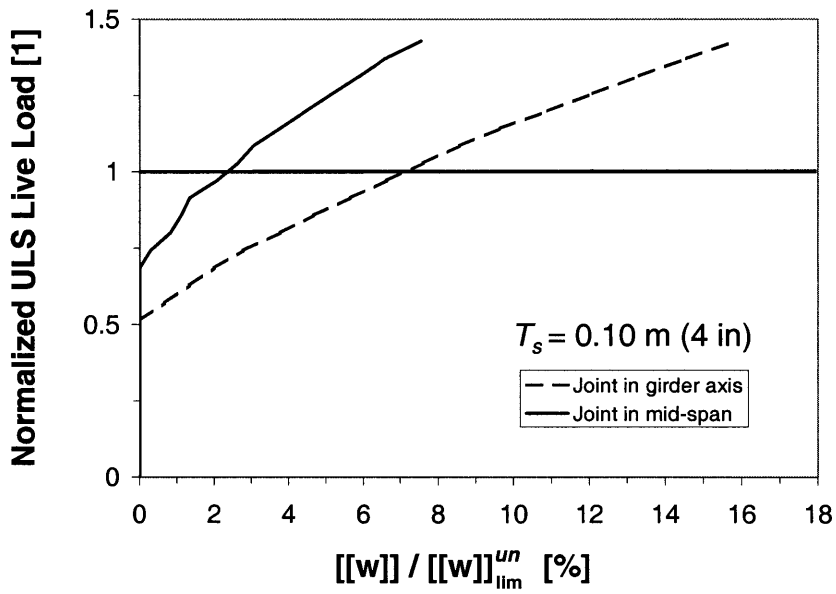

Figure 5-22: Normalized ultimate live load versus normalized crack opening, for $T_s = 0.10\,\mathrm{m}$ (4 in).

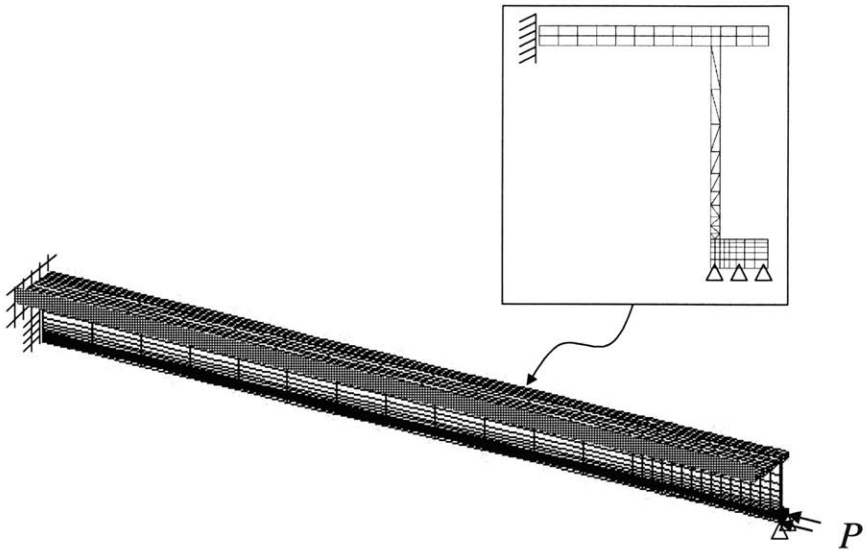

Figure 5-23: 3-D model-based investigation of transfer of prestressing: employed mesh with boundary conditions.

5.3.5 Design Control #2: Transfer of Prestressing

A detailed 3-D analysis was performed to assess the risk of cracking due to high stresses induced during the transfer of prestressing to the structure. The mesh employed in the analysis is depicted in Figure 5-23. Using the girder symmetry, only a quarter of the girder was modeled and zero normal displacement boundary conditions were prescribed in the planes of symmetry. The mesh was refined in the bottom flange and close to the ends where the prestress force is applied. The girder self weight g_1 and the prestressing force P were applied simultaneously, mimicking the pre-tensioning and self weight activation (see Section 5.1.3).

Figure 5-24 displays the plastic strains obtained in the simulation. They are confined in a localized zone at the bottom flange-web interface, and extend over a distance of $H_w/2$. The magnitude of the plastic strains is non negligible, $\max_{\underline{x}}\left(\varepsilon^p_{M,I}\right) = 5.8 \times 10^{-4}$, which translates into an estimated cumulative crack opening at the bottom flange-web interface (from Eq. (4.13)):

$$\max\left[[w]\right] = \frac{2}{3}\max_{\underline{x}}\left(\varepsilon^p_{M,I}\right)\max\left(T_w, T_f\right) = 0.06\,\mathrm{mm}(1/430\,\mathrm{in}) \tag{5.18}$$

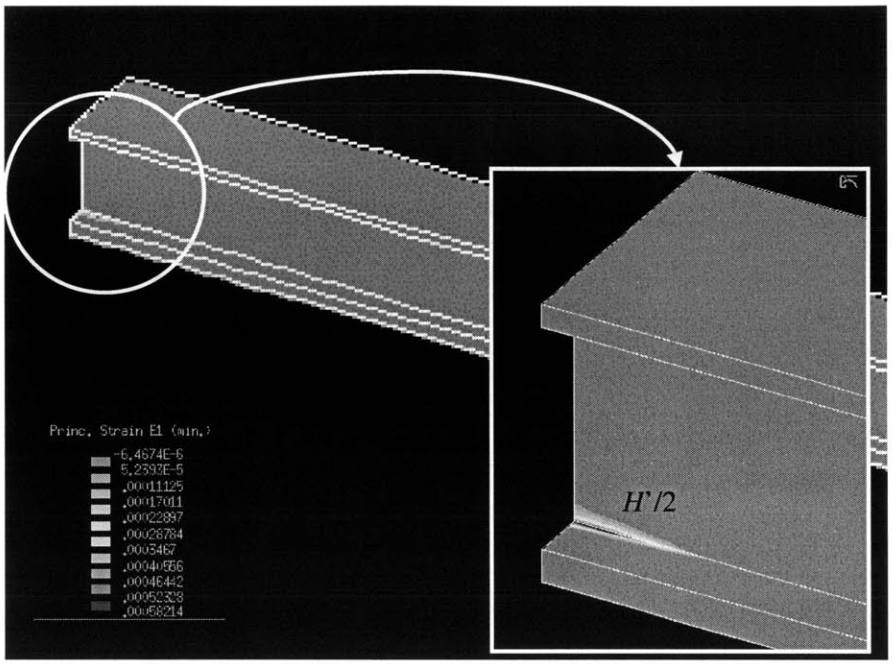

Figure 5-24: Plastic strain distribution in critical region after prestress application.

While this crack opening is almost one order of magnitude smaller than the admissible ULS crack opening, we should keep in mind that crack opening during prestressing may impair the long-term durability of the prestressed girders. One possible solution could be the use of rounded corners, to reduce stress concentrations, as displayed in Figure 5-25 (a). In this case, cracking is possibly constrained to an even smaller region (see Fig. 5-25 (b)). Alternatively, using anchor plates or debonding some of the prestressing strands over a distance $H_w/2$ could further reduce this localized risk of cracking during prestress applications. This, however, goes beyond the scope of our investigation.

5.4 Case Study of Two-Span Continuous UHPC Girders

The optimization has so far focused on single-span bridge girders, but the use of continuous girders has several advantages over single-span girders: reduction of the maximum moment and the deflection, provision of redundancy, protection of the support structures, etc. This last section on model-based optimization, therefore, addresses the question of the effectiveness of

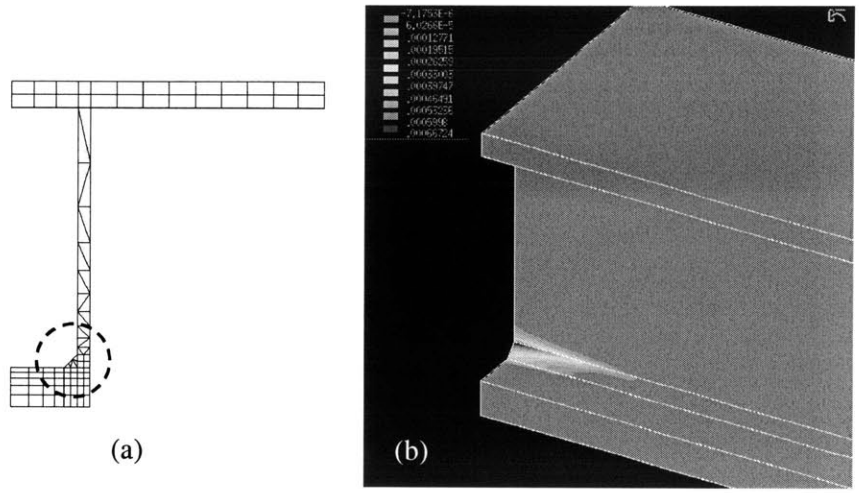

Figure 5-25: (a) Mesh of girder with rounded corner, (b) Plastic strain distribution after prestress application.

	L	B	T_s	H_w	T_w	B_f	T_f	P
30L-C	2×30.5 m (2×100 ft)	3.66 m (12 ft)	0.10 m (4 in)	1.10 m (44 in)	0.05 m (2 in)	0.30 m (12 in)	0.15 m (6 in)	4.45 MN (1,000 kips)

Table 5.3: Design parameters employed in the study of applicability of double-tee girders for coninuous beams.

double-tee girders for continuous bridge girders[6].

5.4.1 2-D Finite Element Model: Achieving Continuity After Prestressing

The structure we consider is a two-span bridge of equal spans $L/2 = 30.5$ m (100 ft). The section dimensions are those obtained from the optimization of single-span girders, summarized in Table 5.3. Given the focus on pre-tensioned applications, continuity over support is only achieved after prestressing of the individual single-span beams. This is taken into account in

[6]Continuity over supports can be addressed in various ways: 1) no continuity; 2) partial continuity and 3) total continuity. The first case corresponds to single span girders studied in previous sections, and the last case is studied in this section. One may consider the case of partial continuity, in which the continuity of stress and displacement over support is only ensured for a part of the section, for instance the slab, while web and bottom flange are discontinuous. This partial continuity is situated in between the limit cases of no continuity and total continuity, and will not be addressed here.

the 2-D finite-element simulations by modeling three separate groups: two single-span UHPC girders and a joint over the middle support:

1. During application of the factored dead weight ($\gamma_{g_1} \times g_1$) and prestressing, the elastic properties of the joint material are set to a small value, such that the stresses in the joints are negligible and the two single span girders behave independently.

2. After complete application of the factored dead weight and prestress, the material properties of the joint materials are set to those of UHPC, and the subsequent loading is applied incrementally so that the structure behaves as a continuous beam structure only for any additionally applied load. The different load cases that fall in this category are:

   (a) The dead load $\gamma_{g_2} \times g_2$, corresponding to the potential future (non-load bearing) wearing surface.

   (b) The live loads $0.9\gamma_p \times (\delta \times p_1 + p_2)$, which are gradually increased in load steps of 10% of the nominal value. The factor of 0.9 represents the load reduction factor permitted by LRFD specifications for the traffic load on continuous beams [6].

   Figure 5-26 displays the considered HS-20 design truck location that causes the maximum negative moment over support.

5.4.2 Model-Based ULS Analysis

Figure 5-27 illustrates the structural behavior captured by the finite element model after dead weight and prestress application. From the deformed shape, we verify that the rotations are not restrained over the support (rotational discontinuity) and that there is no stress transfer between the two girders, which act as two independent single span beams during this load phase. These displacement and stress states are the initial conditions for subsequent loading.

Once the continuity over the support is achieved, stress transfer occurs between the two girders as a consequence of the additionally applied dead load and live loads. The stress transfer quickly induces high surface tensile stresses in the unreinforced UHPC slab over the mid-support, which leads to cracking. Figures 5-28, 5-29 and 5-30 exemplify this behavior:

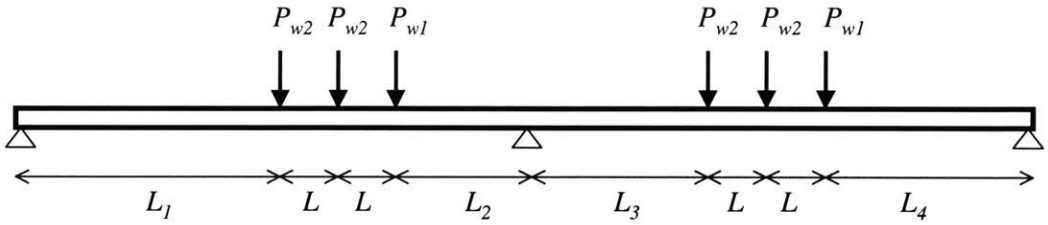

L	L_1	L_2	L_3	L_4
4.27 m	14.52 m	7.42 m	10.27 m	11.68 m
(14 ft)	(47.64 ft)	(24.36 ft)	(33.69 ft)	(38.31 ft)

Figure 5-26: Location of design truck load HS-20 for maximum negative moment: P_{w1} and P_{w2} correspond to the front and back wheel load. The (non-load bearing) wearing surface load g_2 and the uniform lane load p_2 are not shown in the figure.

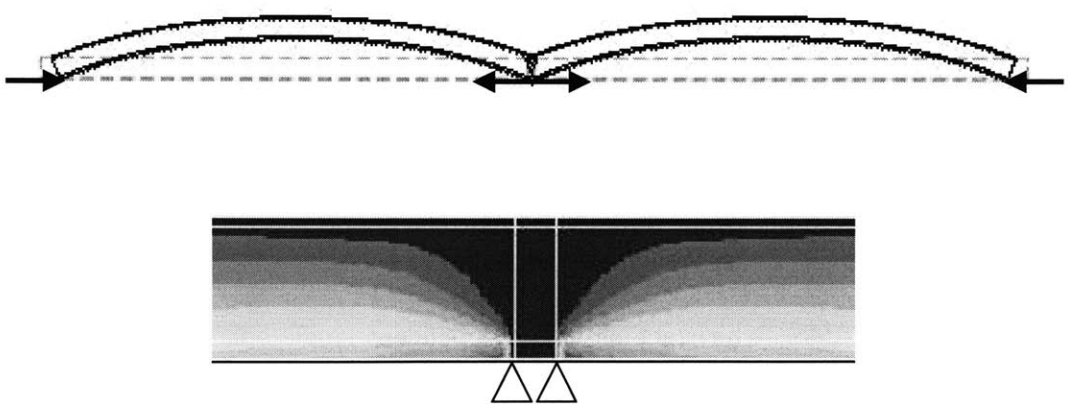

Figure 5-27: 2-D finite element simulation of the prestressing phase (prior to establishment of continuity at support). Top: Deformed Shape with rotational discontinuity over support. Bottom: Longitudinal stress distribution around mid-support, showing that there is no stress transfer between the two girders during prestress application.

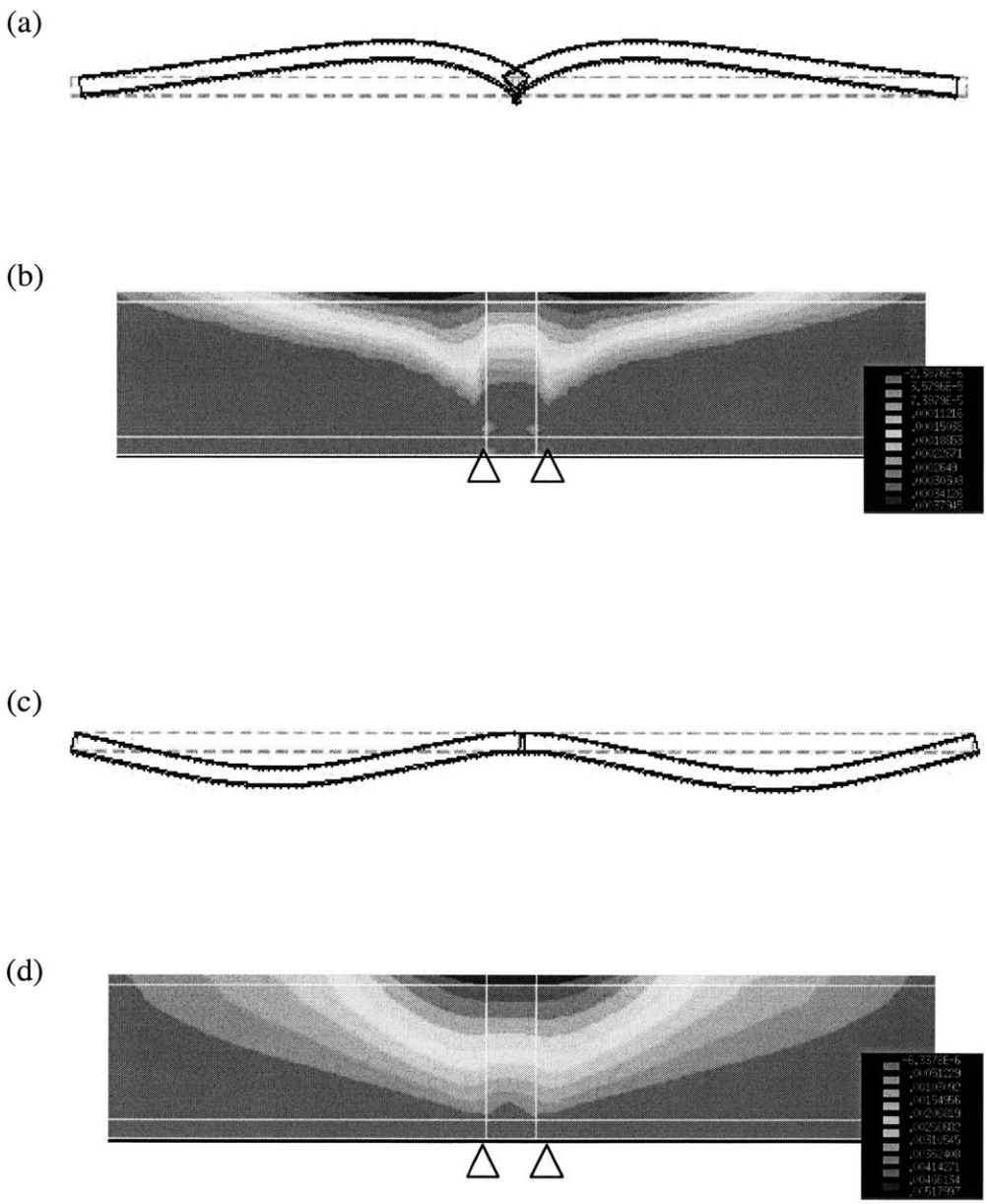

Figure 5-28: 2-D Model-based results of continuous UHPC beam: (a-b) Deformed shape and plastic strain distribution over support at 15% ULS live load level; (c-d) Same for the 100% ULS live load level.

- At a relatively low load level of 15% of the ULS live load, at which some rotational discontinuity is still present over support (Fig. 5-28 (a)), cracking over support occurs in the slab and in almost half of the web over a zone roughly the size of the girder height (Fig. 5-28 (b)), and the maximum plastic strain reaches the maximum admissible ULS strain for unreinforced UHPC sections.

- At ULS load level, the rotational discontinuity over support has disappeared (Fig. 5-28 (c)), and the cracking zone over support extends through the entire web (Fig. 5-28 (d)). This is also depicted in Figure 5-29 (a), which displays the cracking evolution (as longitudinal composite matrix plastic strains $\varepsilon^{p}_{M,xx}$) for the 15% and 100% ULS live load along the girder height over the mid support; and Figure 5-29 (b) displays the corresponding longitudinal stress profiles in the section.

- The design ultimate load level causes substantial cracking, not only over mid support, but also in the span in the vicinity of the design truck load application. Figure 5-30 (a) displays the cracking evolution for the 15% and 100% ULS live load along the girder height; and Figure 5-30 (b) displays the corresponding longitudinal stress profiles in the section. While there is no cracking in the span at the 15% ULS live load, cracking at the 100% load level extends almost entirely through the bottom flange and web, indicating that the section is close to its load bearing capacity and, as consequence, the structural load bearing capacity. Indeed, beyond this load level, our iterative numerical simulations did not converge.

5.4.3 Comment on UHPC Continuous Beams

It could be tempting to associate the cracking in span and over the mid-support with the formation of 'plastic' hinges at ULS design load level (100% ULS live load level), and associate this hinge mechanism, according to classical yield design [42], with a theoretical load bearing capacity of the two-field UHPC beam structure. However, the UHPC structure may practically never realize this theoretical structural yield capacity. Indeed, the high tensile stresses generated in the slab under the action of a negative moment over the mid-support induce cracking early on: the ULS crack opening criterion (for an unreinforced slab) is reached at only 15% of the ULS

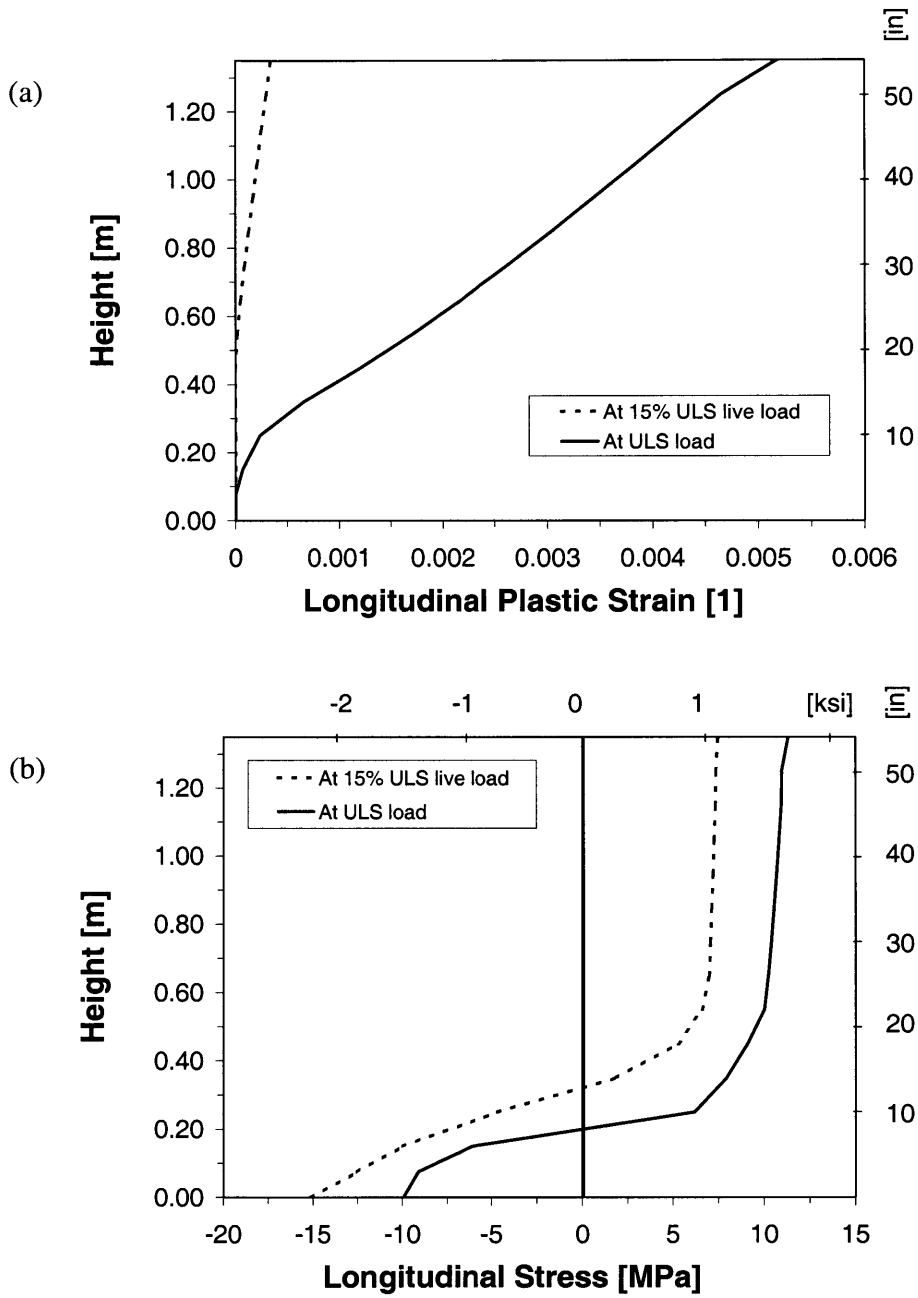

Figure 5-29: 2-D Model-based results of continuous UHPC beam over mid support (negative moment) for 15% and 100% ULS live load level: (a) Longitudinal composite matrix plastic strains $\varepsilon^{p}_{M,xx}$ along the height of the girder, (b) Longitudinal stresses Σ_{xx} along the height of the girder.

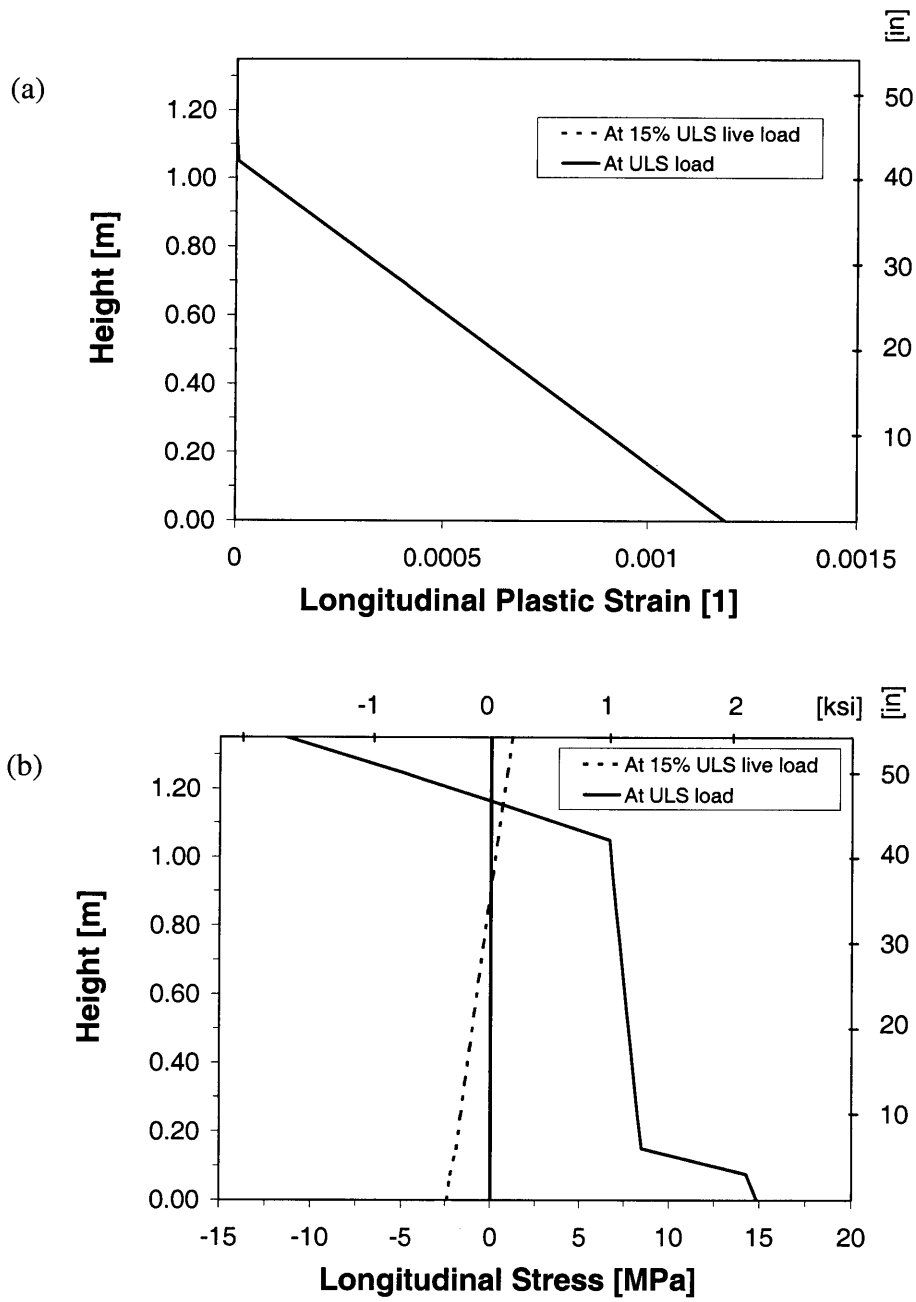

Figure 5-30: 2-D Model-based results of continuous UHPC beam in field (positive moment) for 15% and 100% ULS live load level: (a) Longitudinal composite matrix plastic strains $\varepsilon^p_{M,xx}$ along the height of the girder, (b) Longitudinal stresses Σ_{xx} along the height of the girder.

live load level, i.e. long before the statically indeterminant structure approaches its theoretical yield capacity. Once this crack opening threshold is breached, the ductile tensile behavior of the UHPC material in the unreinforced slab can no longer be guaranteed. That is, the material will exhibit softening associated with excessive cracking and fracture, so that the continuity over support will be lost long before a second plastic hinge forms in the field. This softening behavior is not taken into account in our material modeling approach, which sets a crack limit to avoid softening behavior. The results at ULS load level, therefore, are not a very realistic representation of the 'real' *in situ* behavior of UHPC, and are rather of theoretical interest, than of practical importance, thus a clear limitation of our material modeling approach.

On the other hand, the case study highlights the strength of a combination of our material model with the AFGC crack opening criterion [38], which together form a powerful tool for UHPC structural design. The material model gives access to the plastic strains of the cementitious matrix, which translate into realistic crack width values in the domain for which the ductile tensile behavior of UHPC is ensured (design focus). Within the limits of the UHPC design domain, the crack width threshold allows one to determine the actual ULS limit of the structure, not from yield design, but from a crack opening criterion, which guarantees the *in situ* ductility of material and structure. For the case study at hand, this design criterion is breached at 15% of the ULS live load level.

In summary, for continuous beams with an unreinforced slab the UHPC tensile strength alone is not sufficient to support the negative moment. While extremely efficient for single span structures, application of the double-tee girder for UHPC continuous beams would require some reinforcement and/or prestressing of the UHPC slab over the mid-support. This reinforcement will enhance the ductility of the UHPC material and allow the formation of a second plastic hinge in the field, so that the structure can reach the theoretical yield design load bearing capacity.

5.5 Summary of Optimized Design Solutions for UHPC Double-Tee Girder Sections

Tables 5.4 and 5.5 summarize the optimized design solutions for UHPC double-tee sections for single span girders in the $21 - 36\,\mathrm{m}$ ($70 - 120\,\mathrm{ft}$) span range, for two prestress force levels, $4.45\,\mathrm{MN/lane}$ ($1,000$ kips/lane) (Table 5.4) and $6.68\,\mathrm{MN/lane}$ ($1,500$ kips/lane) (Table 5.5). The chosen section parameters were adapted from the 'exact' values determined by model-based optimization to meet certain constraints and requirements:

- The choice of the slab thickness $T_s = 0.10\,\mathrm{m}$ ($4\,\mathrm{in}$) is a conservative choice. While this thickness provides some freedom in the detailed cross section design (web spacing and joint position), the thickness has been chosen in the absence of experimental results that confirm the superior behavior of UHPC in punching shear, which turned out to govern the slab behavior (see Section 5.3). While a thinner slab may be more favorable from a material processing point of view, and may improve the overall structural performance because of the reduction in self-weight, the chosen slab dimension is suitable even for prestress applications, which would become necessary when employing the double-tee section in continuous beam applications (see Section 5.4).

- The bottom flange dimensions ($T_f = 0.15\,\mathrm{m}$ ($6\,\mathrm{in}$); $B_f = 0.305\,\mathrm{m}$ ($12\,\mathrm{in}$)) have been chosen to meet the minimum space requirements for the prestressing tendons, as the gain in maximum admissible load capacity due to an increase of the bottom flange section was shown to be insignificant (see Section 5.2.5).

- While the web height is a key parameter of the flexural resistance (see Section 5.2), the web thickness was fixed to a minimum value of $T_f = 0.05\,\mathrm{m}$ ($2\,\mathrm{in}$)[7] for constructibility reasons. Indeed, in the considered span range, and for the considered load configurations, bending always dominates over shear, so that this minimum web width seems sufficient for shear resistance of this type of girder.

- It is generally more efficient to employ UHPC with high prestress levels, for which very

[7] Note that there are 2 webs per girder, and 3 webs per traffic lane composed of 1.5 girders.

Section Parameter	Symbol	Span (m / ft)				
		21.3 (70)	24.4 (80)	27.4 (90)	30.5 (100)	33.5 (110)
Prestress Force(*)	P (MN/kips)	4.45 (1,000)				
Slab Thickness	T_s (m / in)	0.10 (4)				
Web Height	H_w (m / in)	0.575 (23)	0.725 (29)	0.90 (36)	1.10 (44)	1.325 (53)
Web Thickness	T_w (m / in)	0.05 (2)				
Flange Thickness	T_f (m / in)	0.15 (6)				
Flange Width	B_f (m / in)	0.30 (12)				
Total Height	H (m / in)	0.825 (33)	0.975 (39)	1.15 (46)	1.35 (54)	1.575 (63)
Cross-Sectional Area(*)	A_{TOT} (m^2 / in^2)	0.600 (930)	0.623 (966)	0.650 (1008)	0.681 (1056)	0.716 (1100)
Estimated Weight / Lane(*)	G ([kN/m] / [kips/ft])	14.7 (1.00)	15.3 (1.04)	15.9 (1.09)	16.7 (1.14)	17.5 (1.20)
Transport Weight	W (kN /kips)	209 (46.9)	248 (55.6)	291 (65.3)	339 (76.0)	392 (87.9)

Table 5.4: Choice of section for double-tee girders prestressed with 4.45 MN (1,000 kips) per lane. (*)The total prestress force, cross-sectional area and estimated weight/lane are calculated for a single traffic lane composed of 1.5 double-tee girder sections.

shallow sections can be obtained. An increase of the prestressing by 50% allows one to reduce the total height by roughly 30% (compare values in Tabs. 5.4 and 5.5).

Finally, it is instructive to compare the found UHPC design solutions with conventional prestressed concrete solutions, i.e. AASHTO type III girders (height 1.14 m, 45 in) in the 21.3 – 24.4 m (70 – 80 ft) span range and AASHTO Type IV girders (height 1.37 m, 54 in) in the 24.4 – 36.6 m (80 – 120 ft) span range. In comparison with these design solutions, the developed UHPC solutions have three main advantages: (1) UHPC bridge girders have a substantially smaller height, considering that the UHPC girder height includes the thickness of the riding surface; (2) the in-place weights of the UHPC solutions are significantly less than corresponding classical concrete solutions (roughly 55% for 30. 5 m (100 ft) girder with 4.45 MN prestressing[8]); and (3) there is no passive reinforcement required.

[8]This estimate assumes use of one AASHTO type IV girder per traffic lane. For purposes of comparison, a 4 in slab was taken into account for the UHPC solution and a 7.5 in slab for the normal concrete solution.

Section Parameter	Symbol	Span (m / ft)			
		27.4 (90)	30.5 (100)	33.5 (110)	36.6 (120)
Prestress Force(*)	P (MN/kips)	6.68 (1,500)			
Slab Thickness	T_s (m / in)	0.10 (4)			
Web Height	H_w (m / in)	0.625 (25)	0.75 (30)	0.925 (37)	1.125 (45)
Web Thickness	T_w (m / in)	0.05 (2)			
Flange Thickness	T_f (m / in)	0.15 (6)			
Flange Width	B_f (m / in)	0.30 (12)			
Total Height	H (m / in)	0.875 (35)	1.00 (40)	1.175 (47)	1.375 (55)
Cross-Sectional Area(*)	A_{TOT} (m^2 / in^2)	0.608 (942)	0.627 (972)	0.654 (1014)	0.685 (1062)
Estimated Weight / Lane(*)	G ([kN/m] / [kips/ft])	14.9 (1.02)	15.4 (1.05)	16.0 (1.10)	16.8 (1.15)
Transport Weight	W (kN /kips)	272 (61.0)	312 (70.0)	358 (80.3)	409 (91.8)

Table 5.5: Choice of section for double-tee girders prestressed with 6.68 MN (1,500 kips) per lane. (*)The total prestress force, cross-sectional area and estimated weight/lane are calculated for a single traffic lane composed of 1.5 double-tee girder sections.

Chapter 6

CONCLUSIONS AND OUTLOOK

Ultra High Performance Concrete (UHPC) represents a breakthrough for civil engineering materials and its potentials in structural applications are far from being fully explored. Compared to standard reinforced and prestressed concrete solutions, UHPC possesses such dramatic mechanical improvements that new design philosophies, safe guidelines, and design tools for UHPC structures are required to gain true acceptance in the global civil engineering industry. The research presented in this report contributes to this goal through the development of a comprehensive model-based optimization methodology and an implementation for the design of UHPC highway bridge girders. Overall, this research confirms the added value of model-based simulations as a powerful tool for designing structures for this new material. This methodology can be applied to other materials to expedite their utilization in industrial practice.

6.1 Summary of Scientific Findings

The development of a comprehensive model-based optimization methodology yielded scientific findings regarding design criteria of UHPC structures, namely how to safely exploit the ductility of the UHPC material in structural applications that have never been considered for conventional (reinforced or prestressed) concrete solutions.

6.1.1 Model-Based Optimization Framework: UHPC Model and Crack Opening Criteria

UHPC possesses a ductile tensile strength (in the sense of strength theories, not fracture strength) that can be safely utilized in tension and shear provided measures are taken to restrict the critical crack opening to limits which ensure that the material is not loaded past its ability to transfer stresses across cracks. This requires (1) a material model for UHPC materials which accurately captures the cracking of UHPC on a material level and (2) crack opening criteria that limit, with high confidence, the risk of excessive cracking and deformation in structural applications. In this research, we employed and validated:

1. The macroscopic two-phase UHPC material model of Chuang and Ulm [14] in which the brittle-plastic composite matrix and the elasto-plastic composite fiber reinforcement are modeled as two distinct and interacting phases. The model requires a minimal number of input parameters of clear physical significance which are all obtained with a single notched tensile test. We suggest that this tensile material test becomes a requirement for the exploitation of the tensile and shear capacity of UHPC in large-scale structural applications. Though severe, the tensile properties extracted from this test are thought to reflect accurately the *in situ* tensile properties of UHPC materials, particularly after cracking. Furthermore, while exploitation of the tensile strength of cementitious materials is often restricted by the uncertainty regarding their tensile values, careful batching and mixing procedures of UHPC delivers less dispersive tensile values, which makes it possible to use the tensile yield capacity of UHPC safely in structural applications. In this sense, the notched tensile test may serve for quality control purposes of UHPC materials. Taken as input for the two-phase UHPC material model, cracking of UHPC in structures is predicted with high accuracy.

2. The crack opening criterion issued by the French Association of Civil Engineering (AFGC) [38], which effectively limits the risk of excessive cracking and deformation of unreinforced and reinforced UHPC structural elements at the Ultimate Strength Limit State (ULS). In contrast to pure strength theories (as employed in conventional concrete design), a crack opening criterion prevents the occurrence of excessive deformation in UHPC that may

trigger localized fracture or rupture, not only of UHPC but also of other critical structural components, such as prestressing tendons. The validation of the crack opening criterion with experimental data provides evidence that the values for maximum admissible crack widths proposed by the French Association of Civil Engineering (AFGC) [38] provide safe estimates for the flexural and shear load bearing capacity of UHPC structures. Similarly, a 'no cracking' criterion provides a conservative estimate of the Service Limit State (SLS).

A combination of the UHPC model and the AFGC crack width criteria provides a powerful framework for the model-based design of UHPC structures for both SLS and ULS.

6.1.2 A Comprehensive Model-Based Design Strategy: From 1-D Design Formulas to 3-D Finite Element Simulations

The model-based optimization methodology developed in this research can be broken down in different steps, with increasing complexity and different focus:

- 1-D UHPC Design Formulas: a simple section design based on section equilibrium and yield design theory suffices for estimates of primary section dimensions and design parameters, such as the section height (Sections 4.1 and 4.3) or prestressing levels (Section 5.2.5). In this research, the most simple section model for the flexural resistance of prestressed UHPC girders was employed, providing safe estimates of the actual flexural resistance: a two-point section model in which the prestressed UHPC flange was considered to have reached the effective composite strength and for which the critical crack width criterion was considered in the section moment capacity. While more refined section models will improve the predictive capability, the use of section-type design models is primarily restricted to global structural performance analyses of the ULS flexural resistance of UHPC structures.

- 2-D Model-Based Simulations: this refinement in model-based design employs the UHPC material model in plane stress 2-D finite element simulations giving predictions for deflections, stress distributions, and plastic strains in the UHPC matrix phase. The plastic strains translate into crack widths and crack patterns, which are compared with the admissible values to determine the service limit state ('no cracking') and the ultimate strength

limit state (AFGC crack opening criteria [38]). When applied to the design of single span UHPC double-tee bridge girders for medium spans ($21.3 - 36.6\,\mathrm{m}$ ($70 - 120\,\mathrm{ft}$)), it turned out that the ULS dominated over the SLS and that the flexural resistance dominated over the shear resistance. We also showed, by means of 2-D finite element simulations, the limitation of the considered section profile for continuous beam applications. More generally, the application of the UHPC material model in 2-D finite element simulations is a powerful engineering tool for the study of the overall structural performance of UHPC structures.

- 3-D Model-Based Simulations are required to study three-dimensional stress and cracking states which can become critical for the determination of local failure mechanisms in structural elements which are not detected by 1-D and 2-D approaches. A typical example is the minimum slab thickness of the UHPC girders (Section 5.3), which is subjected to punching shear as a consequence of the localized truck wheel application in addition to longitudinal and transversal bending effects. The service limit state was shown to be governed by punching shear, determining the minimum slab thickness. Another example is the 3-D investigation of the prestress transfer from the endsides into the structure (Section 5.3.5), which highlight the necessity of structural design that limits localized cracking as a consequence of prestress application. 3-D simulations are costly and time consuming and are therefore most suitable for design control and section detailing purposes once the main section parameters have been determined by 1-D and 2-D model-based simulations.

6.2 Industrial Benefits

The step-by-step application of the described design strategy allows a comprehensive model-based optimization of UHPC structures for large-scale applications, furnishing viable engineering design solutions that depart from conventional concrete structural design. The proposed UHPC double-tee section charts, suitable for precast applications, are an elegant example of the beneficial use of this optimization methodology for bridge girders: the deck is an integral part of the UHPC design solution, no reinforcement is used neither in the web nor in the slab, and the section parameters have been reduced to a minimum exploiting the truly exceptional properties

of the UHPC material considered. The proposed section solutions have many advantages over conventional precast concrete solutions (significant reduction in height and weight, elimination of shear reinforcement, etc.), which could ultimately translate into easier and faster construction processes, longer life spans with higher durability and lower maintenance, addressing requirements for the renewal of the deteriorating bridge systems in the United States and worldwide. The design strategy developed for UHPC, including the developed engineering models, will aid in achievement of these goals.

6.3 Current Limitations and Suggestions for Future Research

The developed model-based design solutions (double-tee design charts in Tables 5.4 and 5.5) for UHPC girders are limited in several aspects by conservative and simplifying assumptions, which could be addressed in future research.

- The slab thickness was chosen to ensure the 'no cracking' criterion of the service limit state. This is clearly a conservative choice, related to the absence of pertinent experimental data for punching shear of unreinforced UHPC slabs. Once punching shear data become available, we can validate the two-phase UHPC model for punching shear and then check whether a reduced slab thickness (whose advantages include in-plane distribution of UHPC fibers and reduced self-weight) is a viable design solution for bridge girders.

- From the onset, the optimization focussed on double-tee sections, because of the versatility and adaptability of these sections for detailed section design (including slab joint position, web distance, etc.). Further considerations could be given to other section types. Most of the more conventional section types (e.g. $\mathcal{I}$-section) are covered by our analysis: The 1-D section model was based on a two-point section representation, the 2-D simulation results were based on an equivalent $\mathcal{I}$-girder representations of the double-tee girder, and the 3-D slab simulations turned out to be insensitive to the number of girders per traffic lane. However, a detailed control of local effects with 3-D finite element analyses could provide necessary information about the sensitivity of other section types to prestressing transfer, slab joint position, etc., which are important issues in a detailed section design. On the other hand, 'out-of-the-box' girder sections, which were not considered in our study, must

be considered on a case-to-case basis and the full design strategy developed in this report should be employed for a detailed section design.

- The UHPC material considered in this study is DUCTAL^{TM}, and our model-based simulations were calibrated with the notched tensile results provided by the material producer (Lafarge), and validated with the FHWA large scale flexural and shear test in which also DUCTAL^{TM} was employed. That is, our material model is calibrated and validated for DUCTAL^{TM} only. While we are confident that our model is generally applicable for all types of UHPC materials with similar material performance, it is recommended that one subject the *in situ* performance of other UHPC materials to a similar quality control procedure (notched tensile test and structural test) prior to structural application. The aim of this quality control procedure is to show that the UHPC material behavior (determined by a notched tensile test) translates into structural performance (determined by a structural test). On the basis of these two independent data sets, it will be possible to employ the notched tensile data as input values for model-based design of UHPC structures.

- Finally, the design tools employed in this study are based on a linear deformation theory, which neglects second order deflection and rotation effects. While the robust sections justify the employment of a linear theory, and while the crack opening criterion generally limits large deflections, there may be certain load configurations not considered in this study in which second order effects are not negligible, e.g. lateral buckling phenomena during transport of precast girders. In the future, as the range of UHPC structural application increases, it may be useful to study these non-linear structural behaviors in greater detail.

Bibliography

[1] Canadian Precast/Prestressed Concrete Institute website (http://www.cpci.ca), 2002.

[2] FHWA website (http://www.fhwa.dot.gov), 2002.

[3] Florida Department of Transportation Structures Design Office website (http://www11.myflorida.com/structures), 2002.

[4] Lafarge North America website (http://imagineductal.com), 2002.

[5] American Association of State Highway and Transportation Officials (AASHTO). Interim to Standard Specifications for Highway Bridges, 2000.

[6] American Association of State Highway and Transportation Officials (AASHTO). AASHTO LRFD Bridge Design Specifications, 2002.

[7] C. Boulay, F. Le Maou, S. Renwez, J. Sercombe, and F. Toutlemonde. Caractérisation du comportement au choc d'un béton de poudres réactives grâce a des essais de traction direct. Res Rep. LCPC-BOUYGUES, Laboratoire Central des Ponts et Chaussées, Paris, 1997.

[8] Greg Brouwer. Bridge to the future. *Civil Engineering Magazine*, 71(11), 2001.

[9] B. Budiansky, J. Hutchinson, and A. Evans. Matrix fracture in fiber-reinforced ceramics. *Journal of the Mechanics and Physics of Solids*, 34(2):167–189, 1986.

[10] A. Burr, F. Hild, and F. A. Leckie. Continuum description of damage in ceramic-matrix composites. *Eur. J. Mech., A/Solids*, 16(7):1491–1500, 1997.

[11] E. Chuang, M. Overland, and F.-J. Ulm. On length scales of fiber reinforced cementitious composites. *Concrete Science and Engineering*, 4(14):98–105, 2002.

[12] E. Chuang, H. Park, and F.-J. Ulm. Ductility assessment of HP2C structures: From materials modeling to model-based simulation. *Submitted to Journal of Engineering Mechanics*, 2002.

[13] E. Chuang and F.-J. Ulm. Ductility enhancement of high performance cementitious composites and structures. MIT-CEE Report R02-02 to the Lafarge Corporation, 2002.

[14] E. Chuang and F.-J. Ulm. Two-phase composite model for high performance cementitous composites. *Journal of Engineering Mechanics*, December 2002:1314–1323, 2002.

[15] P. de Buhan and B. Sudret. A two-phase elastoplastic model for unidirectionally-reinforced materials. *Eur. J. Mech. A/Solids*, 18:995–1012, 1999.

[16] F. de Larrard and T. Sedran. Optimization of ultra-high-performance concrete by the use of a packing model. *Cement and Concrete Research*, 24(6):997–1009, 1994.

[17] Federal Highway Administration. Fiscal year 2003 performance plan, U.S. Department of Transportation, 2002.

[18] Federal Highway Administration. Literature made available at FHWA flexural test, 2002.

[19] Federal Highway Administration. UHPC testing: Shear. Handout made available at FHWA shear test, 2002.

[20] B. Graybeal. Personal communication, 2002.

[21] F. Hild, A. Burr, and F. A. Leckie. Matrix cracking and debonding of ceramic-matrix composites. *International Journal of Solids and Structures*, 33(8):1209–1220, 1996.

[22] Christopher D. Hill. Personal communication, 2002.

[23] J. W. Hutchinson and H. M. Jensen. Models for fiber debonding and fiber pull-out in brittle composites with friction. *Mechanics of Materials*, 9:139–163, 1990.

[24] J. W. Ju and K. H. Tseng. Effective elastoplastic behavior of two-phase ductile matrix composites: a micromechanical framework. *International Journal of Solids and Structures*, 33(29):4267–4291, 1996.

[25] B. Karihaloo and D. Lange-Kornbak. Optimization techniques for the design of high-performance fibre-reinforced concrete. *Structural and Multidisciplinary Optimization*, 21:32–39, 2001.

[26] B. Karihaloo, J. Wang, and M. Grzybowski. Doubly periodic arrays of bridged cracks and short fibre-reinforced cementitious composites. *Journal of the Mechanics and Physics of Solids*, 44(10):1565–1586, 1996.

[27] A. Kelly. The strengthening of metals by dispersed particles. Proceedings of the Royal Society of London. Series A, 282, pages 63–79. Royal Society, London, 1964.

[28] P. Ladevèze. Sur une théorie de l'endommagement aniotrope. Rep. no. 34, LMT Cachan, Cachan, France, 1983.

[29] Lafarge. Case study: cost comparison for the construction of a bridge in Ductal. Internal document, 2001.

[30] Lafarge. Suggested guidlines for the selection of a demonstration Ductal bridge. Internal document, 2001.

[31] C. Leung and V. Li. First cracking strength of short fiber-reinforced ceramics. *Ceram. Eng. Sci. Proc.*, 9/10:1164–1178, 1989.

[32] C. Leung and V. Li. New strength-based model for the debonding of discontinuous fibers in elastic matrix. *Journal of Material Science*, 26(11):5996–6010, 1991.

[33] V. C. Li. From micromechanics to structural engineering - the design of cementitious composites for civil engineering applications. *Journal of Structural Engineering and Earthquake Engineering*, 44(10):1565–1586, 1993.

[34] National Bridge Inventory. Database of National Bridge Inventory. Website (http://www.fhwa.dot.gov/bridge/britab.htm), 2001.

[35] V. Perry. Personal communication, 2002.

[36] P. Rossi. High performance multimodal fiber reinforced cement composites (HPMFRCC): The LCPC experience. *ACI Materials Journal*, 94(6):478–483, 1997.

[37] P. Rossi, O. Coussy, C. Boulay, P. Acker, and Y. Malier. Comparison between plain concrete toughness and steel fibre reinforced concrete toughness. *Cement and Concrete Research*, 16:303–313, 1986.

[38] Service d'études techniques des routes et autoroutes - Association Française de Génie Civil (SETRA-AFGC). *Bétons fibreés à ultra-hautes performances -Recommandations provisoires (Ultra High Performance Fibre Reinforced Concretes-Interim Roccomendations).* Bagneux, France, 2002.

[39] A. Simon, Z. Hajar, D. Lecointre, and J. Petitjean. Realization of two road bridges with ultra-high-performance fibre-reinforced concrete. 6th International Symposium on High Performance Strength / High Performance Concrete, 2002.

[40] H. Stang and S. Shah. Failure of fibre-reinforced composites by pull-out fracture. *Journal of Material Science*, 21(3):953–957, 1986.

[41] N. Taly. *Design of Modern Highway Bridges.* McGraw-Hill, New York, 1998.

[42] F.-J. Ulm and O. Coussy. *Mechanics and Durability of Solids, Volume I: Solids Mechanics.* Prentice-Hall, Upper Saddle River, New Jersey, 2002.

Appendix A

Conversion Factors

Table A.1 displays the conversion factor between the International Standard System of Units (SI) and the US Customary Units (IU).

	Symbol		To convert from IU to SI	To convert from SI to IU
	SI	IU	multiply by	multiply by
Length	m	ft	0.304 8	3.281
	m	in	0.025 4	39.37
Force	1 N	lbf	4. 448 2	0.22481
Area	m^2	ft^2	0.09 290 3	10.764
	m^2	in^2	$6.451\,6 \times 10^{-4}$	1550
Pressure	kPa	psi	6.894 8	0.14504
Mass	kg	lb	0.453 59	2. 204 6
Density	kg / m^3	lb / in^3	27680	$3.612\,7 \times 10^{-5}$
Moment	kN m	kips ft	1.3558	0.7376

Table A.1: Conversion factors between SI and IU units.